MACHINING ACCURACY IMPROVEMENT AND MODE COUPLING CHATTER AVOIDANCE IN ROBOTIC MILLING

A Dissertation
Presented to
The Academic Faculty

by

Lejun Cen

In Partial Fulfillment
of the Requirements for the Degree
Doctor of Philosophy in the
School of Mechanical Engineering

Georgia Institute of Technology
May 2017

MACHINING ACCURACY IMPROVEMENT AND MODE COUPLING CHATTER AVOIDANCE IN ROBOTIC MILLING

Approved by:

Dr. Shreyes Melkote, Advisor
School of Mechanical Engineering
Georgia Institute of Technology

Dr. Henrik Christensen
School of Computer Science and Engineering
University of California, San Diego

Dr. Charles Ume
School of Mechanical Engineering
Georgia Institute of Technology

Dr. James Castle
The Boeing Company

Dr. Steven Liang
School of Mechanical Engineering
Georgia Institute of Technology

Date Approved: February 3rd, 2017

ACKNOWLEDGEMENTS

First of all, I would like to thank my advisor Dr. Shreyes Melkote for giving me the opportunity to join his lab as research assistant during these years. I learnt a lot from his patient guidance throughout my time at Georgia Tech. I really appreciate his guidance and financial support. Without these, it is hard to imagine I can learn and do research at Georgia Tech. I would also like to thank Dr. Henrik Christensen, Dr. Charles Ume, Dr. Steven Liang and Dr. James Castle for taking the time to participate in my thesis committee. Dr. Henrik Christensen provided access to the industrial robotic arm used in this research. I also learnt a lot from Dr. Charles Ume's mechatronics class, which provided me the knowledge to develop and improve the performance of the wireless sensor system. Dr. Steven Liang helped me a lot during his office hours when I was doing teaching practicum in the machine tool analysis class, which enhanced my understanding of the machining process. I also learnt a lot from the discussion with Dr. James Castle during the Boeing meetings. The knowledge gained through these interactions with my committee members were very helpful in my research. I am grateful to all of them for their contributions. Their passion for teaching, research, and mentoring of students is inspiring.

I express my gratitude to all the students in PMRC. Specifically I would like to thank Aoyu Chen for her assistance in signal processing and encouragement all through these years. Vinh Nguyen also helped me a lot in various matters, such as the PCB design of the wireless sensor system and filter board design, etc. All of these were very important for my research. Finally, I want to give special thanks to my friends and family

for their encouragement, especially my parents. As a second son in China, I understand that they sacrificed a lot (jobs, money, etc.) to bring me to this world. Words alone cannot fully express my appreciation for what they have done for me.

TABLE OF CONTENTS

LIST OF TABLES

LIST OF FIGURES

NOMENCLATURE

a	Radial depth of cut
$[A]$	System matrix to determine the stability of the system
b	Axial depth of cut
c	Feed per tooth
$[C]$	System damping matrix
D_0	Shank diameter of the end mill
E_t	Young's modulus of the end mill
$\bar{F}$	Average resultant cutting force
$d\bar{F}$	The change in average resultant cutting force
F_{peak}	The peak of the resultant force
F_{PV}	The difference between the largest and smallest peaks of the resultant force
F_r	Radial force
F_t	Tangential force
f_{max}	The theoretical maximum feed rate that does not overload the robot or does not cause chatter
f_{real}	The feed rate chosen based on a predetermined safety factor
h	Instantaneous uncut chip thickness
$[I_\theta]$	Rotational inertia matrix of the robot
$[J]$	Kinematic Jacobian matrix for the robot
$[K]$	System stiffness matrix in the Cartesian space
$[K_c]$	Conservative Congruence Transformation (CCT) based additional stiffness matrix
$[K_p]$	Cutting stiffness matrix

K_{tc},K_{rc}, K_{ac}	Cutting force coefficients contributed by the shearing action in the tangential, radial, and axial directions, respectively
K_{te},K_{re}, K_{ae}	Edge force coefficients in the tangential, radial, and axial directions, respectively
K_{max}	The maximum principal stiffness vector of the robot arm
K_{min}	The minimum principal stiffness vector of the robot arm
K_{px}	Cutting stiffness in the *X* direction
K_{py}	Cutting stiffness in the *Y* direction
$[K_\theta]$	Stiffness in the joint space
ΔK	The difference between the maximum and minimum principal stiffness of the robot arm
L_c	A real, positive number determined from an acceptable false alarm rate
L_p	The axial distance from the idealized concentrated feed/transverse force to the center of the PVDF sensor
L_S	Section length
$[M]$	System mass matrix
N	Number of cutter teeth
R	Radius of the end mill
δR	The change in cutter radius due to runout
r	Ratio between the average resultant forces in Y and X directions
r_c	Ratio between the radial and tangential cutting forces
T_x, T_y, T_z	Moment about X, Y, Z axis, respectively
$[V]$	Coordinate transformation matrix
V_p	PVDF sensor voltage signal
$[V_Y]$	Transformation matrix for the rotation about the *Y* axis
$[W]$	Wrench (forces and moment) applied to the robot end-effector

X_{static}	Static deflection error
ΔX	Bending error
Z_c	Cumulative distribution function of a standard Gaussian distribution
Z_n	The vibration amplitude normal to the cut surface
α	The rotation angle about Y axis for 2 dof simplification
$\delta\alpha_x$	Rotation about the X axis
α_f	False alarm rate: the probability of issuing an alarm when chatter does not occur
β	The angle between the nominal average force vector and the *X* axis
γ	The angle between maximum principal stiffness vector of the robot and the average resultant cutting force vector
γ_{tran}	The transition angle between stable and unstable regions
$\Delta\gamma$	The variation of angle γ based on linear interpolation between the section endpoints
$\Delta\gamma_c$	The variation of angle γ due to the CCT effect
$\Delta\gamma_{max}$	Maximum allowable change of angle γ for that particular section
$[\Delta]$	System displacement
ε	Bending strain generated in the tool at the location of the PVDF sensor
$[\theta]$	Joint space of the robot
θ_t	Tool angular position
θ_{to}	Initial tool angular position
λ	Eigenvalue of a matrix
σ	Standard deviation of wavelet signal
$\emptyset$	Cutter rotation angle
$\emptyset_p$	Pitch angle of the cutter

$\emptyset_{st}$	Entry angle of the immersion zone
$\emptyset_{ex}$	Exist angle of the immersion zone
ω_o	Angular velocity of the end mill

SUMMARY

Robotic milling offers an attractive and cost-effective alternative to multi-axis CNC machining of large aerospace structures. Multiple degree-of-freedom (dof) articulated robotic arm-based machining has several potential advantages over traditional CNC machine tools including greater flexibility (reconfigurability) and lower cost. However, its industrial application is currently limited by its lower stiffness compared to a CNC machine tool, which easily gives rise to static deflection errors and vibration during the milling process. Therefore, the robot's elastic deformation and chatter vibration must be adequately minimized to achieve higher part feature dimensional accuracy. Therefore, this thesis focuses on the elastic deformation and chatter vibration aspects of robotic milling.

At first, the effect of robot structural dynamics on the forces produced in robotic milling is analyzed in this thesis. For this purpose, a dynamic milling force model incorporating the effect of robot dynamics and the effect of external forces on the robot stiffness are implemented. The force model leverages existing work on dynamic modeling of milling forces where the influence of system compliance on the equilibrium or "steady state" uncut chip thickness is accounted for using an iterative computation process. The proposed iterative approach demonstrates significantly better performance than the forced vibration model that uses only the first iteration.

A new hybrid method is proposed that combines wireless force sensing with a mechanistic model of the milling forces to enable improvements in the dimensional accuracy obtained in robotic milling by compensating for the static elastic deformations

of the robot arm. It employs an in-situ thin film wireless force sensor to measure in real-time the milling forces, which are input to a mechanistic milling force model to estimate the instantaneous cutter engagements for direct tool position compensation feedback. When the proposed static deflection error feedback control strategy was implemented, experimental results showed at least 70% improvement in the cut surface dimensional error.

Next, the Conservative Congruence Transformation (CCT) is integrated into the robotic milling chatter model to account for the effect of average milling force on the robot stiffness. Unlike prior work on mode coupling chatter analysis where the angle γ between the robot principal stiffness vector and the milling force vector can only be altered by changing the workpiece orientation and robot arm configuration, in this thesis the use of the milling force dependent CCT-based stiffness term allows the chatter instability to be avoided by altering the cutting conditions.

Finally, the thesis presents a force sensing-based approach for real time chatter detection and suppression in the robotic milling process.

CHAPTER 1. INTRODUCTION

1.1 Motivation and Problem Statement

Multi-axis milling of large aerospace structures is usually carried out on rigid and accurate multi-axis CNC machining centers. However, such machining centers are expensive and occupy a large footprint on the factory floor. In contrast, an articulated-arm based robotic milling system is in principle capable of highly flexible machining of large complex parts. An integrated robotic milling system consists of a multi-axis articulated-arm robot with a milling cutter held in a spindle motor attached to the robot end-effector. Compared to a traditional CNC machine tool, a robotic milling system can yield work space savings of up to 40% in addition to providing greater flexibility and versatility for machining [1, 2]. Robotic milling is also highly desirable in noisy, dusty and unhealthy working environments [3]. However, its industrial application is currently limited by its lower stiffness compared to a CNC machine tool, which easily gives rise to robot static deflection error and vibration during the milling process. Therefore, the robot's elastic deformation and chatter vibration must be adequately minimized to achieve higher part feature dimensional accuracy.

A major hurdle in the adoption of an articulated-arm robot for high process load applications, such as milling, is its position error due to the elastic deformation of the robot arm. While several researchers have developed different methods to minimize the robotic arm static deflection error, the current approaches reported in literature suffer from at least one of the following drawbacks: 1) high cost, 2) extremely conservative cutting conditions, including the use of plastic workpieces and small diameter cutters, and

3) time-consuming stiffness determination along the entire tool path. Therefore, a low cost and efficient method to minimize robot static deflection error under practical cutting conditions is warranted.

Another limitation in robotic milling is chatter vibration, which can result in poor dimensional accuracy of the workpiece, reduction in tool life, and damage to the tool spindle and robot, etc. While researchers have analyzed the robotic milling chatter phenomenon using the classical mode coupling chatter model, they do not account for the effect of time-varying milling forces on the stiffness. In addition, even though the angle between the average resultant cutting force and the robotic arm maximum principal stiffness is related to chatter stability in robotic milling, the effect of cutting parameters on this angle are not fully understood. Consequently, a model that considers the effect of the milling forces on the robotic arm stiffness and the effect of cutting parameters on mode coupling chatter stability in robotic milling is needed.

Although some researchers have proposed methods/guidelines to avoid mode coupling chatter in robotic milling by changing the robot arm configuration or the workpiece/tool feed orientation, limiting the robot arm configuration or the tool feed direction limits the flexibility and versatility of robotic milling in practical applications. In addition, on-line detection and suppression of chatter via real-time process monitoring are very important to account for the process uncertainties in robotic milling, which have not been reported in literature. Therefore, a more practical chatter avoidance method with on-line detection and suppression algorithm is highly desirable.

To summarize, the need for more advanced solutions for accuracy improvement and chatter avoidance/suppression in robotic milling serve as motivation for the research described in this thesis.

1.2 Research Objectives

In light of the problems and motivation discussed in the previous section, this thesis addresses the study of new methods to improve robotic milling dimensional accuracy and to develop a more comprehensive robotic milling chatter model for chatter avoidance. The specific objectives of this research are to:

1. Develop a new approach to increase the accuracy of robotic milling by minimizing the tool position error due to robot compliance.

2. Develop a more comprehensive model for robotic milling chatter analysis that considers the effect of milling forces on the robot stiffness and the effect of cutting conditions on chatter stability.

3. Develop a new method for chatter detection and chatter avoidance in robotic milling.

The research objectives of this thesis are accomplished through a comprehensive literature review of prior work followed by modeling, analysis, and experimental validation of the proposed solution approaches.

1.3 Proposed Approach

A robotic milling static deflection error compensation method that utilizes real-time force sensing in combination with a mechanistic static milling force model to estimate the cutter engagements for static deflection error compensation is proposed. The effect of robot structural dynamics on the milling forces is analyzed to determine the conditions under which the use of a static mechanistic milling force model is valid. In addition, a dynamic model for robotic milling chatter analysis that considers the effect of milling forces on the robot stiffness is proposed. The Conservative Congruence Transformation (CCT) is integrated into the model to account for the effect of time-varying milling forces on the robot stiffness. Subsequently, the eigenvalues of dynamic system of equations are calculated to determine the mode coupling chatter stability criterion. Using the milling force dependent stiffness term, the cutting parameters are selected so that the system is stable i.e. all eigenvalues of the dynamic system of equations are negative and real. Finally, a method for real-time chatter detection and suppression is proposed to take into account uncertainty in the robotic milling forces due to material property variations and/or other unexpected variations in the process. Based on the estimation of chatter frequency from the dynamic process model, the corresponding decomposition level in wavelet transform is pre-determined so that the mode coupling chatter frequency is within the wavelet band of interest. Once chatter is detected using the wavelet transform, the appropriate cutting parameter is adjusted to suppress chatter using the adjustment guidelines derived from the CCT-based chatter model. The proposed approach is summarized as below in Figure 1.

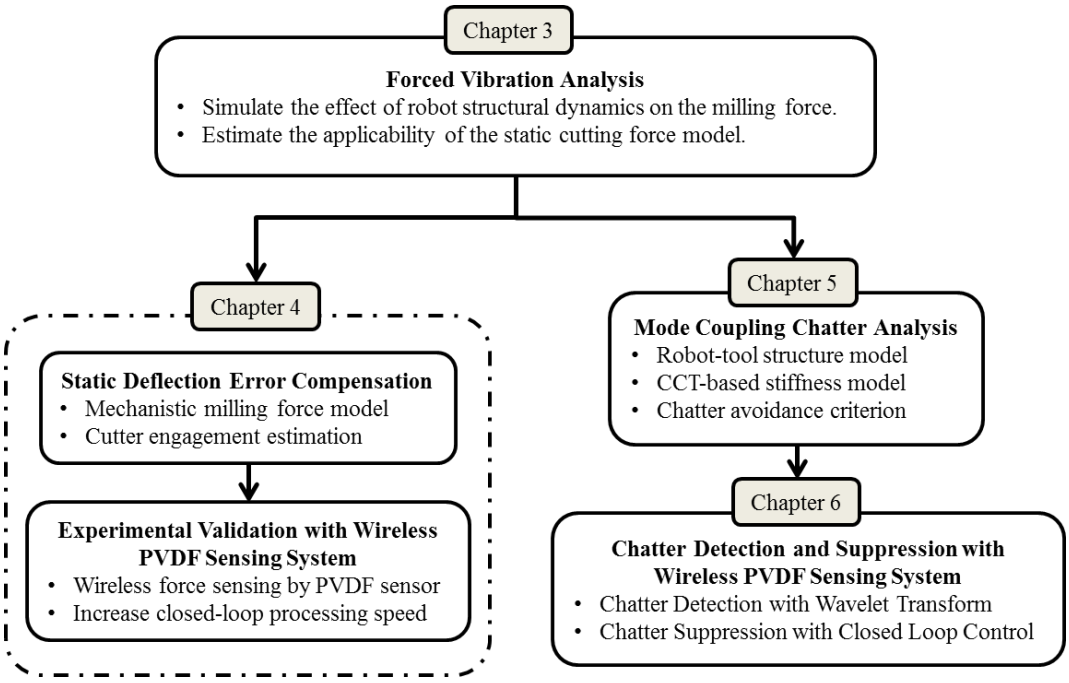

Figure 1. Summary of the proposed approach.

1.4 Thesis Outline

The remainder of this thesis is organized as follows. Chapter 2 presents a comprehensive review of the relevant prior work in robotic milling. Chapter 3 presents an analysis of the effect of robot structural dynamics on the forces produced in robotic milling. Chapter 4 presents a new method that combines wireless force sensing with a mechanistic model of the milling process to increase the dimensional accuracy of robotic milling process by minimizing the tool position error due to static compliance of the robot. Chapter 5 presents an enhanced model for robotic milling chatter analysis that involves the CCT-based stiffness term, which accounts for the effect of milling forces on the robotic arm stiffness. In Chapter 6, a wavelet decomposition based method for real-time chatter detection and suppression is proposed to account for uncertainties in the

robotic milling process that cannot be included in the model. Finally, the major conclusions of this thesis and recommendations for future work are given in Chapter 7.

CHAPTER 2. LITERATURE REVIEW

A critical review of the relevant work available in the literature is presented in this chapter. The review is divided into four areas: 1) dynamic effect in robotic milling, 2) static deflection error reduction in robotic milling, 3) chatter phenomenon in robotic milling, and 4) mode coupling chatter avoidance in robotic milling.

2.1 Dynamic Effect in Robotic Milling

Dynamics plays an important role in the cutting force model selection in robotic milling. To model the cutting forces, two approaches can be used. The static approach involves computing the static cutting force without considering the influence of structural dynamics on the material removal process. The assumption of a rigid milling system for the calculation of forces has been shown to work in the analysis of conventional CNC machining [2], which is generally characterized by high machine stiffness. In contrast, the stiffness of a serial link robot changes as a function of the arm configuration. For certain arm configurations, the robot may exhibit relatively low structural stiffness. Under such conditions, system deflections will be large enough to produce a significant effect on the chip load and hence the cutting forces. Consequently, the cutting forces cannot be modeled accurately using the static approach when the robot's dynamics is significant. Therefore, the dynamic effect for the corresponding robot arm configuration must be analyzed before selecting the proper cutting force model for use in robotic milling analysis. The analysis is based on computing the dynamic uncut chip thickness, which is derived from the instantaneous interaction of the vibrating tool (robot) with the workpiece [4].

For a CNC machining system, the dynamic effect is usually taken into account in special cases, such as in machining of thin-walled sections or deep pockets/cavities with long cutters. In these special cases, the deflections of the workpiece and/or cutter can become large and significantly affect the chip load and hence the cutting force. Sutherland and DeVor [5, 6] developed a dynamic cutting force model for end milling of deep cavities with long cutters. The dynamic effect of the long cutter was modeled as a continuous fixed-free cantilever beam undergoing vibrations. The dynamics of the long cutter instantaneously modulates the uncut chip thickness. As shown by Sutherland and DeVor [5, 6] and others [7], the instantaneous milling force is a function of the instantaneous chip thickness, which in turn is affected by the compliance of the machining system (e.g. due to a long milling cutter). This requires iterative computation of the equilibrium or "steady state" dynamic uncut chip load at each time instant.

Different from the cantilever beam model assumption for long cutters, analysis of the dynamic effect in robotic milling is more complex due to the complexity of the robotic arm structure. Consequently, the majority of robotic milling research reported to date still uses the static cutting force model, which is valid when the dynamic effect is negligible [8-14]. Therefore, in order to use the static cutting force model in robotic milling, the magnitude of the dynamic effect for the corresponding robot arm configuration must be analyzed to identify the cutting conditions where the static assumption is valid.

Although extensive research on dynamics of CNC milling has been carried out, limited work has been reported on the dynamic effect in robotic milling [4, 15-17]. While Bondareko et al. [17] modeled the effect of robot dynamics on the milling forces, they

did not account for the equilibrium between the robot dynamics and the resulting forces at each time instant nor did they present experimental validation of their force model.

Another limitation of the current state-of-the-art in dynamic analysis of robotic milling is the use of a conventional stiffness model for the robot, which neglects the effect of external loading on the stiffness. Prior works have used a simplified stiffness model of the robot derived from a mapping between the joint and Cartesian spaces, which is strictly not valid for robotic milling because the robot stiffness is influenced by the machining forces [18-21]. The existence of an additional stiffness term due to external force (e.g. due to machining) was demonstrated in the form of the Conservative Congruence Transformation (CCT) [18-24]. However, prior work in robotic milling has not utilized the CCT to account for the effect of external force on robot stiffness.

Therefore, a more comprehensive model is required to analyze the dynamic effect of different robot arm configurations under different cutting conditions. For simplicity, similar to the majority of robotic milling work in literature [8-11, 25-31], the classical static milling force model is utilized in the following chapters on static deflection error compensation and chatter avoidance/suppression, where the cutting conditions employed are such that the effect of robot structural dynamics on the milling forces can be neglected.

2.2 Static Deflection Error Reduction in Robotic Milling

Even though the effect of robot structural dynamics on the milling forces can be minimized through careful selection of the robot arm configuration and of the cutting conditions, static deflection error is still present due to the inherently low stiffness of the

robotic arm structure compared to a CNC machine tool. According to [27, 32], machining applications are less than 5% of the industrial robotic market. Articulated arm robotic systems are currently used in low process force applications such as material handling, welding, deburring, and assembly [9-13, 33-41]. The articulated robotic arm's relatively low structural stiffness is a major drawback in machining applications. Compared to the a conventional CNC machine tool, which has a stiffness on the order of 10^8 N/m, the robot arm's stiffness is on the order of 10^5 – 10^6 N/m [10, 11]. Consequently, a large position error often results in robotic milling and therefore must be minimized.

Various methods have been used to reduce the static deflection error in robotic milling (see Figure 2). They include: 1) reducing the cutting forces, 2) increasing the robot arm stiffness, and 3) compensating for the static deflection error.

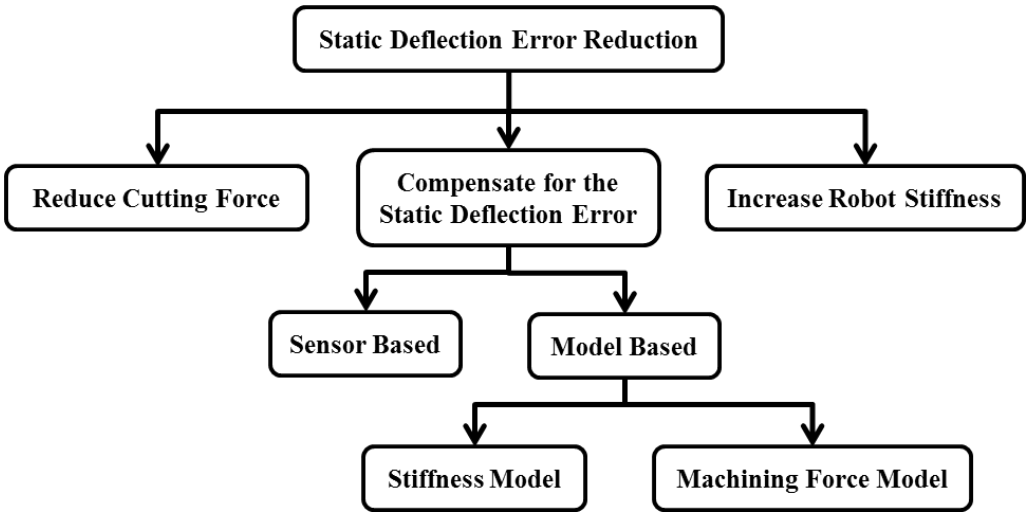

Figure 2. Summary of static deflection error reduction in robotic milling.

Because the static deflection error is proportional to the cutting force magnitude, researchers have used conservative cutting conditions to reduce the cutting force directly,

such as by using a small diameter of end mill and a high-speed spindle [2], or by cutting a soft material [42]. However, using conservative cutting conditions jeopardizes productivity significantly, and is therefore impractical for industrial applications.

The static deflection error can also be reduced by enhancing the robotic arm stiffness, such as using a double parallel mechanism [43, 44]. However, changing the robotic arm structure is costly. In addition, the robot's flexibility is reduced when enhancing the stiffness through such means.

The third method involves compensating the static deflection error directly, which is regarded as the most popular method in literature. Prior work on robot compliance compensation focuses on gravity and elastic deflection compensation of flexible robotic arm structures [45, 46]. To simplify the problem, the robotic arm is considered to be flexible so that the compliance of the joints and links are included in the compensation model [47]. The external load applied to the manipulator is generally treated as a deadweight attached to the robotic arm end effector. Not much attention has been paid to the compensation of robot elastic deformation induced by process forces (such as time-varying milling forces) [48].

The two main approaches for compensating process force induced robot elastic deformations are position sensor based compensation and model based compensation. Position sensor based compensation methods measure the deflection error directly in either the Joint or Cartesian space and then adjust the robot position accordingly [12]. For instance, in [49], a linear scale was used to measure the link deformations caused by external forces. However, position sensor based compensation methods are difficult to

implement in robotic milling [48], where the milling cutter is immersed in the workpiece and is occluded by chips and coolant. In addition, optical sensors are prohibitively expensive [31]. Thus, sensor based compensation methods are more suitable for high accuracy uniaxial processes such as drilling, where the tool path is relatively simple compared to milling [48].

Unlike sensor based methods, model based compensation utilizes a model to predict the robot elastic deformation and utilize it to compensate the position of the robot arm. Work on modeling and identification of robot stiffness for milling applications has been reported in the literature [12, 13, 28, 30, 38, 50, 51]. However, precise determination of the robot arm stiffness within its entire work volume as a function of its pose or configuration is challenging [48]. Due to the complexity of robot arm stiffness modeling, researchers simplify the problem to mapping of stiffness matrices between the Cartesian and Joint spaces [8, 13, 20, 52]. However, this simplification suffers from many drawbacks. For instance, it is only valid when the manipulator is in a quasi-static configuration and is under no loading, or the Jacobian matrix throughout the robot work volume is constant, which is unrealistic in robotic milling [18, 19, 21, 23]. In addition, the stiffness of a robotic arm is generally nonlinear and varies with robot pose or configuration. The complexity of robotic arm stiffness modeling is a major hurdle for the effective industrial application of robotic milling. Precise determination of the robotic arm stiffness along the whole tool path is time consuming and expensive.

Above all, the current approaches for reducing the static deflection errors due to elastic deformation of the robot suffer from at least one of the following drawbacks: 1) high cost, 2) use of extremely conservative cutting conditions or the use of a soft

workpiece or a small cutter, and 3) time-consuming stiffness estimation, such as the precise stiffness determination along the entire tool path. Therefore, a low cost and time-efficient method for reducing the robot static deflection error under normal cutting conditions is necessary.

2.3 Chatter in Robotic Milling

Although extensive research on machining chatter – a dynamic instability – has been carried out, limited work has been reported on the chatter mechanism in robotic machining [9, 11]. The result is that robotic engineers and technicians are severely constrained when dealing with chatter issues without a good understanding of the phenomenon. Very often, to get the machining process working correctly, one has to resort to trial and error methods for tuning a setup or sacrifice productivity by settling on very conservative cutting parameters that negatively impact productivity [11].

Different from the commonly encountered regenerative chatter in conventional CNC machining, mode coupling chatter was identified as the dominant source of vibration in robotic machining [9]. This chatter mode is primarily due to the low structural stiffness of the industrial robot relative to the cutting stiffness [9, 11]. Mode coupling chatter is due to the fact that the system mass vibrates simultaneously in the directions of the degrees of freedom of the system, with different amplitudes and phases. Researchers usually control the angle γ between the average resultant machining force and the maximum principal stiffness to avoid mode coupling chatter, as shown in Figure 3. Analysis of chatter in robotic machining was first reported in 2006 by Wang et al [9]. They investigated both regenerative and mode coupling chatter theories to explain the

drastic low frequency vibration under certain machining conditions. Their robotic milling experiments demonstrate that although regenerative chatter, which is generally characterized by high frequency vibrations, is commonly encountered in conventional machining processes, it has little relationship to the low frequency structural vibration commonly encountered in robotic milling. An analysis of mode coupling chatter shows that if the structural stiffness is not significantly higher than the cutting stiffness, mode coupling chatter can occur. Since the stiffness of a conventional CNC machine tool is generally hundreds of times larger than the cutting stiffness, mode coupling chatter rarely occurs in machining carried out on conventional CNC machine tools. However, for articulated arm robots, the stiffness difference is only 5–10 times more than the cutting stiffness, which makes mode coupling chatter the dominant reason for structural vibrations in robotic machining [9, 11].

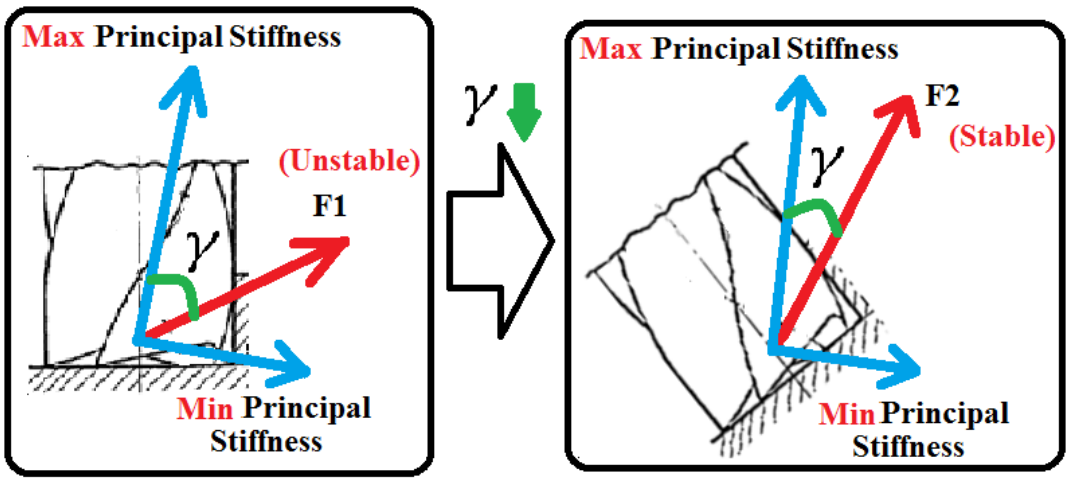

Figure 3. Changing tool feed (milling force) direction or workpiece orientation to stabilize the system.

Due to the complexity of the robot arm stiffness, existing robotic milling chatter models are based on a simplified mapping between the Joint space and the Cartesian space stiffness matrices [8, 9, 11]. Again, this simplification is valid only when the manipulator is in a quasi-static configuration with no external loading, or the Jacobian matrix throughout the robot work volume is constant, which is unrealistic [18, 19, 21, 23].

Consequently, a more comprehensive model is needed for robotic milling chatter analysis to take into account the effect of milling force on the robotic arm stiffness and the effect of cutting conditions on mode coupling chatter stability.

2.4 Mode Coupling Chatter Avoidance in Robotic Milling

Tobias and Fishwick [53] and Tlusty and Polacek [54] recognized that the most powerful sources of chatter or self-excited vibrations were the regenerative and mode coupling effects. Regenerative chatter occurs when the vibrating tool cuts an uneven surface generated by the vibrating tool in the previous tool pass or revolution, and therefore the undeformed chip thickness and the corresponding cutting forces vary continuously. Depending on the phase shift between two successive undulations, the maximum chip thickness may grow exponentially and cause regenerative chatter. Mode coupling chatter occurs when the system mass vibrates simultaneously and with different amplitudes and phases in the directions of the degrees of freedom of the system. As explained by Altintas [55], the regenerative chatter is more commonly encountered in CNC machining, where the structure stiffness is large.

Despite the availability of a large number of studies on regenerative chatter in milling, publications on mode coupling chatter are scarce. Noteworthy are the work of Tobias et al.[41], Gasparetto et al. [39, 40], Wang et al. [9] and Pan et al. [11]. These studies propose the avoidance of mode coupling chatter by adjusting the angle γ between the maximum principal stiffness vector (K_{max}) of the robot arm and the milling force vector (F). Theoretically, this can be accomplished by changing direction of K_{max} or F (see Figure 4a and b). However, in prior work, the stiffness of machining structure is assumed constant. Therefore, prior work has proposed altering the workpiece orientation to avoid mode coupling chatter, as shown in Figure 4a.

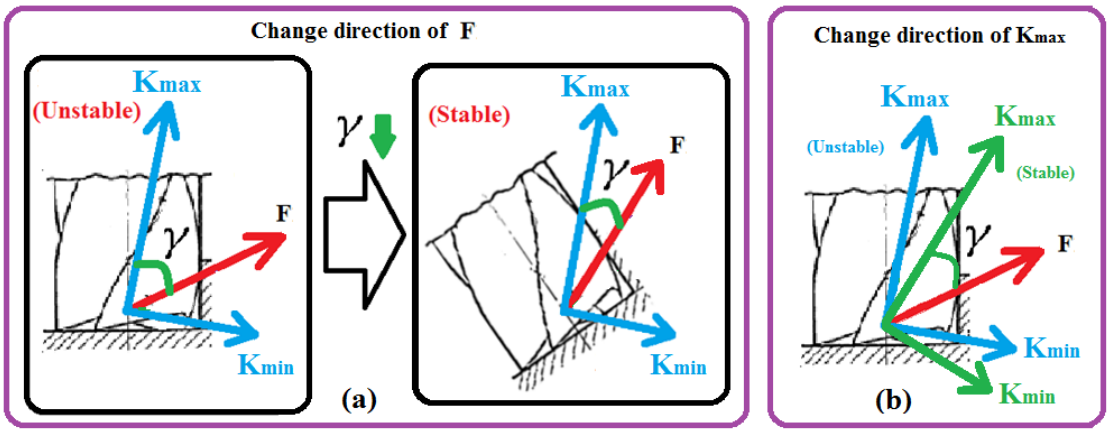

Figure 4. Mode coupling chatter avoidance.

However, limiting the tool feed direction or the workpiece orientation in robotic milling reduces its flexibility and versatility for machining, which therefore makes this approach to chatter suppression impractical for industry applications. In addition, on-line detection and suppression of chatter via real-time process monitoring are critical to account for the process uncertainties in robotic milling, which have not been reported in

literature. Therefore, a more practical chatter avoidance method with on-line detection and suppression algorithm is highly desirable.

2.5 Summary

It can be seen from the literature survey that prior work on static deflection error reduction and chatter avoidance in robotic milling suffer from at least one of the following drawbacks: 1) high cost, 2) the use of extremely conservative cutting conditions, or the use of a soft workpiece or a small cutter, 3) difficulties in accurate determination of the robot stiffness, and 4) limitations in the tool feed direction or the workpiece orientation. The existing models for robot static deflection error compensation and chatter avoidance do not account for the effect of milling force on the robotic arm stiffness and the effect of cutting conditions on chatter stability. In addition, on-line detection and suppression of chatter via real-time process monitoring, which have not been reported in literature, are important to account for the unavoidable process uncertainties in robotic milling.

The remainder of this thesis describes the effect of robot dynamics on the milling forces, a novel and time-efficient approach to reduce the robot position error due to static deflections arising from the process forces, the development and validation of an enhanced model for robotic milling chatter analysis, and the development and validation of an on-line chatter detection and suppression algorithm.

CHAPTER 3. EFFECT OF ROBOT DYNAMICS ON THE MILLING FORCES IN ROBOTIC MILLING

3.1 Introduction

In this chapter, the effect of robot structural dynamics on the forces produced in robotic milling is analyzed. For this purpose, a dynamic milling force model incorporating the effect of robot dynamics and the effect of external forces on the robot stiffness is implemented. The force model leverages prior work on dynamic modeling of milling forces [5, 6] where the influence of system compliance on the equilibrium or "steady state" uncut chip thickness is accounted for using an iterative computation process. The effect of milling forces on the robot arm stiffness is accounted for using the Conservative Congruence Transformation (CCT). In addition, this chapter analyzes the significance of robot dynamics on the milling forces as a function of the robot configuration (pose) and the cutting conditions. In the following sections of the chapter, the overall methodology and approach are described, followed by experimental validation, discussion of results and conclusions.

It should be noted that the dynamic milling force model presented in this chapter is a simplified discrete model used to estimate the effect of robot dynamics on the milling forces. This model permits the identification of the cutting conditions and robot arm configuration for which the effect of robot dynamics on the milling process can be neglected.

3.2 Dynamic Model of the Robotic Milling System

The structural dynamic model of the robotic milling system consists of the dynamic models of the cutting tool, the workpiece, and the corresponding fixturing system. The generalized dynamic model presented here includes two systems, as shown schematically in Figure 5; namely, the cutter and its fixture (system 1), and the workpiece-fixture combination (system 2). The governing equations for the two systems are given by:

$$[M_1]\{\ddot{\Delta}_1\} + [C_1]\{\dot{\Delta}_1\} + [K_1]\{\Delta_1\} = [F_1] \quad (1)$$

$$[M_2]\{\ddot{\Delta}_2\} + [C_2]\{\dot{\Delta}_2\} + [K_2]\{\Delta_2\} = [F_2] \quad (2)$$

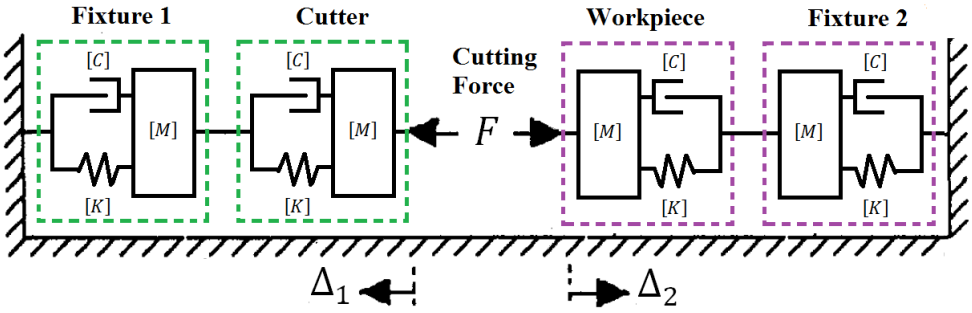

Figure 5. Structural dynamic model of a robotic milling system.

where $[\Delta]$, $[F]$, $[M]$, $[C]$ and $[K]$ are the system displacement, resulting milling force, mass, damping, and stiffness matrices, respectively. The sizes of these matrices depend on the number of degrees of freedom involved in the application at hand. The total system instantaneous deflection in the presence of cutting forces is given by $\Delta = |\Delta_1| + |\Delta_2|$. For a typical robotic milling application, the robot arm is usually the most flexible component, which dominates the structure's dynamic characteristics. Finite element

analysis can be used to compute the deflections in applications involving a flexible cutter and/or workpiece. However, similar to the work of other robotic milling researchers [8, 9, 11], this thesis considers the cutter and workpiece compliances to be negligible relative to the compliance of the robot structure itself.

The mass matrix $[M]$ is related to the robot's rotational inertia matrix $[I_\theta]$ in the joint space $[\theta]$ as

$$[M] = [J(\theta)]^{-T}[I_\theta][J(\theta)]^{-1} \tag{3}$$

where $[J(\theta)]$ is the kinematic Jacobian matrix for the robot, which depends on the joint angles $[\theta]$. The damping matrix $[C]$ is difficult to determine accurately and is ignored here for the sake of simplicity, as in other robotic milling works [9-13, 38-40].

The sources of stiffness in a typical robotic manipulator include the compliances of its joints, actuators, its transmission elements, the geometric and material properties of the links, base, and the active stiffness provided by its position control system. For simplicity and without loss of generality, this thesis, similar to the work of other researchers [12, 13, 25, 26, 38, 56, 57], assumes that: 1) the primary source of stiffness is the joint stiffness in the axial direction of each joint, which is lumped into a constant joint stiffness, and 2) the robot's links are infinitely stiff.

It is common [12, 13, 25, 26, 38, 56, 57] to relate the robot stiffness in the Cartesian space $[K]$ to its stiffness in the joint space $[K_\theta]$ via the congruence transformation as follows:

$$[K] = [J(\theta)]^{-T}[K_\theta][J(\theta)]^{-1} = \left[[J(\theta)][K_\theta]^{-1}[J(\theta)]^{T}\right]^{-1} \tag{4}$$

Equation (4) is the conventional stiffness formulation used in prior work, first derived by Mason and Salisbury [58]. However, this formulation is only valid when the robot is in a quasi-static configuration with no external loading, or when its kinematic Jacobian matrix is constant throughout the robot workspace such as for a Cartesian robot [8, 9, 11, 18, 19].

In this thesis, the conservative congruence transformation (CCT) is utilized to account for the change in geometry via the differential Jacobian of the robot manipulators when an external force is applied. Conservative and consistent physical properties of stiffness matrices can be preserved during the CCT-based stiffness mapping regardless of the usage of coordinate frames and the existence of external force.

Although the CCT approach has been used in others applications [18-24], heretofore its significance in robotic machining has not been recognized and exploited. In this thesis, the effect of milling forces on the robot stiffness is accounted for via the CCT method as follows:

$$[K] = [J(\theta)]^{-T}[K_\theta - K_c][J(\theta)]^{-1} = \left[[J(\theta)][K_\theta - K_c]^{-1}[J(\theta)]^T\right]^{-1} \tag{5}$$

where $[K_c]$ is the additional stiffness term, which considers the effect of milling forces $[F]$ acting on the end effector, and is given by:

$$[K_c] = \underbrace{\left[\frac{\partial[J(\theta)]^{-T}}{\partial\theta_1}F \quad \frac{\partial[J(\theta)]^{-T}}{\partial\theta_2}F \quad \cdots \quad \frac{\partial[J(\theta)]^{-T}}{\partial\theta_{n-1}}F \quad \frac{\partial[J(\theta)]^{-T}}{\partial\theta_n}F\right]}_{n\times n} \tag{6}$$

where $\left[\frac{\partial[J(\theta)]^{-T}}{\partial\theta_i}F\right]$ is an $n \times 1$ column vector, with $i = 1 \cdots n$, and n is the number of joints.

3.3 Dynamic Robotic Milling Force Model

Figure 6 shows a schematic of the 2-dof dynamic model of the robotic milling system. The milling force model utilized here is an adaptation of Sutherland's steady state dynamic model for milling [5-7], where the dynamics of a long flexible end mill was modeled. However, in this thesis, the flexible end mill model is replaced with the robot structural dynamics model, as discussed in Section 2.1.

Similar to prior work on robotic milling [9-13, 38-40], the robot dynamic model considers instantaneous displacements in the *X* and *Y* directions. The 2-dof lumped mass-spring damper system assumption is valid when the axial depth of cut is small relative to the size of the vibrating structure (robot arm in this case) [5-7].

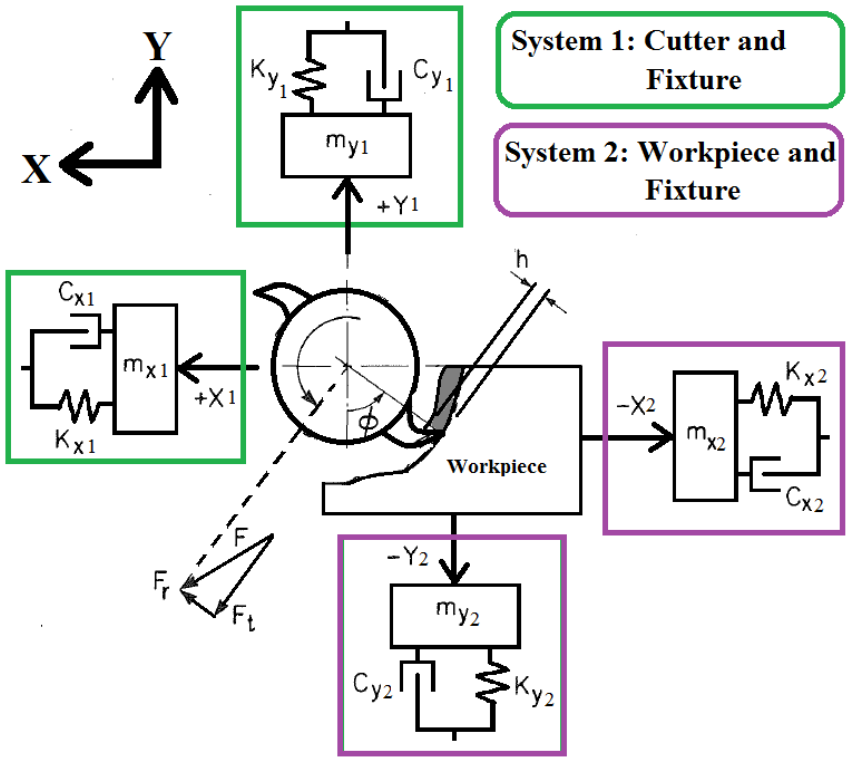

Figure 6. 2-dof simulation model for dynamic milling force computation.

The instantaneous forces acting on a cutter tooth engaged in the cut at a given axial location include the tangential force F_t and the radial force F_r, as shown in Figure 6 where the cutter is engaged in the cut at a rotation angle ϕ. The relationship between F_t and F_r is given by the following ratio:

$$F_r = r_c F_t \tag{7}$$

where r_c is an experimentally determined constant and F_t is calculated from:

$$F_t = K_{tc} b h \tag{8}$$

where the cutting coefficient K_{tc} is determined experimentally, b is the axial depth of cut, and h is the instantaneous uncut chip thickness obtained from the following expression [5-7],

$$h = c * sin\emptyset - Z_n + Z_{n(\min)} + \delta R \tag{9}$$

where c is the feed per tooth, Z_n is the vibration amplitude normal to the cut surface, $Z_{n(\min)}$ is the minimum surface undulation resulting from the prior cut at angle ϕ, and δR is the change in cutter radius due to runout. The instantaneous vibration Z_n is computed as follows:

$$Z_n = xsin\emptyset + ycos\emptyset \tag{10}$$

where x and y are the instantaneous displacements in the X and Y directions, respectively. The displacements can be calculated from the solution Δ of the structural dynamic model presented in Section 3.2 ($\Delta = xi + yj$ in the 2-dof dynamic model).

The dynamic milling force model is applied to a helical cutter by discretizing the axial depth of cut into thin slices perpendicular to the tool axis [5, 6]. Accordingly, Eq. (7) and (8) give the instantaneous forces acting on one cutter tooth at a particular axial slice. The total instantaneous force components F_x and F_y at cutter rotation angle ϕ can be obtained by integrating the resolved elemental forces in the X and Y directions over all axial slices and cutter teeth. In the following chart, F refers to the resultant milling force.

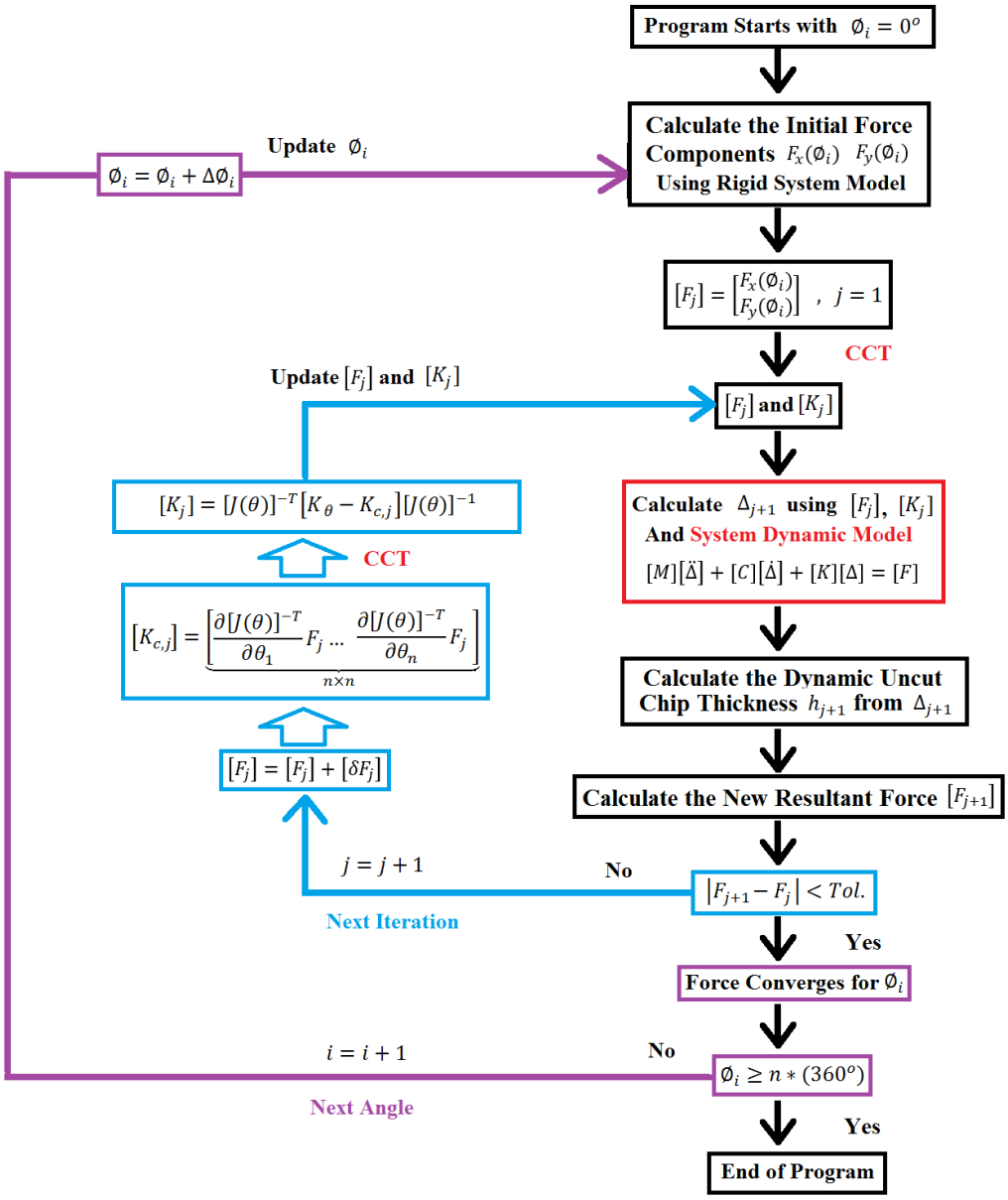

Figure 7. Algorithm for steady state chip thickness and dynamic cutting force determination.

Figure 7 presents a flow chart of the iterative approach used to calculate the instantaneous dynamic resultant forces in robotic milling. For given cutting conditions, the resultant milling force components and the robot stiffness matrix are calculated first

using the rigid model assumption. The resulting milling force and the stiffness matrix are substituted into the dynamic model to calculate the total system vibration Δ. The dynamic uncut chip thickness h is then estimated from Δ using Eqs. (9) and (10). The corresponding new resultant milling force is then calculated from the dynamic uncut chip thickness using Eqs. (7) and (8). Note that the algorithm must fully converge to the equilibrium or "steady state" dynamic uncut chip thickness at every cutter rotation angle.

Due to the dependence of the robot vibration on the process forces, which in turn depend on the robot vibration, the robot arm is not simply undergoing forced vibration. Similar to the work of Sutherland and DeVor [5], an iterative closed loop algorithm is implemented to compare dynamic milling forces obtained in the current iteration with the forces obtained in the previous iteration. If the difference is greater than a predefined threshold, the algorithm updates the cutting forces and the corresponding stiffness using the CCT-based stiffness model. The iterations continue until the difference is below the specified threshold, which is chosen as 1 percent in this thesis (similar to [5]). Therefore, the algorithm proceeds until the equilibrium or "steady state" dynamic uncut chip thickness at the current time instant is reached. This procedure is repeated for every cutter rotation angle. Note that the range of cutter rotation angles (defined by parameter n in Figure 7) should be large enough to capture the fundamental natural vibration frequency of vibration of the robot.

3.4 Experiments and Results

3.4.1 Joint Stiffness Identification

In order to verify the robotic milling dynamic effect model, the joint stiffness matrix of the robot arm needs to be experimentally determined. A common method for joint stiffness estimation is to identify the work zones where $[K_c]$ is negligible compared to $[K_\theta]$. The detailed identification procedure can be found in [25, 27, 56, 57]. Since $[K_c]$ increases with the external force magnitude, a small static load between $0 - 120\ N$ was selected to further minimize the effect of $[K_c]$. Therefore, Eq. (5) can be reduced to Eq. (4), which simplifies the joint stiffness calculation. Fifteen well-spaced robot configurations were chosen for the static stiffness tests, as shown in Table 1.

Table 1. Robot configurations for static stiffness tests. (Unit: degree)

No.	θ_1	θ_2	θ_3	θ_4	θ_5	θ_6
1	16	-51	45	-6	96	87
2	18	-47	57	-8	80	74
3	22	-42	55	3	77	92
4	27	-48	43	9	95	85
5	35	-63	47	-4	106	73
6	39	-52	44	10	98	82
7	41	-48	50	-12	88	96
8	47	-47	57	-8	80	95
9	54	-52	45	-21	97	77
10	68	-63	47	14	106	76
11	75	-52	44	-24	98	92
12	81	-48	45	8	93	84
13	86	-51	45	11	96	85
14	94	-47	57	9	80	93
15	103	-42	55	7	77	78

For each test, a given wrench $[W]$ (forces and moment) was applied to the robot end-effector and its elastic deformations $[\Delta X]$ (translations and rotations) were measured. The Cartesian stiffness matrix $[K]$ were then determined from the following equations:

$$[W] = [K][\Delta X] \tag{11}$$

$$[W] = [F_x \quad F_y \quad F_z \quad T_x \quad T_y \quad T_z]^T \tag{12}$$

$$[\Delta X] = [\delta x \quad \delta y \quad \delta z \quad \delta \alpha_x \quad \delta \alpha_y \quad \delta \alpha_z]^T \tag{13}$$

Finally, the joint stiffness $[K_\theta]$ was estimated from the conventional congruence transformation given by Eq. (4).

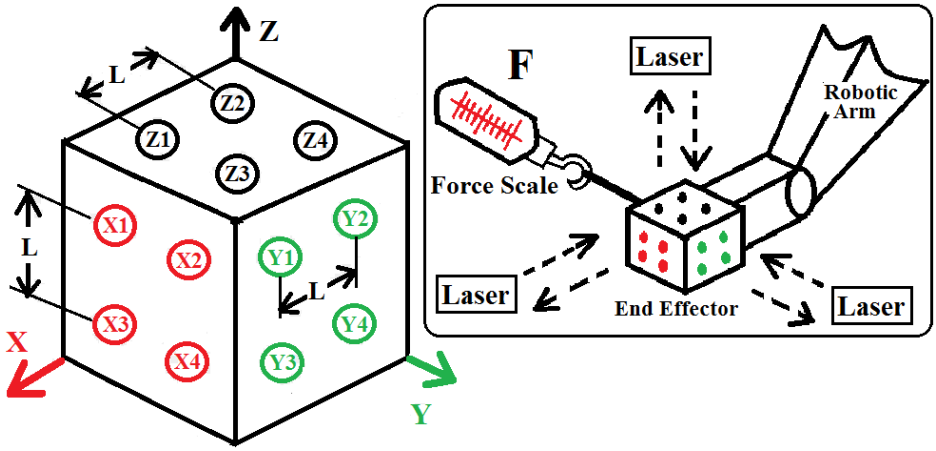

Figure 8. Schematic of experimental method for joint stiffness identification.

To measure the small deformations $[\Delta X]$ (translations and rotations), 12 measurement locations on the end effector were marked as shown in Figure 8. A force scale (1 N accuracy) was used to apply static forces to the end effector ranging from $0 -$

$120\ N$ in $20\ N$ increments, causing the end effector to deflect away from the original point. For each selected arm configuration, the Cartesian position of the robot end effector was recorded by a laser displacement sensor (Keyence LK-G37; 0.3 μm resolution) in the absence and presence of the applied load. The 6-dof deformations $[\Delta X]$ were then calculated using the following first approximations:

$$\delta x \approx (x_1 + x_2 + x_3 + x_4)/4 \tag{14}$$

$$\delta\alpha_x \approx \left[\tan^{-1}\left(\frac{z_3 - z_1}{L}\right) + \tan^{-1}\left(\frac{z_4 - z_2}{L}\right) + \tan^{-1}\left(\frac{y_3 - y_1}{L}\right) + \tan^{-1}\left(\frac{y_4 - y_2}{L}\right)\right]/4 \tag{15}$$

Equations (14) and (15) approximate the translations (δx), and rotations ($\delta\alpha_x$) along and about the X axis. The approximations for the translations and rotations along and about the Y axis, and along and about the Z axis, can be similarly written.

The difference between the unloaded and loaded measurements yielded the displacement of the end effector for an applied force vector. The joint stiffness values were then calculated from Eq. (4) and (11) using a least squares method, as shown in Table 1.

It must be noted that the Cartesian stiffness of the manipulator changes from one joint configuration to another. Figure 9 shows representative force-deflection curves obtained in the stiffness estimation tests.

According to Eq. (5), the Cartesian stiffness at the end effector should be nonlinear due to the $[K_c]$ term. The force-deflection curves however show an almost linear relationship in the chosen work zones, which confirms that $[K_c]$ is negligible in the

zones selected for joint stiffness identification. Therefore, without the nonlinear $[K_c]$ term, the joint stiffness in these zones can now be estimated using the conventional congruence transformation, namely Eq. (4) [25, 27, 56, 57], as shown in Table 2.

Table 2. Joint stiffness (Unit: 10^6 Nm/rad).

$K_{\theta 1}$	$K_{\theta 2}$	$K_{\theta 3}$	$K_{\theta 4}$	$K_{\theta 5}$	$K_{\theta 6}$
1.2	2.74	2.13	0.396	0.433	0.285

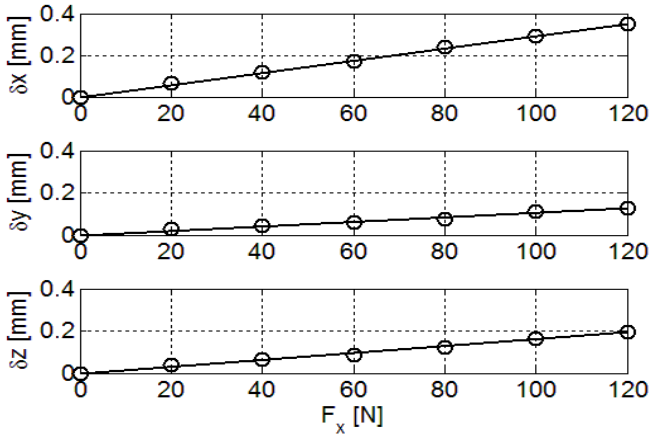

Figure 9. Force-deflection curves for Fx.

3.4.2 Robotic Milling Setup

The robotic milling testbed used for experimental validation consisted of a KUKA KR210 6-axis robot with a motorized spindle mounted to its end effector, as shown in Figure 10. Peripheral end milling experiments were performed on Aluminum 6061

workpieces. A 25.4 mm diameter uncoated tungsten carbide two flute square end mill with a 30 degree helix angle and 19 mm cutter length was used in all experiments.

A three-component quartz-based force dynamometer (Kistler 9257B) was used to measure the milling force components in the three orthogonal directions. Dry peripheral milling tests were performed for the following two robot arm configurations: (1) when the cutter is perpendicular to the horizontal (XY) plane (Cases 1 and 2), and (2) when the cutter is perpendicular to the vertical (XZ) plane (Cases 3 and 4). The robot base coordinate system is shown in Figure 10.

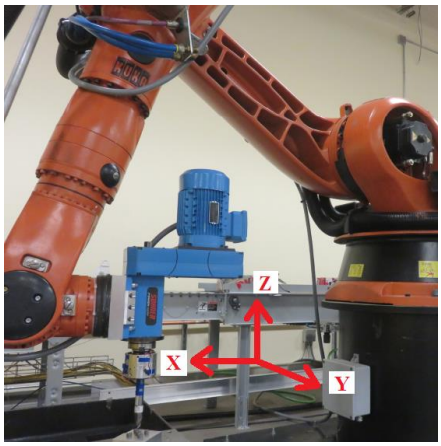

Figure 10. Robotic milling setup.

An impact hammer test using MetalMax TXF package was performed to find the natural frequency of the robotic milling system. The free vibration response of the robot was measured by impacting the tool tip. One example of the measured vibration response of the robot for the arm configuration used in Case 1 is shown below:

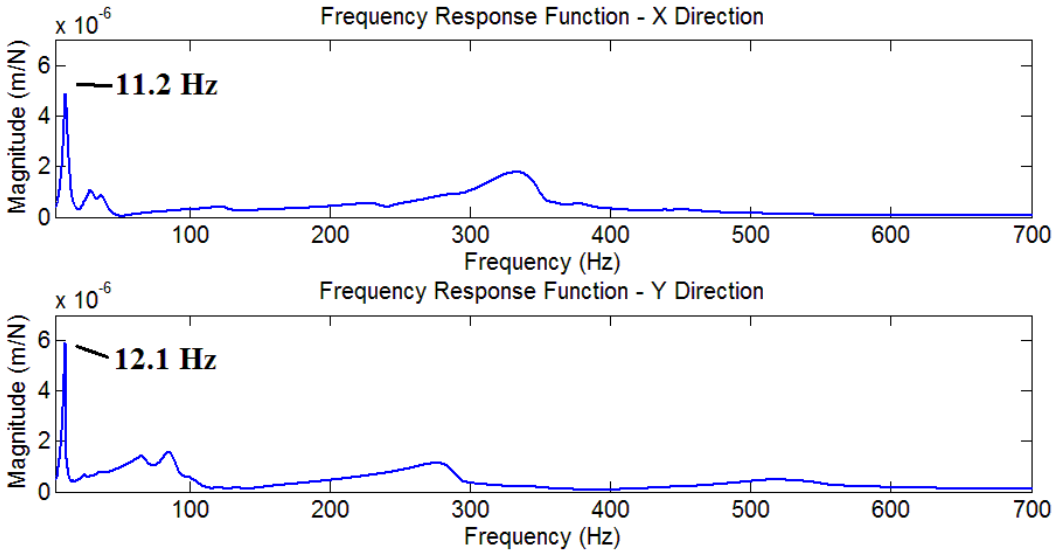

Figure 11. Impact hammer test result.

3.4.3 Results and Discussion

The peripheral milling experiments consisted of linear tool paths with constant radial and axial depths of cut at different feed rates. All tests were run at a constant spindle speed of 1000 rpm. The feed rate was limited by the spindle power and the payload of the robot used in this work (210 kg including the weight of the spindle). The radial depth of cut in all experiments was 15.24 mm. The robot configurations, axial depths of cut, feed rates, and directions used in the experiments are listed in Table 3.

Table 3. Cutting conditions, and experimental and simulation results.

Up milling Feed direction	**No.**	**Feed rate (mm/s)**	**Axial depth of cut (mm)**	Resultant Force (N) Experimental		Resultant Force (N) Simulation, 1st Iteration **[Error (%)]**		Resultant Force (N) Simulation, Converged **[Error (%)]**	
				F_{peak}	F_{PV}	F_{peak}	F_{PV}	F_{peak}	F_{PV}
Case 1 Horizontal $\mathbf{X_{robot}}$	1	1.2	3	151.2	22.4	164.5 **[8.8]**	38.1 **[70.1]**	148.1**[2.0]**	20.1 **[10.3]**
	2	1.6	3	180.3	26.8	196 **[8.7]**	46.2 **[72.4]**	176.2 **[2.3]**	23.8 **[11.1]**
	3	1.6	4	230.7	34.6	254.3 **[10.2]**	60.2 **[74.0]**	223.3 **[3.2]**	30.4 **[12.1]**
Case 2 Horizontal $\mathbf{Y_{robot}}$	4	1.2	3	137.2	20.3	143.1**[4.3]**	34.5 **[69.9]**	134.8 **[1.7]**	18.6 **[8.4]**
	5	1.6	3	163.2	24.7	172.3**[5.6]**	42.4 **[71.7]**	159.9 **[2.0]**	22.1 **[10.5]**
	6	1.6	4	219.2	32.3	232.4 **[6.0]**	55.7 **[72.5]**	213.5 **[2.6]**	28.7 **[11.1]**
Case 3 Vertical $\mathbf{-X_{robot}}$	7	1.2	3	147.2	42.8	165.9 **[12.7]**	73.9 **[72.6]**	141.7 **[3.7]**	37.7 **[12.0]**
	8	1.6	3	177.6	51.3	201.2 **[13.3]**	89.6 **[74.6]**	170.7 **[3.9]**	44.8 **[12.7]**
	9	1.6	4	236.3	68.1	271.8 **[15.0]**	120 **[75.3]**	226.5 **[4.1]**	58.9 **[13.5]**
Case 4 Vertical $\mathbf{-Z_{robot}}$	10	1.2	3	118.4	34.1	131 **[10.6]**	57.8 **[69.5]**	115.6 **[2.4]**	30.2 **[11.4]**
	11	1.6	3	143	41.8	159.1 **[11.1]**	71.3**[70.6]**	139.2 **[2.7]**	36.8 **[12.0]**
	12	1.6	4	223.1	54.6	250 **[12.1]**	94.1**[72.3]**	216.4 **[3.0]**	47.9 **[12.3]**

In order to validate the performance of the robotic milling dynamic force model, two criteria were selected, as shown in Figure 12b. The first criterion is the difference between the largest and smallest peaks of the resultant force (defined as the F_{PV}), which quantifies the dynamic effect. In order to minimize the effect of runout, F_{PV} is calculated by comparing the peaks in the resultant force for the same flute. This quantity is almost zero when the dynamic effect is small. Note that the effect of cutter runout is assumed to be negligible. It can be seen that F_{PV} increases significantly in the presence of robot vibration. The second criterion used is the peak cutting force (F_{peak}). The peak cutting force increases with the dynamic effect and is therefore an important factor to monitor to prevent overloading of the robot arm.

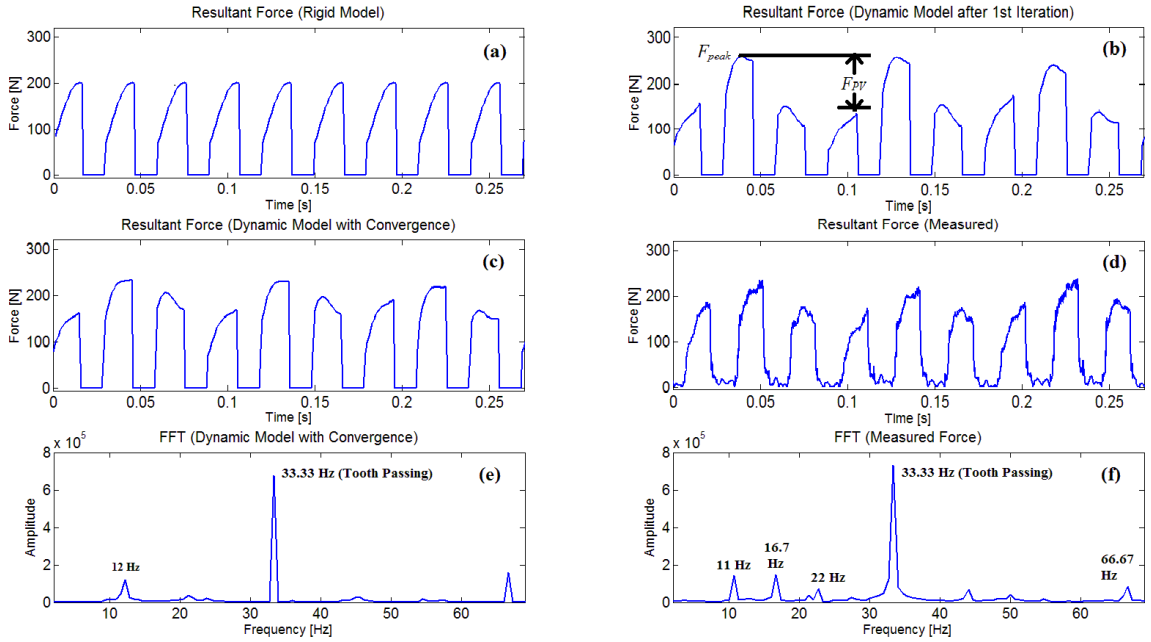

Figure 12. Experimental and simulation results for test # 9.

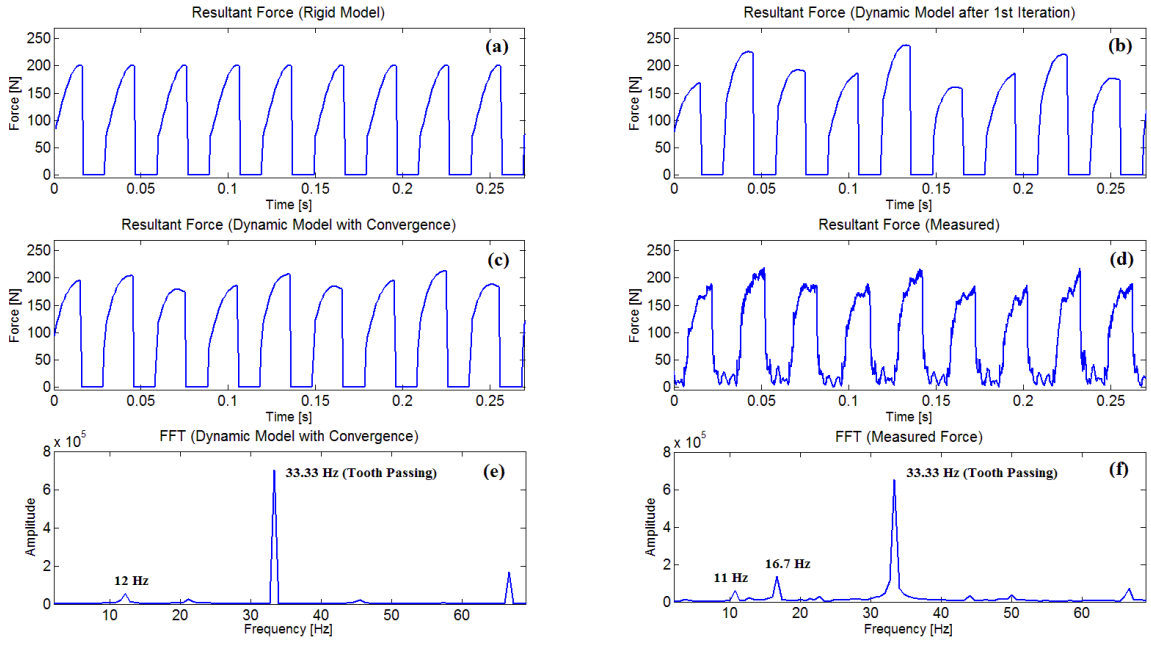

Figure 13. Experimental and simulation results for test # 6.

Figure 12 and Figure 13 show results for two cases – one where the effect of robot dynamics is significant (Figure 12) and one where it is insignificant (Figure 13). As shown in Figure 12a (test #9), F_{PV} is 0 and F_{peak} is ~200 N when the entire system is treated as perfectly rigid. After the 1st iteration of the dynamic force model, the simulation errors in F_{peak} and F_{PV} are 15% and 75.3%, respectively, as shown in Table 3 and in Figure 12b. The measured resultant force signal is shown in Figure 12d. Although some runout is present in the measured force signal, it can be seen from the force profile and the Fast Fourier Transform (FFT) spectra that F_{PV} is primarily due to the dynamic effect.

When not accounting for the equilibrium of the dynamic uncut chip thickness in the presence of the instantaneous robot deflection (i.e. after the 1st iteration of the algorithm), the resultant milling force is overestimated, which results in larger F_{PV} and $P_{peak.}$ After reaching the equilibrium (steady state) uncut chip thickness, the errors in F_{peak} and F_{PV} decrease significantly, as shown in Figure 12c. Table 3 shows the error in F_{peak} decreases by at least ~50% while the error in F_{PV} is reduced to 25% of its original value. This behavior is similar to that observed in conventional milling using a flexible cutter [5, 6]. According to Figure 12b-d, the steady state dynamic cutting force model matches the experimental results better, compared to the case when the equilibrium chip thickness is not considered (i.e. after only one iteration of the convergence algorithm).

In addition, the spectral decomposition of the simulated resultant force is in reasonable agreement with the spectral decomposition of the measured force. The natural frequency of the robot arm (~ 11 Hz) was identified through a modal impact hammer test. The effect of the robot arm's vibration on the uncut chip thickness is shown by both the

model and the experimental results. Therefore, the natural frequency and its harmonics are visible in the frequency decompositions. The natural frequency in simulation (~12 Hz) is slightly larger than the experimental value due to the absence of damping in the simulation model. In addition, note that a 16.7 Hz peak owing to spindle/cutter runout is present in the experimental data. The iterative model does not consider spindle/cutter runout, and therefore the 16.7 Hz peak is absent from the FFT of the simulated force profile. In general, the proposed steady state dynamic uncut chip thickness algorithm demonstrates better performance in all 12 experiments over a range of cutting conditions and arm configurations, as seen in Table 3.

The results in Table 3 also show the dynamic effect (and therefore the performance of the dynamic force model) varies considerably with cutting conditions and the robot arm configuration. For the same arm configuration but with different cutting parameters, the dynamic effect increases under more aggressive cutting conditions, which is reflected in the increase in F_{PV}. In addition, the corresponding error in the dynamic cutting force model increases with the dynamic effect, as seen in Tests (#1-3) for Case 1 (see Table 3). This may be due to the lumped mass spring system assumption that only considers vibration in two degrees of freedom while the robot arm is a continuous system with infinite degrees of freedom.

To determine the applicability of the static cutting force model in the robot's workspace, the dynamic effect of the corresponding robotic arm configuration was estimated. Using the robot dynamic model presented in Section 3.2, F_{peak} and F_{PV} can be estimated for different arm configurations at various points in the robot workspace. Figure 14 shows an example where the cutting conditions for Test #3 were examined. As

mentioned before, F_{PV} quantifies the dynamic effect and is equal to the difference between the largest and smallest peaks in the resultant force. Thus, F_{PV} is zero when there is no dynamic effect. Points in space where F_{PV} was larger than 10% of F_{peak} are marked in red. As seen in Figure 14, the F_{PV} is significant at points in the workspace where the robot arm configuration is characterized by low stiffness, which is consistent with previous findings [56, 57]. This suggests that the dynamic effect is significant in the red regions where the static cutting force model cannot be utilized.

Therefore, the simplified discrete model can be used a tool to estimate the dynamic effect of different arm configuration under different cutting conditions, and identify the region within the robotic workspace where static cutting force model may be used.

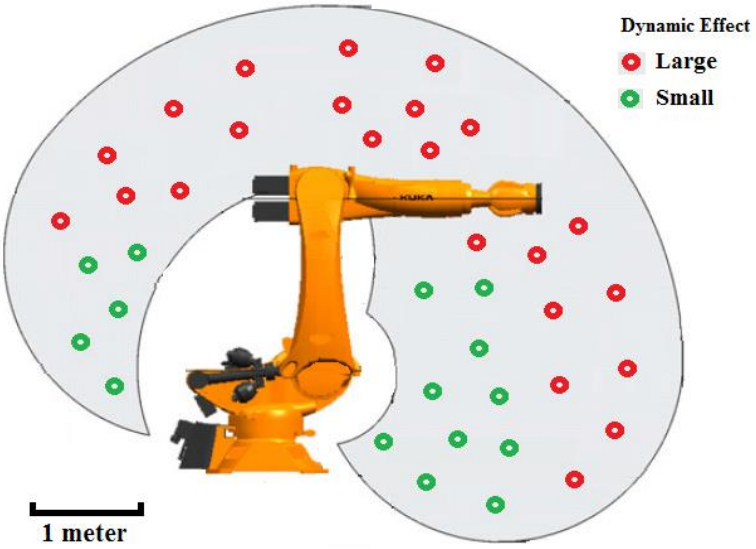

Figure 14. Simulation of the dynamic effect as a function of robot configuration using the cutting conditions for test #3.

3.5 Summary

In this chapter, the effect of robot structural dynamics on the forces produced in robotic milling was analyzed. For this purpose, a dynamic milling force model incorporating the effect of robot dynamics and the effect of external forces on the robot stiffness was developed and implemented. The force model leverages prior work on dynamic modeling of milling forces where the influence of system compliance on the equilibrium or "steady state" uncut chip thickness is accounted for using an iterative computation process. The force model presented here is an adaptation of Sutherland's steady state dynamic model for milling [5-7], where the dynamics of a long flexible end mill was modeled. Instead, in this thesis, the flexible end mill model is replaced with the robot structural dynamics model. In addition, the effect of milling forces on the robot arm stiffness was accounted for using the Conservative Congruence Transformation (CCT).

Compared to the dynamic model using only the first iteration (i.e., non-equilibrium uncut chip thickness condition), the iterative approach showed reductions of up to 50% and 75% in the errors for F_{peak} and F_{PV}, respectively. This chapter also analyzed the significance of the robot dynamics effect on the resultant milling force as a function of the robot configuration (pose) and cutting conditions, which can help in selecting the proper arm configuration with negligible dynamic effect, where the static cutting force model can be utilized.

Note that the dynamic effect is less for conservative cutting conditions and relatively stiff arm configurations. In such cases, the static cutting force model may be acceptable. Due to the complexity in developing a continuous dynamic model for the robotic arm structure and the limitation in the robot controller (12 ms cycle time for the Kuka KR210 used in this work), the experiments in the following chapters are conducted in the regions where the dynamic effect is negligible, and therefore the static cutting force model can be used. This assumption is similar to the majority of robotic milling work reported in the literature [8-11, 25-31].

CHAPTER 4. A WIRELESS FORCE SENSING AND MODEL BASED APPROACH FOR ENHANCEMENT OF MACHINING ACCURACY

4.1 Introduction

This chapter presents a new method to increase the accuracy of robotic milling while preserving its flexibility. The approach does not require any position sensor or explicit analysis of the robot compliance. Instead it employs an in-situ thin film wireless force sensor to measure in real-time the milling forces. The real time milling force signals are utilized in a mechanistic milling force model to estimate the instantaneous cutter engagements for direct tool position compensation feedback. Articulated-arm robotic milling experiments are conducted to validate the concept. The work presented in this chapter has also been reported in the author's paper [59]. In this thesis, the effects of cutter deflection and any pre-existing cutter tilt are assumed to be negligible.

4.2 Methodology

In this chapter, a new approach is proposed to overcome the accuracy limitations of robotic milling. The approach employs an in-situ thin film wireless force sensor to measure in real-time the milling forces. The real time milling force signals are input to a mechanistic milling force model to estimate the instantaneous radial (a) and axial (b) cutter engagements for static deflection error compensation feedback, as summarized in Figure 15. The essence of the new robotic milling position feedback algorithm proposed here is based on the existence of the following two physical relationships:

(1) A physical relationship between the dynamic strains (deflections) produced in the milling cutter and the X and Y milling forces (Function 1 in Figure 15). More details are given in Section 4.2.1.

(2) A physical relationship between the X and Y milling forces and the instantaneous radial and axial cutter engagements with the workpiece (Function 2 in Figure 15). More details are given in Section 4.2.2.

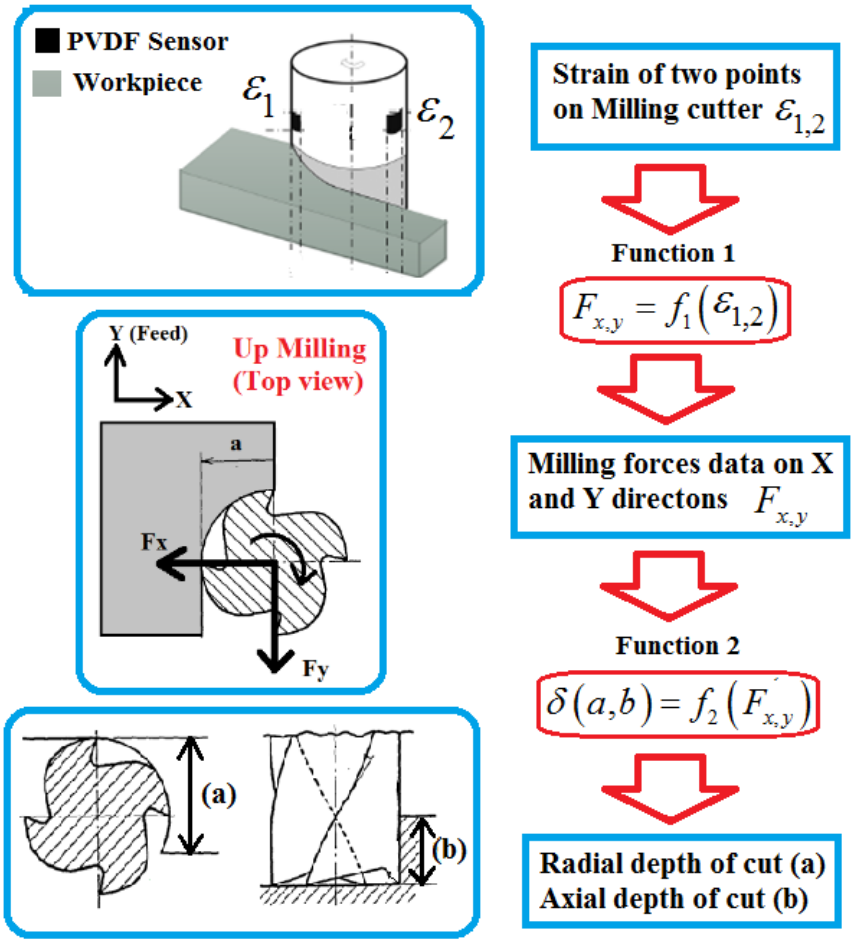

Figure 15. Physical relationships governing milling force model based compensation method.

4.2.1 Wireless PVDF Sensor System

This work is an extension of prior work on Polyvinyldene Flouride (PVDF) sensor based monitoring of milling forces [60].

Current state-of-the-art for accurate measurement of cutting forces in milling operations includes rotating or platform type piezoelectric quartz dynamometers. However, these dynamometers suffer from several limitations, such as limited frequency bandwidth (with typical resonant frequencies of 2–4 KHz), reduction in the dynamic stiffness of the machine tool system upon introduction into the machining system, large size, and high cost [60].

Thin film PVDF sensors possess the characteristics required for dynamic surface strain measurement, such as high dynamic range (up to 2% strain), fast response, and high strain sensitivity (~ 10 mV/με). In addition, they possess a wide frequency bandwidth (with resonant frequencies above 10 MHz), and low cost (about $5 per sensor) [30]. The signal to noise ratio for the PVDF sensor system used in this work is around 19.2.

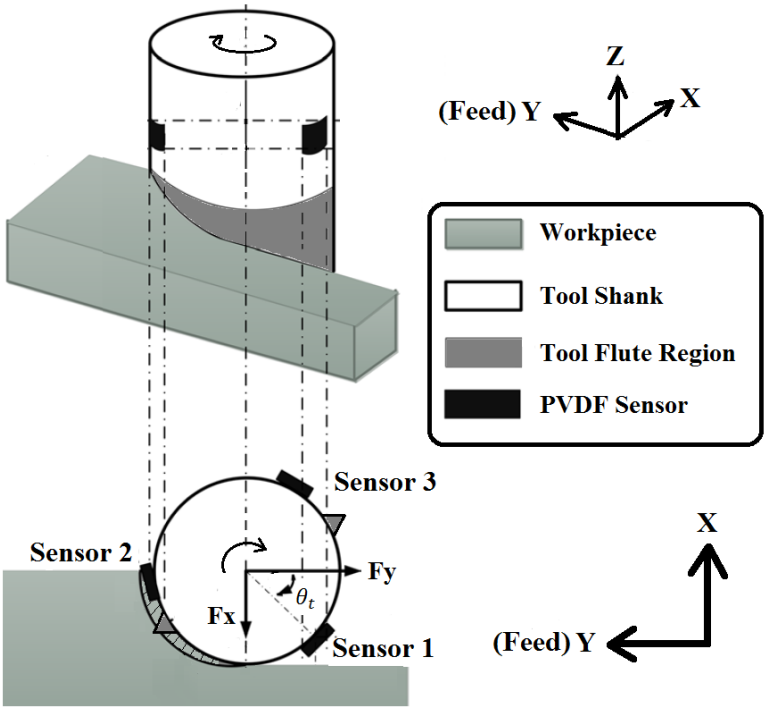

Figure 16. Schematic of PVDF sensor deployment in peripheral end milling process.

A piezoelectric PVDF sensor rosette, developed in prior work [60], was glued to the shank of the end mill (see Figure 16 and Figure 17) to measure the time-varying bending strains generated in the tool by the cutting forces. The cutting forces acting at the free end of the milling cutter elastically deform the tool and the PVDF sensor rosette produces electric charges corresponding to the elastic strains generated in the tool at the sensor location due to the piezoelectric effect. The charges are then converted into voltage signals using an on-board charge amplifier, whose output is transmitted through an anti-aliasing filter before being sampled by the embedded microcontroller unit, which wirelessly transmits the sampled signal. The signal conditioning electronics, polymer lithium ion battery and wireless transmission hardware (IEEE 802.15.4 standard protocol) were mounted on the tool holder into which the end mill was inserted (see Figure 17).

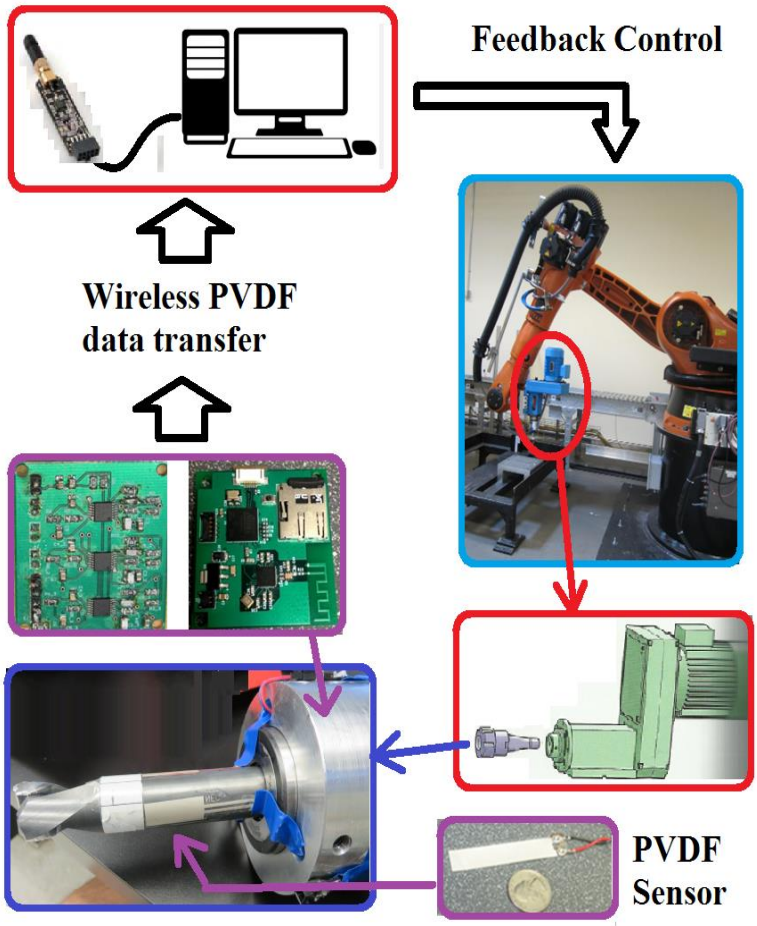

Figure 17. Hardware for robotic milling setup with wireless PVDF sensor system.

To accurately measure the cutting forces, the transfer function between the discrete time voltage samples and the forces was modeled as described in detail elsewhere [60]. In order to compensate for the distortion introduced by the signal conditioning circuitry and to recover the original magnitude and shape of the force signal, a discrete time finite impulse response (FIR) compensation filter was used to process the PVDF sensor signals [60].

To measure the feed and transverse force components (F_x and F_y) in peripheral end milling, at least two PVDF sensors are needed to mathematically relate the

feed/transverse force to the charge generated by the PVDF sensors. As shown in Figure 16, a strain gauge rosette design consisting of three PVDF sensors, which are mounted 120 degrees apart on the tool shank, was used to increase the robustness of the measurement system.

Treating the end mill as a cantilever beam clamped in the tool holder and assuming the Euler–Bernoulli beam theory is applicable, the bending strain generated in the tool at the location of the PVDF sensor i ($i = 1, 2, 3$) can be found using the bending formula [60]:

$$\varepsilon_i = -\frac{32L_p\left[F_y \cos(\theta_t + \theta_{ti}) + F_x \sin(\theta_t + \theta_{ti})\right]}{E_t \pi D_o^3} \qquad (i = 1, 2, 3) \tag{16}$$

where $L_p$is the axial distance from the idealized concentrated feed/transverse force to the center of the PVDF sensor, E_t is the Young's modulus of the end mill, D_0 is the shank diameter of the end mill, $\theta_{t1} = 0\ deg$, $\theta_{t2} = 120\ deg$, $\theta_{t3} = 240\ deg$, and θ_t is given by

$$\theta_t = \omega_o t + \theta_{to} \tag{17}$$

where ω_o and θ_{to} are the angular velocity of the end mill and the initial angular position(s) of the sensor(s), respectively.

Following the derivation in [60], the feed and transverse cutting force components (F_x and F_y) can be determined from the PVDF sensor voltage signals ($V_{p1,2,3}$), as follows:

$$\begin{bmatrix} V_{p1} \\ V_{p2} \\ V_{p3} \end{bmatrix} = \begin{bmatrix} C_{11}(\theta) & C_{12}(\theta) \\ C_{21}(\theta) & C_{22}(\theta) \\ C_{31}(\theta) & C_{32}(\theta) \end{bmatrix} \begin{bmatrix} F_x \\ F_y \end{bmatrix} \tag{18}$$

Note that the coefficient C_{ij} in (18) depends on the tool angular position θ. According to (17), the initial angular position of the tool is crucial for determination of the coefficient matrix. Since fast calculation is essential for feedback control, an algorithm to automatically detect the angular position of the tool corresponding to the peak force was implemented, which can be used to fix the initial tool angle for each data period. Figure 18 shows the steps involved in computing the milling forces using the measured PVDF sensor data.

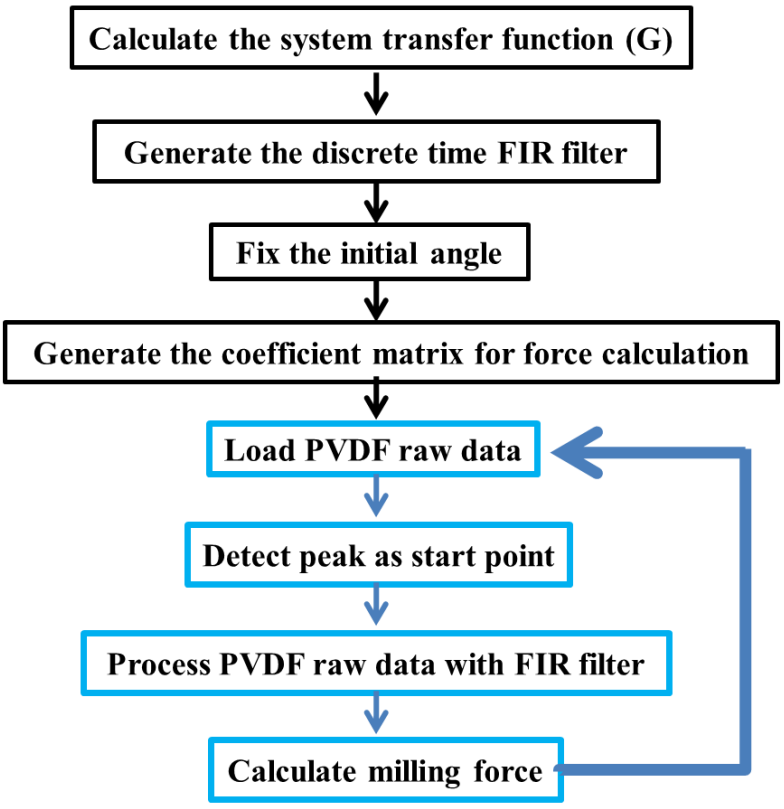

Figure 18. Procedure for determining the milling forces from PVDF sensor data.

4.2.2 Milling Force Model Based Feedback Loop

Using a well-established milling force model, it is possible to derive semi-analytical expressions for the average end milling forces [55]. An end mill with *N* flutes is assumed in the model. The immersion angle $\emptyset$ in the model is measured clockwise from the $(-X)$ axis, as shown in Figure 19.

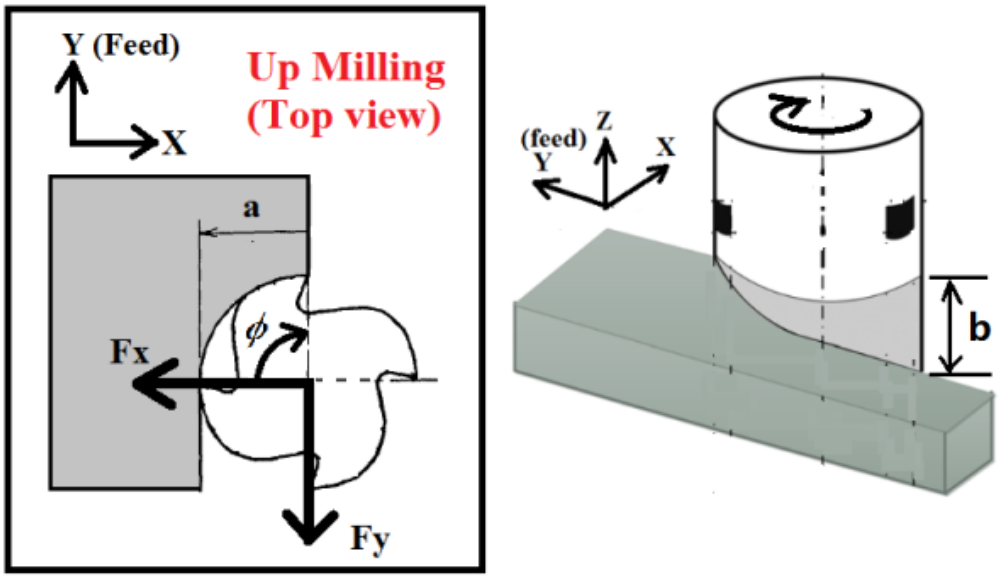

Figure 19. Coordinate system for the up milling process.

Cutter runout was assumed to be negligible. Since the flute cuts only within the immersion zone ($\emptyset_{st} \leq \emptyset \leq \emptyset_{ex}$), integrating the differential cutting forces (dF_x and dF_y) over one revolution along the axial depth of cut and then dividing by the pitch angle ($\emptyset_p = 2\pi/N$) yields the average milling forces per tooth period [55, 61-63]:

$$\overline{F_x} = \frac{1}{\emptyset_p} \int_{\emptyset_{st}}^{\emptyset_{ex}} \int_{z_1}^{z_2} dF_x(\emptyset, z) d\emptyset \tag{19}$$

$$\bar{F}_y = \frac{1}{\emptyset_p}\int_{\emptyset_{st}}^{\emptyset_{ex}}\int_{z_1}^{z_2} dF_y(\emptyset, z)d\emptyset \tag{20}$$

where z_1 and z_2 are the lower and upper axial engagement limits of the portion of the milling cutter engaged in cutting. For a general square end mill application, the average milling forces can be calculated from Equations (4-5) as follows [55]:

$$\bar{F}_x = \frac{Nbc}{8\pi}[-K_{rc}\cos 2\emptyset - K_{tc}(2\emptyset - \sin 2\emptyset)]_{\emptyset_{st}}^{\emptyset_{ex}} + \frac{Nb}{2\pi}[K_{te}\cos\emptyset + K_{re}\sin\emptyset]_{\emptyset_{st}}^{\emptyset_{ex}} \tag{21}$$

$$\bar{F}_y = \frac{Nbc}{8\pi}[K_{tc}\cos 2\emptyset - K_{rc}(2\emptyset - \sin 2\emptyset)]_{\emptyset_{st}}^{\emptyset_{ex}} + \frac{Nb}{2\pi}[-K_{te}\sin\emptyset + K_{re}\cos\emptyset]_{\emptyset_{st}}^{\emptyset_{ex}} \tag{22}$$

where b is the axial depth of cut, c is the feed rate, the edge force coefficients are $K_{re}$and K_{te}, and the cutting force coefficients are K_{rc} and K_{tc}. Note that, in this thesis, all force coefficients are assumed to be constant.

Therefore, it is possible to solve for $\emptyset_{ex}$ from the ratio of the milling forces (since $\phi_{st} = 0\ deg$ for up-milling) as follows:

$$r = \frac{\bar{F}_y}{\bar{F}_x} = \frac{[cK_{tc}\cos 2\emptyset - cK_{rc}(2\emptyset - \sin 2\emptyset) + 4(-K_{te}\sin\emptyset + K_{re}\cos\emptyset)]_{\emptyset_{st}}^{\emptyset_{ex}}}{[-cK_{rc}\cos 2\emptyset - cK_{tc}(2\emptyset - \sin 2\emptyset) + 4(K_{te}\cos\emptyset + K_{re}\sin\emptyset)]_{\emptyset_{st}}^{\emptyset_{ex}}} \tag{23}$$

Finally, the instantaneous radial (a) and axial (b) depths of cut can be estimated from (21-22) and (23) as follows:

$$a = R(1 - \cos\emptyset_{ex}) \quad (24)$$

where R is the radius of the end mill.

Thus, a physical relationship exists between the strains produced in the cutter and the instantaneous radial and axial cutter engagements through the milling force model. As shown in Figure 20, using the PVDF sensor system, the actual radial and axial depths of cut can be estimated from the above milling force model. Based on these estimates, the difference between the actual and commanded positions of the end effector can be minimized using the position feedback loop as shown in Figure 20.

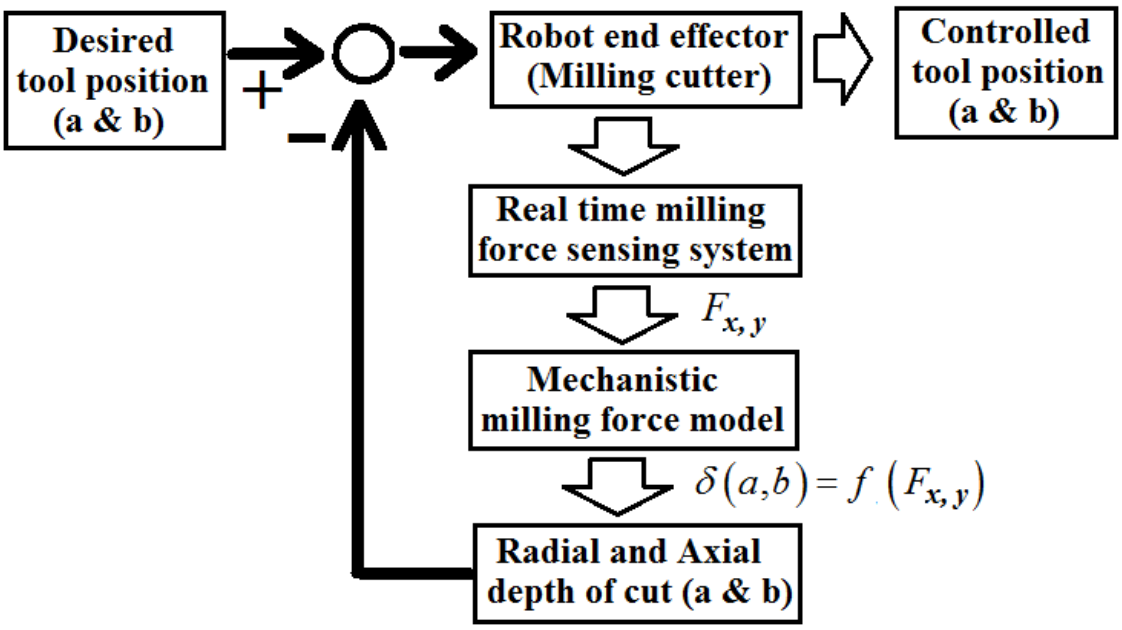

Figure 20. Flow chart of the milling force model based compensation method.

For full immersion milling (slotting), if there is no change in the radial depth of cut, the method proposed in this thesis will only work for compensating static deflection errors in the axial depth of cut. Equations (19-20) also work for other types of end mills, such as ball end mills [61-65]. The two average force components ($\bar{F}_x$ and $\bar{F}_y$) can be

used to solve for the axial and radial depths of cut in general cases when the lower axial engagement z_1 and one of the immersion angles ($\emptyset_{st}$ or $\emptyset_{ex}$) are known.

For special cutting conditions when none of the cutter engagement parameters (z_1, z_2 , $\emptyset_{st}$, $\emptyset_{ex}$) are known, the cutter engagement needs to be estimated from the instantaneous force components. The instantaneous force component for rotational positon $\emptyset$ is as follows [55, 61, 62]:

$$F_q(\emptyset) = \sum_{j=1}^{N} \int_{z_{1,j}}^{z_{2,j}} F_{q,j}(\emptyset, \emptyset_{st}, \emptyset_{ex}, z)\, dz$$

$$= F_q(\emptyset, \emptyset_{st}, \emptyset_{ex}, z_1, z_2), \quad q = x, y, z \qquad (25)$$

where $z_{1,j}$ and $z_{2,j}$ are the lower and upper axial engagement limits of the in-cut portion of flute j.

After reading the rotational position $\emptyset$ from the encoder, at least four unique instantaneous force components are required to calculate the four unknown cutter engagement parameters (z_1, z_2, $\emptyset_{st}$, $\emptyset_{ex}$). Further elaboration of this aspect is left as future work since the focus of this thesis is on square end mills only.

4.3 Experiments and Results

4.3.1 Experimental Setup for Closed-Loop Robotic Milling

An industrial scale robotic milling test-bed was developed by attaching a spindle motor to the end effector of a 6-axis KUKA robot (KR210).

The end mill containing the PVDF sensor and wireless transmission electronics mounted on the tool holder was inserted into the chuck of the spindle motor. In order to realize fast feedback control and to lower the workload of the KUKA robot controller, an external PC was utilized to run the feedback algorithm separately and communicate with the robot controller. Unlike other research groups who have used serial connection, Ethernet was chosen to ensure high transmission speeds. Cyclical data transmission between the robot controller and the external PC takes 12 ms.

However, the high transmission speed poses a challenge. The communication between the external PC and the KUKA robot controller can be quite unstable. In order to overcome this challenge, some research groups have utilized two PC's simultaneously to ensure high transmission speeds (one for feedback control and the other for communication with the robot) [66]. The milling force signal feedback requires fast communication with the KUKA robot. In the current work, one PC was used for running the static deflection error feedback control algorithm (see Figure 20), while the communication task with robot was handled by a C++ server program running inside the KUKA controller, as shown in Figure 21 and Figure 22. In principle, this method can provide faster and more stable communication with the KUKA industrial robot. The system implementation utilized three different programming languages: (1) KUKA Robot Language (KRL) for controlling the robotic arm, (2) C++ Server program for communication between the PC and the KRL-written client program, and (3) MATLAB for executing the milling force model feedback algorithm. Note that the closed loop control could be significantly faster if programmed on the KUKA controller, but the programming and interfacing would be a major challenge.

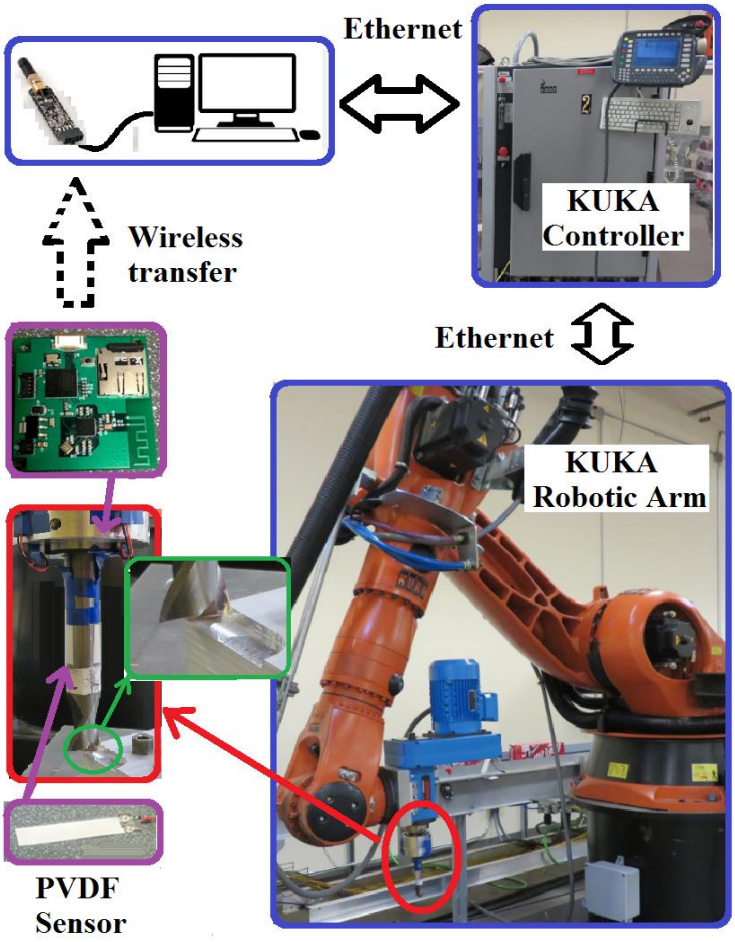

Figure 21. Experimental setup for closed-loop robotic milling.

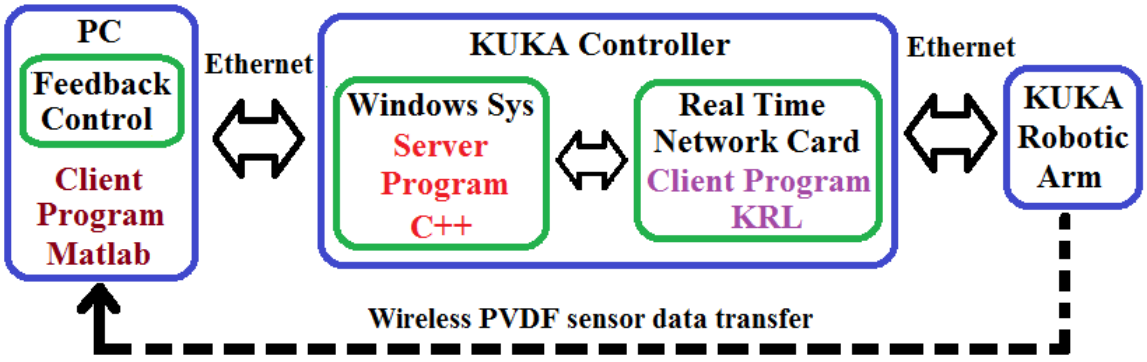

Figure 22. Closed-loop control communication system.

With the simplified calculation algorithm shown in Figure 18, and Equation (18) and Equations (23-24), the feedback calculation time in MATLAB was reduced significantly from 35 s to 0.02 s (compared to previous work [60]) for a PVDF data length of 0.25 s. During actual feedback control, there is a delay between the calculated and current cutter engagement due to the calculation time (at least 0.02 s in this work). This delay was assumed to be negligible when the axial and radial depths of cut are constant. When the axial and radial depths of cut vary continuously along the tool path, faster calculation times are required to minimize the delay mismatch. The delay time requirement depends on how rapidly the axial and radial depths of cut vary along the tool path, which is also a common problem for all other robotic milling feedback control approaches (both sensor-based and model-based).

Similarly, as the spindle speed or the number of flutes increases, the tooth passing frequency of the milling force increases, which then requires a faster calculation time. The external PC should be able to calculate the ratio of the cutting force components at least twice as fast as the tooth passing frequency. For the following experiments, a general purpose PC with Intel Core i7 was utilized. The total delay time for the closed loop system employed in this work is 0.27 s.

4.3.2 Results and Discussion

In this section, the results of the proposed robotic milling static deflection error feedback control strategy are presented and discussed. A block of Aluminum 6061 was used as the workpiece material for the peripheral end milling experiments. A 25.4 mm diameter two flute tungsten carbide square end mill with a 30 degree helix angle and

19.05 mm cutter length was used. The cutting coefficients were estimated using the mechanistic approach discussed in [55] and were found to be as follows: $K_{tc} = 9.04 \times 10^8\ N/m^2$, $K_{rc} = 2.94 \times 10^8\ N/m^2$, $K_{te} = 6.09 \times 10^3\ N/m$, $K_{re} = 6.6 \times 10^3\ N/m$.

The motorized spindle mounted on the end effector of the robot was operated at a constant spindle speed of 1000 RPM. The feed rate was limited by the spindle power and the payload of the robot used in this work. Therefore, relatively conservative cutting conditions were used in the experiments. A total of 15 dry peripheral milling tests, listed in Table 3, were conducted on the robotic milling setup. Figure 23 shows the schematic of the up-milling coordinate system. A scanning type coordinate measuring machine (CMM) (Hexagon Metrology) was used to measure the machined surface profile parallel to the YZ plane. As shown in Figure 23a, the ideal radial depth of cut (without overcut) was selected as the reference for the X coordinate. The Z reference surface was chosen to be 0.8 mm below the top surface of the workpiece (see Figure 23c). This amounted to a total of 16 scans, separated by 0.05 mm along the axial depth of cut (from Z= 0 to Z = 0.8 mm). Each CMM scan was made on the surface containing X_1 and X_2 (see Figure 23c) in the feed direction (Y) with a scan increment of 10 points per mm. All measured points along each scan were averaged to obtain the mean X coordinate value, which represents the actual radial depth of cut at each Z level (axial depth of cut), as shown in Figure 24 - Figure 26.

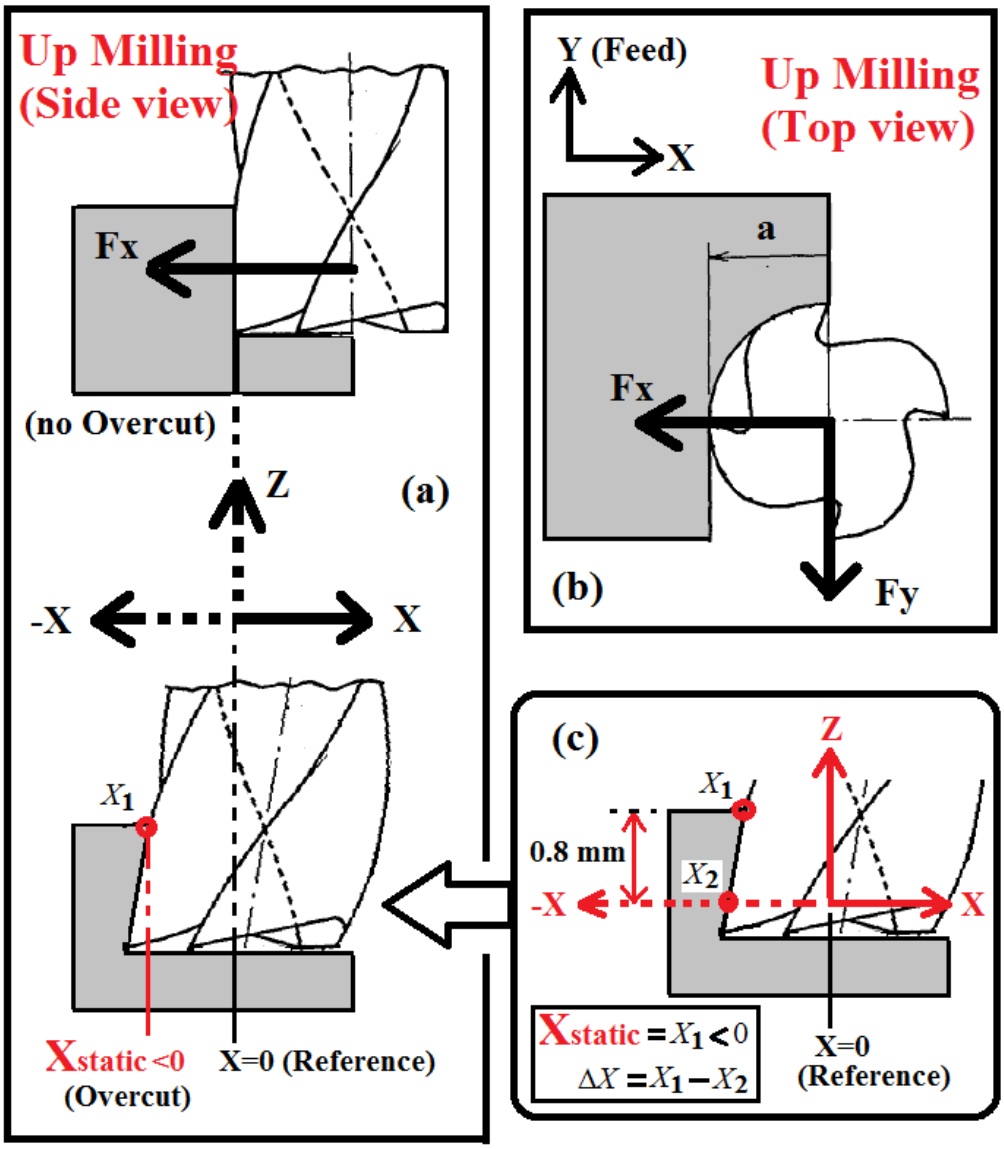

Figure 23. Schematic of the up-milling coordinate system.

Table 3. Cutting conditions and experimental results.

Test no.	Immersion ratio (%)	Axial Depth of cut (mm)	Feed rate (mm/s)	Static error X_{static} (mm)	Bending error ΔX (mm)	Standard deviation (mm)
Experiment **set 1**						
1	40	2.54	0.71	-0.0355	0.0088	0.0063
2	40	2.54	1.0	-0.0576	0.0155	0.0065
3	40	2.54	1.14	-0.0754	0.0169	0.0073
4	**40**	**2.54**	**1.27**	**-0.0945**	**0.0212**	**0.0079**
5 (feedback)	**40**	**2.54**	**1.27**	**-0.0206**	**0.0103**	**0.0064**
Experiment **set 2**						
6	20	5.08	0.8	-0.0654	0.0191	0.0068
7	20	5.08	0.9	-0.0731	0.0241	0.0070
8	20	5.08	1.0	-0.0803	0.0285	0.0073
9	**20**	**5.08**	**1.1**	**-0.0907**	**0.0328**	**0.0082**
10 (feedback)	**20**	**5.08**	**1.1**	**-0.0212**	**0.0089**	**0.0061**
Experiment **set 3**						
11	20	6.35	0.6	-0.0671	0.0056	0.0057
12	20	6.35	0.7	-0.0781	0.0062	0.0069
13	20	6.35	0.8	-0.0891	0.0076	0.0070
14	**20**	**6.35**	**0.9**	**-0.0996**	**0.0124**	**0.0076**
15 (feedback)	**20**	**6.35**	**0.9**	**- 0.0223**	**0.0079**	**0.0062**

As shown in Figure 23, the ideal cut surface should be at $X = 0$ if both the robotic arm and milling cutter are infinitely stiff (i.e. no translation or bending). However, in reality, under the action of the average milling force (F_x) there is translation (due to static deflection error of the robot structure) and bending of the milling cutter. Therefore, the total surface error consists of the sum of the robot static deflection error and the tool bending error. The static deflection error is approximated by X_1, which represents the

deviation of the cut surface from the nominal radial depth of cut measured at the top of the cut surface whereas ΔX represents the tool bending error, as shown in Figure 23c.

In the absence of position compensation of the static robot deflection and tool bending errors, an overcut occurs as seen in the results shown in Figure 24 - Figure 26. This can be explained by the up-milling force diagram in Figure 23b. The up-milling force component (F_x) pulls the milling cutter into the workpiece, thus removing excess material relative to the commanded position. Therefore, the static robot deflection error is always negative.

For comparison, the surface error produced in a CNC milling machine (which is considerably stiffer than the robot) at the highest feed rate (for each experiment set) is also included in Figure 24 - Figure 26. Comparing the surface error generated in the robotic milling experiment with the CNC milling test, it can be seen that the surface error in the robotic milling experiment without feedback compensation is quite large and increases with the feed rate. For the same cutting conditions, the surface error in robotic milling without feedback compensation is almost 30 times more than in CNC milling. In addition, the static deflection error increases significantly with increase in the feed rate and/or the axial depth of cut. Therefore, the low stiffness of the robotic arm makes the corresponding static deflection errors very sensitive to the milling force.

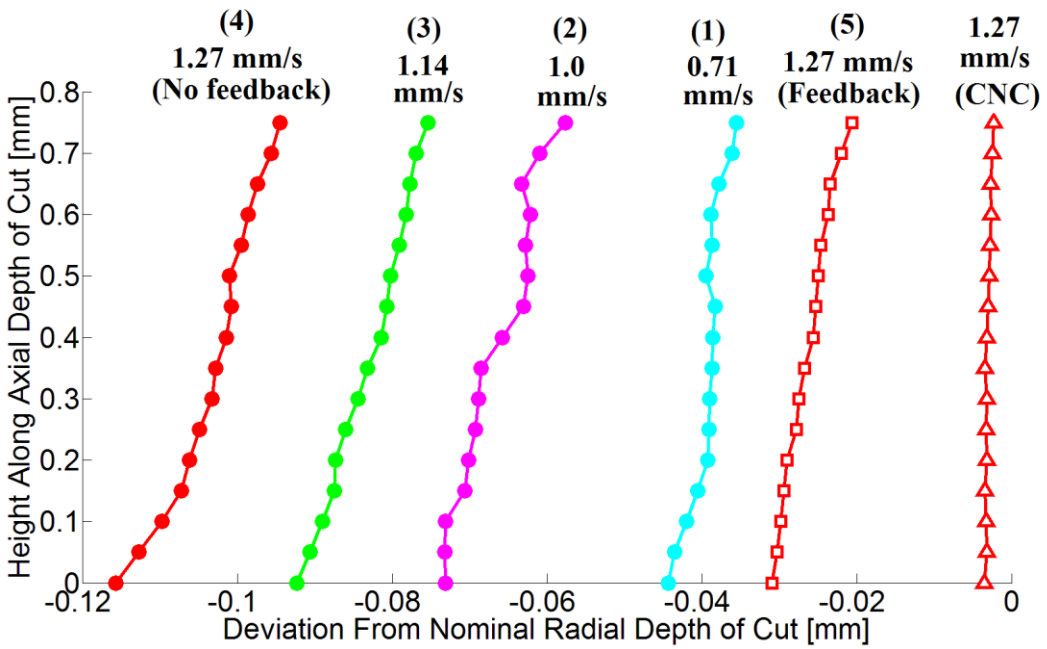

Figure 24. Robotic milling results for experiment set 1.

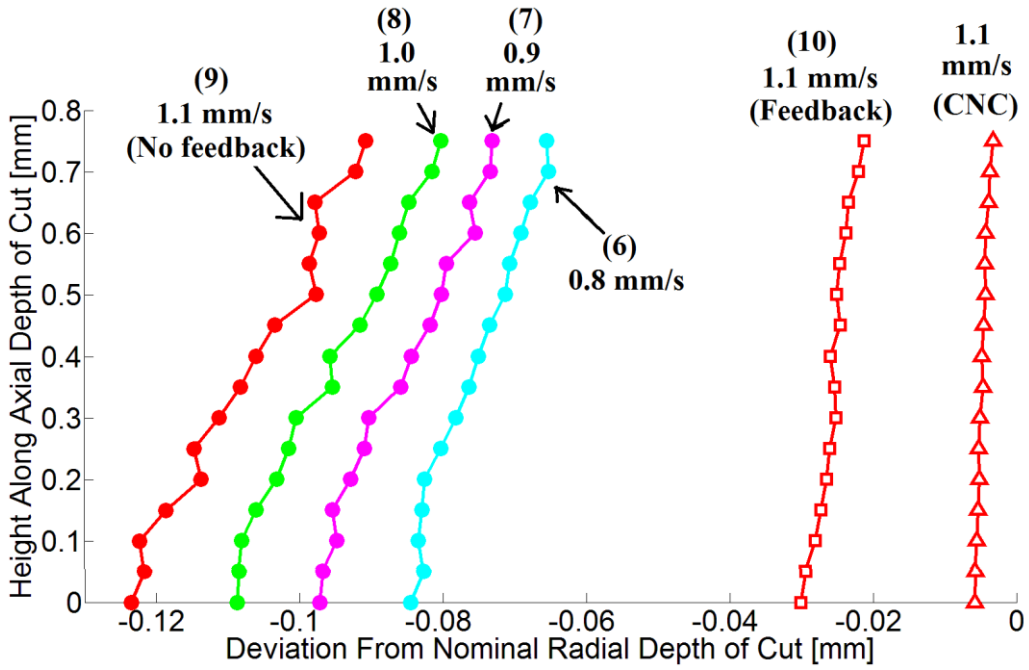

Figure 25. Robotic milling results for experiment set 2.

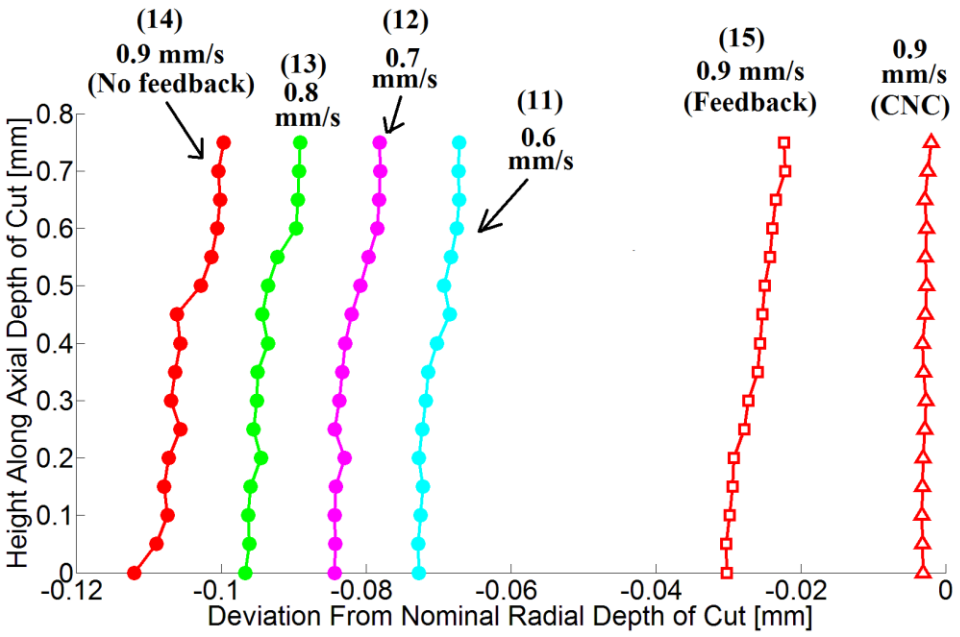

Figure 26. Robotic milling results for experiment set 3.

As for the tool bending error, a similar phenomenon occurs as the feed rate or the axial depth of cut increases. Comparing the tool bending errors produced in the robotic milling tests (Test #4, #9 and #14) and in CNC milling under the same cutting conditions (see Figure 24-Figure 26), it can be seen that the tool bending errors in the CNC milling tests are almost negligible. This can be explained by the relatively higher stiffness of the milling cutter (approximately $2 \times 10^7\ N/m$, [60]) compared to the stiffness of the robot arm (around $10^5 \sim 10^6\ N/m$). The current closed loop feedback compensation mainly targets the static error due to the flexibility of the robot structure.

It can be seen from Tests #5, #10 and #15 that a significant reduction in the dimensional error is realized after applying the milling force model based static deflection error feedback control. For Test #5, the static error was reduced from 0.0945 mm to 0.0206 mm, a 78.2% reduction. Similar improvements of 76.6% and 77.6% were

obtained in Tests #10 and #15, respectively. The tool bending error after compensation was reduced by 51.4%, 72.8% and 36.3% for Tests #5, #10 and #15, respectively. This can be explained by the reduction in F_x due to feedback compensation, which decreases the radial depth of cut and hence the overcut.

4.4 Summary

In this chapter, a new hybrid method that combines wireless force sensing with a mechanistic model of the milling forces to enable improvements in the dimensional accuracy obtained in robotic milling was proposed. The approach does not require an expensive position sensor or time-consuming robot compliance modeling. Instead it employs an in-situ thin film wireless force sensor to measure in real-time the milling forces, which are input to a mechanistic milling force model to estimate the instantaneous cutter engagements for static deflection error feedback compensation. Different from prior work that utilized conservative cutting conditions or soft workpieces and small cutters, articulated-arm robotic milling experiments were conducted on aluminum workpieces to validate the concept. The experimental results showed improvements of over 70% in the cut surface dimensional error when the proposed static deflection error feedback control strategy was implemented.

CHAPTER 5. CCT-BASED MODE COUPLING CHATTER AVOIDANCE

5.1 Introduction

In this chapter, a new model is proposed for robotic milling chatter analysis by integrating the CCT-based stiffness term that accounts for the effect of milling forces on the robotic arm stiffness. In previous mode coupling chatter models, the angle γ between the maximum principal stiffness vector K_{max} and the milling force vector was only dependent on the workpiece orientation and the robot arm configuration.

The introduction of the CCT-based external force related stiffness term offers the possibility of adjusting the angle γ through modification of the stiffness vector K_{max} of the robot arm by changing the cutting conditions, which in turn changes the cutting forces. Since the stiffness of the robot arm can be adjusted by changing the cutting forces using the CCT-based stiffness model, the effect of cutting conditions on the angle γ can be simulated to determine the stability of the robotic milling system.

Based on the above strategy, a new approach is proposed in this chapter for mode coupling chatter avoidance in robotic milling. Different from the previous approaches that changed the tool feed direction or the workpiece orientation, this new approach presents a method for adjusting the cutting parameters so as to modify the robotic arm stiffness vector such that mode coupling chatter is avoided. In the following sections, the proposed methodology is presented with experimental verification and discussion.

5.2 Theory and Approach

5.2.1 Dynamic Model including the Effect of Cutting Forces

In prior work on mode coupling chatter [9-11], researchers usually simplified the analysis by ignoring the average cutting force component in the feed direction, F_{Zo}, which yields a 2-dof problem and a corresponding analytical solution. The average cutting force in robotic milling, however, is a 3D vector, which has three orthogonal force components in the feed, radial and axial depth of cut directions (see Figure 27). The feed direction is along the Z_o axis, while the radial and axial depth of cut directions are oriented in the X_o and Y_o directions, respectively. In prior work [9-11], very restrictive cutting conditions (or special cases) were selected to ensure that the average cutting force component F_{Zo} in the feed direction is much smaller than the force components in the radial and axial depth of cut directions (F_{Xo} and F_{Yo}). This allowed researchers to simplify the chatter analysis to a 2-dof problem by ignoring the average cutting force in the feed direction (F_{Zo}).

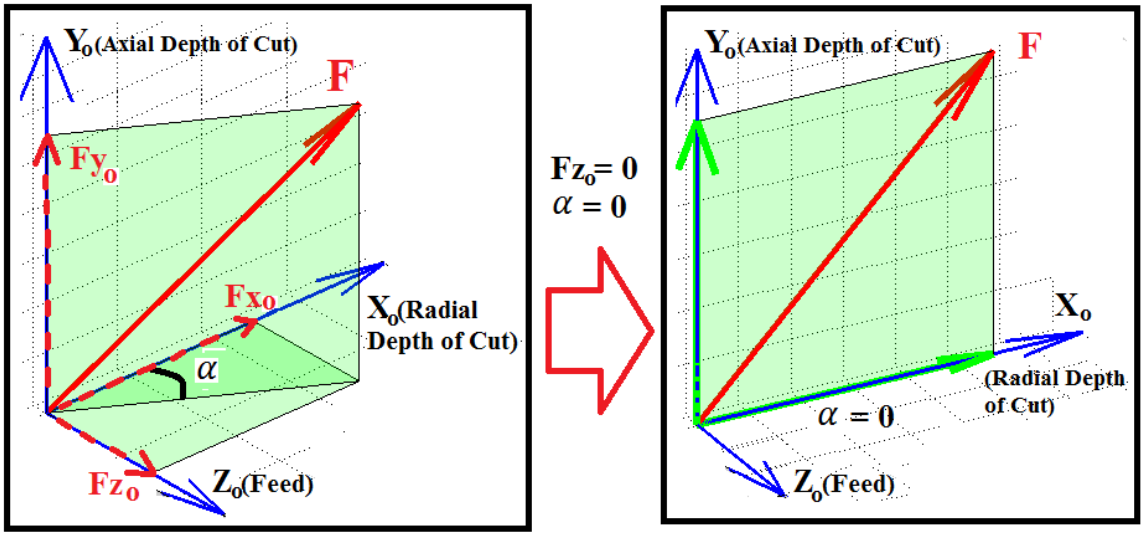

Figure 27. 2-dof simplification obtained by ignoring F_{Zo}.

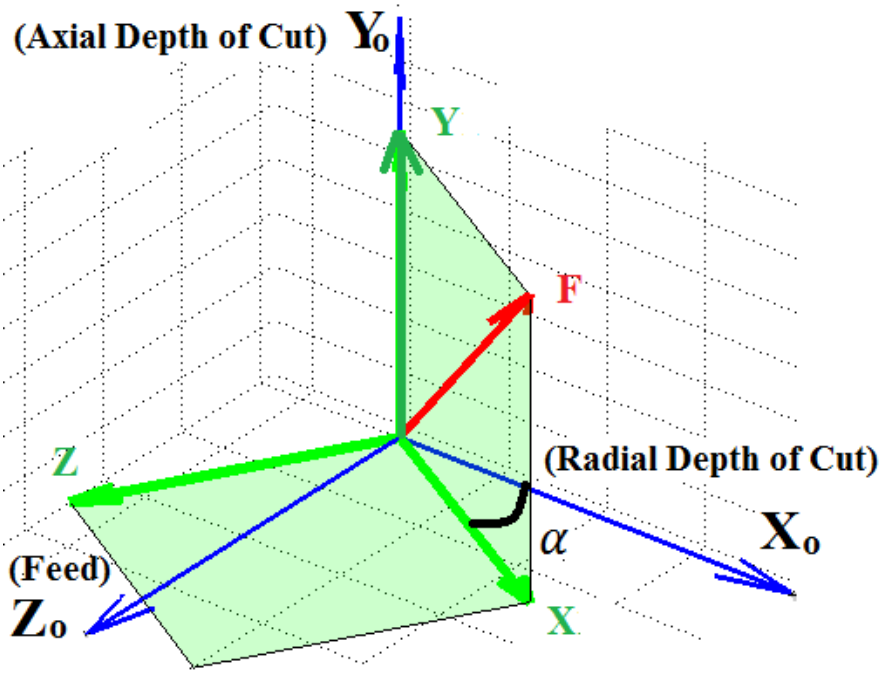

Figure 28. 2-dof simplification by rotating the stiffness matrix.

However, selecting a narrow range of cutting parameters to neglect F_{Zo} severely limits the flexibility and applicability of robotic milling. Therefore, in this thesis, the

reference frame of the robot stiffness model accounts for effect of the average cutting force component in the feed direction (F_{Zo}). This is accomplished by first calculating the tangent of the angle α (see Figure 27) from the ratio of F_{Zo} and F_{Xo}. Then a new coordinate system ($\Delta: XYZ$) is defined by rotating the original coordinate system ($\Delta_o: X_oY_oZ_o$) through α about the negative Y_o axis, as shown in Figure 28. The stiffness matrix $[K]$ in the new coordinate system can then be calculated from Equations (26)-(27), where α takes into account the effect of F_{Zo}:

$$\tan(\alpha) = \frac{F_{Zo}}{F_{Xo}} \tag{26}$$

$$[K] = [V_Y(-\alpha)]^{-1}[K_o][V_Y(-\alpha)] \tag{27}$$

where $[V_Y(-\alpha)]$ is the transformation matrix for the rotation through α about the negative Y_o axis and $[K_o]$ is the robot stiffness matrix defined in the original coordinate system ($X_oY_oZ_o$).

5.2.2 Criterion for Mode Coupling Chatter

The mode coupling chatter criterion is based on eigenvalue analysis of the dynamic model of the machining process. The basic approach was proposed and verified by Tobias et al. [41] for conventional machining and, more recently, has been used in robotic milling [9-11, 39, 40]. In these prior works, simplifying assumptions were made to derive an analytical solution for system stability. For example, Gasparetto [39, 40] assumed that the resultant cutting force direction is parallel to the workpiece surface. In this thesis, this assumption is relaxed and the eigenvalues are solved numerically.

The workpiece is assumed to be relatively stiff and its elastic deformation is ignored. Since structural and process damping always enhance the system dynamic stability and because they are difficult to determine accurately, this thesis assumes an undamped system. Similar to prior works on robotic milling [9-13, 38-40], the 2-dof dynamic system of equations without damping are:

$$[M][\ddot{\Delta}] + [K][\Delta] = [F] \tag{28}$$

where $[\Delta]$, $[M]$ and $[K]$ are the system coordinate vector, and the mass and stiffness matrices, respectively. Although these matrices are robot arm configuration (or joint angle $[\theta]$) dependent, for the purpose of analysis, the robot is assumed to move in a small range of joint angles such that the arm configuration can be considered to be invariant for the experiments reported in this chapter [9-13, 38-40].

The milling force model follows the common assumptions made in previous mode coupling chatter research including robotic milling [9-11, 39-41]. Prior work addressed mode coupling chatter stability by analyzing the angle between the average cutting force vector and the principal stiffness direction of the robot, which determines the proper orientation of the workpiece/machine for chatter avoidance. Specifically, the direction of the average cutting force is assumed to be constant and is determined by the nominal axial and radial depths of cut.

In mode coupling chatter analysis, the axial and radial depths of cut vary from their nominal values due to elastic deformation of the structure, which influences the magnitude of the average cutting force. The change in average cutting force magnitude

with respect to the deflection (dx, dy) from the nominal position (x_m, y_m) is denoted as $(d|\bar{F}|)_{(x_m,y_m)}$ in the following Equation (29):

$$\begin{aligned} |\bar{F}(x_m + dx, y_m + dy)| &= |\bar{F}(x_m, y_m)| + (d|\bar{F}|)_{(x_m,y_m)} \\ &= |\bar{F}(x_m, y_m)| + \left(\frac{\partial|\bar{F}|}{\partial x}dx + \frac{\partial|\bar{F}|}{\partial y}dy\right)_{(x_m,y_m)} \\ &= |\bar{F}(x_m, y_m)| + \left(K_{px}dx + K_{py}dy\right) \end{aligned} \quad (29)$$

Similar to the mode coupling chatter analysis of Tobias [41], the nominal position is selected as the reference position of the system so that $|\bar{F}(x_m, y_m)|$ can be disregarded in the dynamic system of equations, and the corresponding force model in the dynamic system of equations is $[d\bar{F}]$, as shown below:

$$d|\bar{F}| = \left(K_{px}x + K_{py}y\right) \quad (30)$$

$$[d\bar{F}] = \begin{bmatrix} d\bar{F}_x \\ d\bar{F}_y \end{bmatrix} = \begin{bmatrix} (cos\beta) * d|\bar{F}| \\ (sin\beta) * d|\bar{F}| \end{bmatrix} = \begin{bmatrix} (cos\beta) * (K_{px}x + K_{py}y) \\ (sin\beta) * \left(K_{px}x + K_{py}y\right) \end{bmatrix}$$

$$= \begin{bmatrix} K_{px}cos\beta & K_{py}cos\beta \\ K_{px}sin\beta & K_{py}sin\beta \end{bmatrix} \begin{bmatrix} x \\ y \end{bmatrix} = [K_p][\Delta] \quad (31)$$

where K_{px} and K_{py} are the cutting stiffnesses in the *X* and *Y* directions, which depend on the workpiece material and the cutting conditions. The cutting stiffness is defined as the sensitivity of $d|\bar{F}|$ due to small deflections in the x and y directions. For a specific robotic milling setup, the cutting stiffness is assumed to be constant [9-13, 38-40], which can be estimated using the mechanistic approach discussed in [55] and elaborated in Appendix A. For instance, K_{px} and K_{py} are $1.32 \times 10^3\ N/m$ and $-1.4 \times 10^4\ N/m$

respectively for a feed rate of 1 mm/s used in Case 1 (see Table 5). As mentioned in the previous assumption, $[d\bar{F}]$ is assumed to act in the same direction as the nominal average force vector $[\bar{F}]$, which subtends an angle β with the X axis, as in Eq. (31) and as shown in Figure 29.

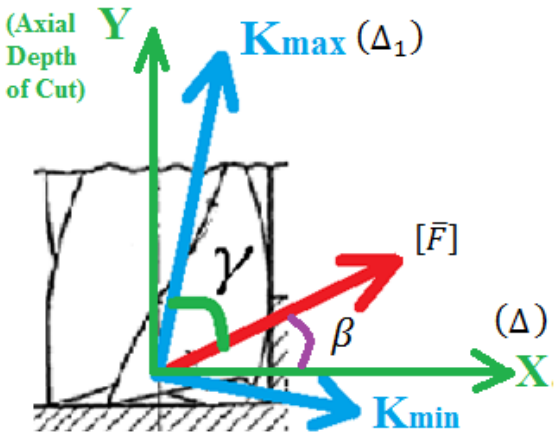

Figure 29. An equivalent 2D model of the robotic milling process.

Since the mass matrix $[M]$ and the stiffness matrix $[K]$ are symmetric and semi-positive definite, $[M]$ and $[K]$ can be diagonalized by the matrix $[V]$ via the similarity transformation as follows [9-11]:

$$[\Delta] = [V(\beta + \gamma)][\Delta_1] \tag{32}$$

$$[V]^T[M][V] = \begin{bmatrix} 1 & 0 \\ 0 & 1 \end{bmatrix} = [I] \tag{33}$$

$$[V]^T[K][V] = \begin{bmatrix} K_{max} & 0 \\ 0 & K_{min} \end{bmatrix} = [K_1] \tag{34}$$

Equation (32) describes the coordinate transformation between Δ and Δ_1, where Δ_1 represents the generalized or principal coordinates because they are uncoupled. The matrix $[V]$ changes with the angle $(\beta + \gamma)$ between Δ and Δ_1, $[K_1]$ is the stiffness matrix in the generalized coordinates Δ_1, while K_{max} and K_{min} are the maximum and minimum principal stiffnesses of the robot, respectively; γ is the angle between K_{max} and the average cutting force direction and it influences the system stability.

Equation (28) can be re-written as:

$$[M]\left[\ddot{\Delta}\right] + [K][\Delta] = [d\bar{F}] = \left[K_p\right][\Delta] \tag{35}$$

Following the standard modal analysis procedure, i.e. substituting Eq. (32) into Eq. (35), and multiplying the latter by the transposed matrix $[V]^T$, one obtains

$$[V]^T[M][V]\left[\ddot{\Delta}_1\right] + [V]^T[K][V][\Delta_1] = [V]^T\left[K_p\right][V][\Delta_1] \tag{36}$$

Substituting the similarity transformation given by Eqs. (33) and (34) into Eq. (36), the 2-dof dynamic system of equations expressed in principal coordinates are:

$$\left[\ddot{\Delta}_1\right] + [K_1][\Delta_1] = [V]^T\left[K_p\right][V][\Delta_1] \tag{37}$$

$$\left[\ddot{\Delta}_1\right] = \left[[V]^T\left[K_p\right][V] - [K_1]\right][\Delta_1] = [A][\Delta_1] \tag{38}$$

Substituting the principal stiffness matrix $[K_1]$ and the cutting stiffness matrix $\left[K_p\right]$, the matrix $[A]$ can be written as:

$$[A] = [V(\beta+\gamma)]^T\begin{bmatrix} K_{px}cos\beta & K_{py}cos\beta \\ K_{px}sin\beta & K_{py}sin\beta \end{bmatrix}[V(\beta+\gamma)] - \begin{bmatrix} K_{max} & 0 \\ 0 & K_{min} \end{bmatrix} \tag{39}$$

The stability of the system depends on the eigenvalues of $[A]$. If all the eigenvalues are negative real numbers, the system is stable; if the matrix has positive eigenvalues, the system is unstable.

5.2.3 Analysis of Chatter Stability

Different solutions of Eq. (39) are available based on various simplifications that have been used in mode coupling chatter analysis for various machining applications, including robotic milling [9-11, 39-41]. For a particular application and cutting condition, $[K_p]$ and β are constant. Therefore, γ is the critical variable for stability analysis.

In prior work [9-11, 39-41], the eigenvalues of $[A]$ were analyzed to determine the value of angle γ necessary to ensure a stable process. For a particular angle γ, the system is stable if the maximum eigenvalue λ_{max} of matrix $[A]$ is negative. In this thesis, the eigenvalues of $[A]$ are solved numerically. Therefore, the stability of the robotic milling system for a given angle γ can be determined through simulation. An example of the stability analysis for different γ is shown in Figure 30: (feed rate of $1\,mm/s$ used in Case 1, see Table 5).

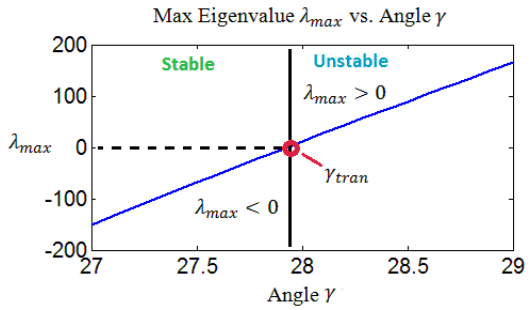

Figure 30. Stability analysis simulation.

As seen in Figure 30, the determination of the transition angle γ_{tran} separating the stable and unstable regions is critical for stability analysis. One approach to ensuring stability is to re-orient the workpiece based the value of γ_{tran}, as shown in Figure 31a. However, this approach is impractical in an industrial setting as it may not always be feasible to alter the workpiece orientation easily. In this thesis, a new approach is proposed. The new approach modifies γ by varying the direction of K_{max} (see Figure 31b). The following section discusses how this is accomplished by taking advantage of the Conservative Congruence Transformation (CCT)-based stiffness term.

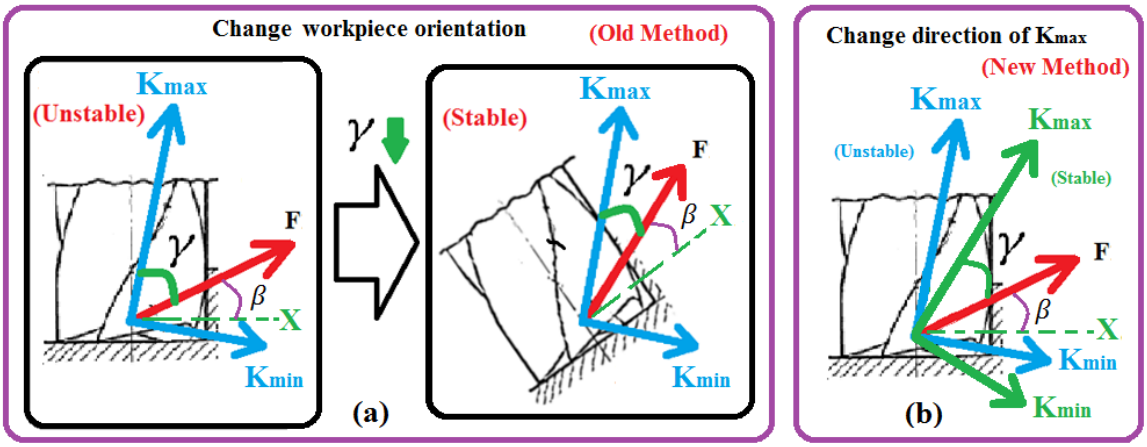

Figure 31. Comparison of old and new chatter avoidance methods.

5.2.4 Robot Stiffness Model

The sources of stiffness in a typical robotic manipulator include the compliances of its joints, actuators, its transmission elements, the geometric and material properties of the links, the base, and the active stiffness provided by its position control system. Similar to the approach in Section 3.4.1 and the work of other researchers [12, 13, 25, 26,

38, 56, 57], the stiffness model is based on the following simplified assumptions: 1) the primary source of stiffness is the joint stiffness in the axial direction of each joint, which is lumped into a constant joint stiffness, and 2) the robot's links are infinitely stiff.

For convenience in reading, the stiffness model is reproduced below, while detailed discussion of the model can be found in Section 3.2 and Section 3.4.1.

The commonly used stiffness model in robotic milling ignores the effect of external forces [12, 13, 25, 26, 38, 56, 57] and relates the robot stiffness in Cartesian space $[K]$ to its stiffness in the joint space $[K_\theta]$ via the congruence transformation, as follows:

$$[K] = [J(\theta)]^{-T}[K_\theta][J(\theta)]^{-1} = \left[[J(\theta)][K_\theta]^{-1}[J(\theta)]^T\right]^{-1} \tag{40}$$

where $[J(\theta)]$ is the kinematic Jacobian matrix of the robot, which depends on the joint angles $[\theta]$.

In this thesis, the effect of milling forces on the robot stiffness is accounted for via the CCT method proposed by Kao et al. [18-24] as follows:

$$[K] = [J(\theta)]^{-T}[K_\theta - K_c][J(\theta)]^{-1} = \left[[J(\theta)][K_\theta - K_c]^{-1}[J(\theta)]^T\right]^{-1} \tag{41}$$

where $[K_c]$ is the additional stiffness term, which takes into account the effect of milling forces $[F]$ acting on the end effector, and is given by:

$$[K_c] = \underbrace{\left[\frac{\partial[J(\theta)]^{-T}}{\partial\theta_1}F \quad \frac{\partial[J(\theta)]^{-T}}{\partial\theta_2}F \quad \cdots \quad \frac{\partial[J(\theta)]^{-T}}{\partial\theta_{n-1}}F \quad \frac{\partial[J(\theta)]^{-T}}{\partial\theta_n}F\right]}_{n\times n} \tag{42}$$

where $\left[\frac{\partial[J(\theta)]^{-T}}{\partial\theta_i}F\right]$ is an $n \times 1$ column vector, with $i = 1 \cdots n$, where n is the number of joints.

5.2.5 CCT-based Mode Coupling Chatter Avoidance

As discussed in Section 5.2.2, the stability of the robotic milling system depends on the eigenvalues of matrix $[A]$ given in Eq. (39). Following the eigenvalue analysis of matrix $[A]$, the angle γ between K_{max} and the milling force vector is analyzed for system stability evaluation [9-11, 39-41]. The conventional mode coupling chatter avoidance method minimizes the angle γ by changing the tool feed direction (or the average milling force direction) [9-11, 39-41], as shown in Figure 31.

In contrast to the conventional mode coupling chatter avoidance method, which limits the tool feed direction, the CCT-based method adjusts γ by altering the direction of K_{max}, as shown in Figure 31. With the help of the milling force dependent stiffness term $[K_c]$ in Eq. (42), suitable cutting parameters are selected to generate the appropriate $[K_c]$ that affects the eigenvector of the Cartesian stiffness $[K]$, thereby changing the direction of K_{max} to minimize γ. Mathematically, the method involves selecting suitable cutting conditions (i.e. milling force level) to manipulate the robotic arm stiffness so that the system is stable i.e. all eigenvalues of the matrix $[A]$ (Eq. 39) are negative and real, as shown in Figure 32.

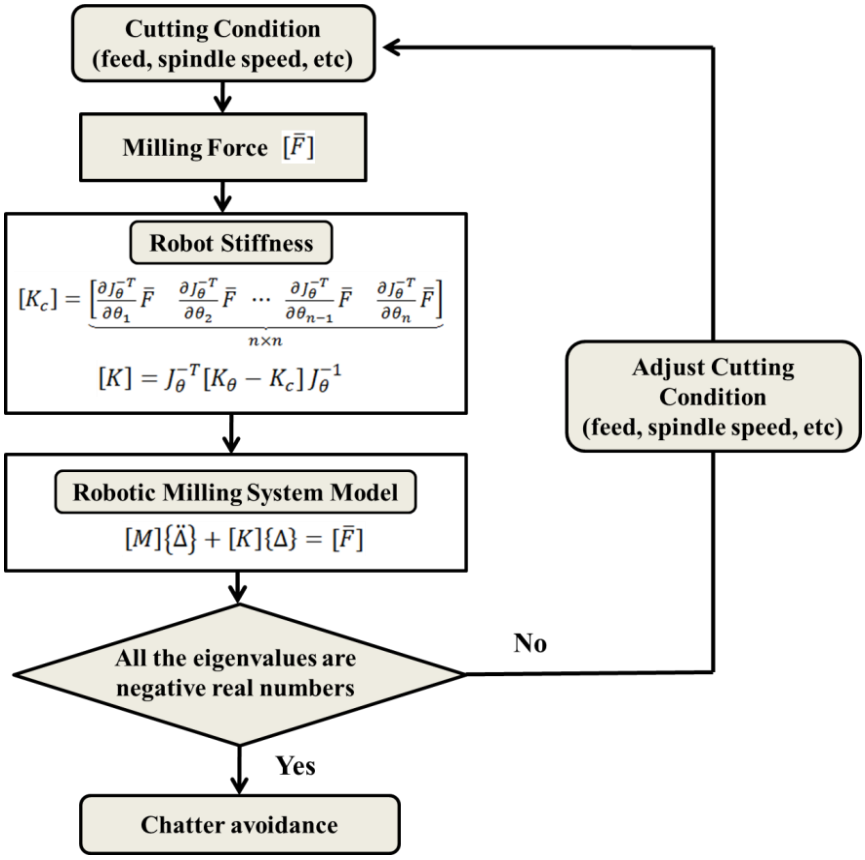

Figure 32. Flow chart of the chatter avoidance algorithm.

According to Eq. (42), the CCT-based stiffness term $[K_c]$ is determined by the milling force $[F]$ and the robot arm configuration (or joint angle combination). For a given external force, the effect of $[K_c]$ on the total Cartesian stiffness $[K]$ can be quite large depending on the type of robot and its arm configuration [19, 20]. Since the aim is to alter $[K_c]$ to manipulate the angle γ, a simulation of the change in angle γ due to modification of $[K_c]$ is shown in Table 4. For each robot arm configuration, the eigenvector of $[K]$ is solved twice (with and without $[K_c]$) to obtain the difference in angle γ ($\Delta\gamma_c$). For the 6-axis robot (Kuka KR210) utilized in the current work, there are more than 30 billion arm configurations if the joint angle resolution (smallest change in

joint angle) is set to 5^o, which corresponds to calculating the system eigenvectors at least 60 billion times. For simplicity, the joint angle resolution is varied from 11.4^o to 14.3^o in the workspace for the six joints, which corresponds to more than 100 million cases, as shown in Table 4. The force magnitude is set to 1000 N, which is less than half of the static payload of the robot arm. The results for a few typical cases are listed in Table 4. As can be seen in Table 4, the CCT-based stiffness term $[K_c]$ can alter γ by as much as 14.45^o. Note that, in reality, the variation in angle γ may be larger than 14.45^o for the same $[F]$ since the real joint angle resolution is much smaller than assumed in the computations performed here for illustration.

Table 4. Change in angle γ due to $[K_c]$. Representative results. (Unit: degree)

No.	θ_1 [-180, 180] ($\Delta\theta_1 = 14.3$)	θ_2 [-140, -5] ($\Delta\theta_2 = 11.4$)	θ_3 [-120, 155] ($\Delta\theta_3 = 11.4$)	θ_4 [-180, 180] ($\Delta\theta_4 = 14.3$)	θ_5 [-125, 125] ($\Delta\theta_5 = 11.4$)	θ_6 [-180, 180] ($\Delta\theta_6 = 14.3$)	$\Delta\gamma_c$
1	20.5352	-111.2451	40.4282	149.4507	-80.2141	-79.7324	**14.45**
2	20.5352	-111.2451	28.9690	178.0986	-103.1324	49.1831	**0.0286**
3	6.2113	-53.9493	-108.5408	6.2113	80.2141	63.5071	**0.0002**
4	149.4507	-122.7042	17.5099	49.1831	118.9690	-36.7606	**13.41**
5	-180	-122.7042	51.8873	49.1831	57.2958	6.2113	**3.9649**

Based on the above analysis, the experiments for joint stiffness identification discussed previously in Section 3.4.1 were limited to regions in the workspace where $[K_c]$ is negligible so that the joint stiffness calculation is simplified, as is common in the literature [25, 27, 56, 57]. On the other hand, the robotic milling experiments (presented later) were performed in the regions where $[K_c]$ is significant in order to verify the CCT-based mode coupling chatter avoidance method.

For simplicity, and without loss of generality, this thesis only adjusts the feed rate while maintaining the other cutting conditions including the spindle speed, and the radial and axial depths of cut constant.

5.3 Experiments and Results

5.3.1 Robotic Milling Setup

A robotic milling testbed was developed by attaching a motorized spindle to the end effector of a 6-axis robot (Kuka KR210). Peripheral end milling experiments were performed on an Aluminum 6061 workpiece. A 25.4 mm diameter tungsten carbide two flute square end mill with a 30 degree helix angle and 19 mm cutter length was used.

The cutting force components in the three orthogonal axes were measured by a three component quartz-based force dynamometer (Kistler 9257B) placed under the workpiece. The milling experiments consisted of linear tool paths with constant radial and axial depths of cut at different feed rates. A number of dry peripheral milling tests were conducted for the following two robot arm configurations shown in Figure 33 and

Figure 34: (1) cutter is perpendicular to the XY plane in the robot base coordinate system (Case 1), and (2) cutter is perpendicular to the XZ plane in the robot base coordinate system (Case 2).

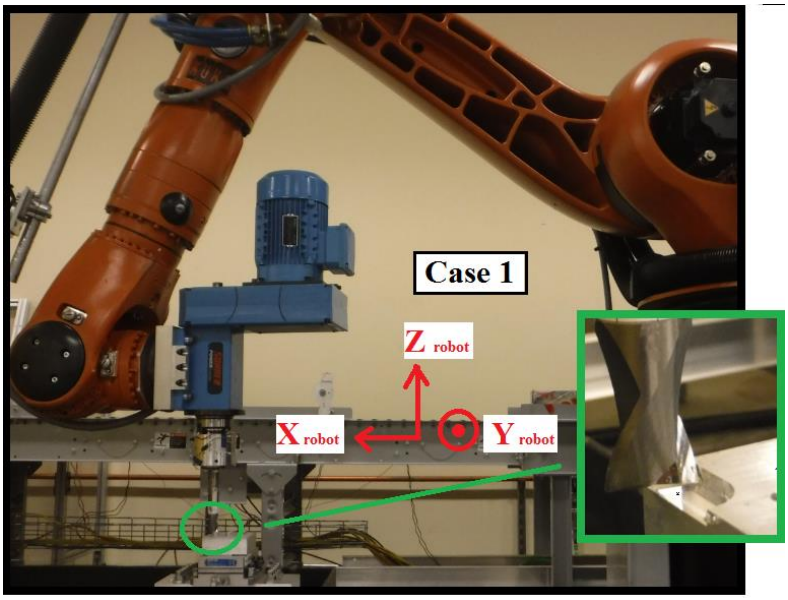

Figure 33. Cutter orientation in Case 1.

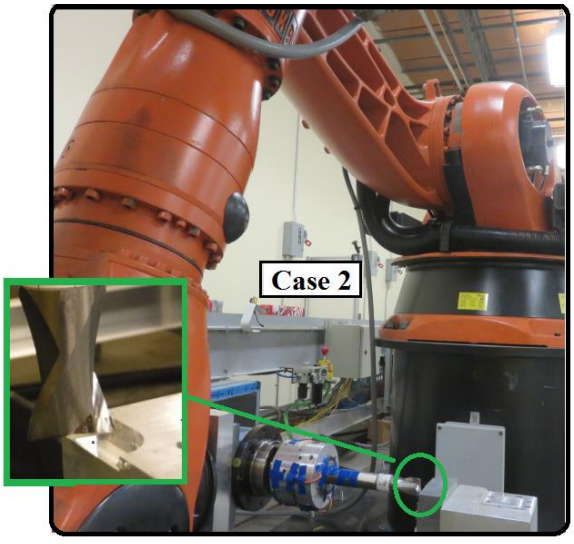

Figure 34. Cutter orientation in Case 2.

5.3.2 Robotic Milling Simulation and Experiment

The motorized spindle was operated at a constant spindle speed of 1000 rpm. The tool feed rate was limited by the spindle power and the payload of the robot used in this work (210 Kg for static loading, which includes the weight of the motorized spindle). When chatter occurs, the peak amplitude of the milling force can increase dramatically. Therefore, relatively conservative cutting conditions were used in the experiments, as shown in Table 5 and Table 6.

Table 5. Cutting conditions and joint angles for Case 1.

Case 1 (Feed : Y_{robot})	**Test No.**	**Feed rate (mm/s)**
Radial Depth of Cut: 15.24 mm		
Axial Depth of Cut: 5.08 mm	1	0.7
$\boldsymbol{\theta_1} = -96.42^o$	2	0.8
$\boldsymbol{\theta_2} = -29.26^o$	3	0.9
$\boldsymbol{\theta_3} = 99.08^o$	4	1.0
$\boldsymbol{\theta_4} = -9.95^o$	5	1.1
$\boldsymbol{\theta_5} = 83.23^o$	6	1.2
$\boldsymbol{\theta_6} = -160.5^o$	7	1.3

Table 6. Cutting conditions and joint angles for Case 2.

Case 2 (Feed : $-Z_{robot}$) Radial Depth of Cut: 12.7 mm Axial Depth of Cut: 4.25 mm $\boldsymbol{\theta_1} = -74.27^o$ $\boldsymbol{\theta_2} = -16.44^o$ $\boldsymbol{\theta_3} = 105.82^o$ $\boldsymbol{\theta_4} = -21.05^o$ $\boldsymbol{\theta_5} = 67.76^o$ $\boldsymbol{\theta_6} = -90.25^o$	**Test No.**	**Feed rate (mm/s)**
	8	0.9
	9	1.0
	10	1.1
	11	1.2
	12	1.3
	13	1.4
	14	1.5

The joint stiffness modeling was described in detail in Section 3.4.1. Using the joint stiffnesses identified in Table 2 of Section 3.4.1, the Cartesian stiffness $[K]$ at the end effector can be estimated using Eq. (41). The kinematic Jacobian matrix represents the effect of different robot arm configurations (or joint angle combinations), while the external force can be estimated from the cutting conditions (feed rate, radial and axial depth of cut). Finally, the angle γ can be calculated from the eigenvector of $[K]$, and the

stability of the robotic milling system can be evaluated from the eigenvalues of $[A]$ (Eq. 39). Using the analysis presented in Section 5.2.2, the angle γ was calculated at different feed rates for Cases 1 and 2, and the transition between stable and unstable conditions was identified (see Figure 35 and Figure 37).

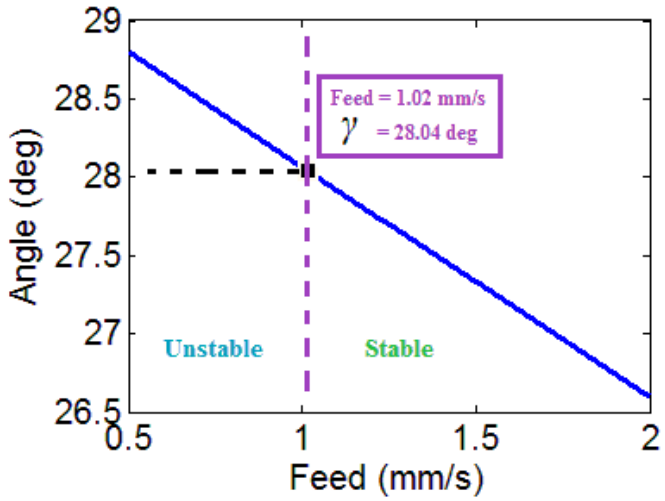

Figure 35. Simulation of angle γ as a function of feed rate (Case 1).

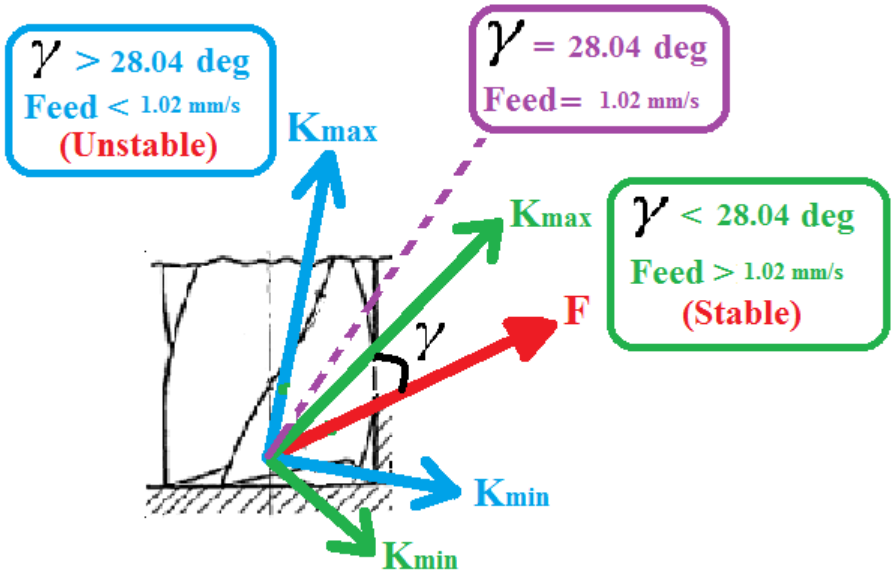

Figure 36. Plot of angle γ as a function of feed rate (Case 1).

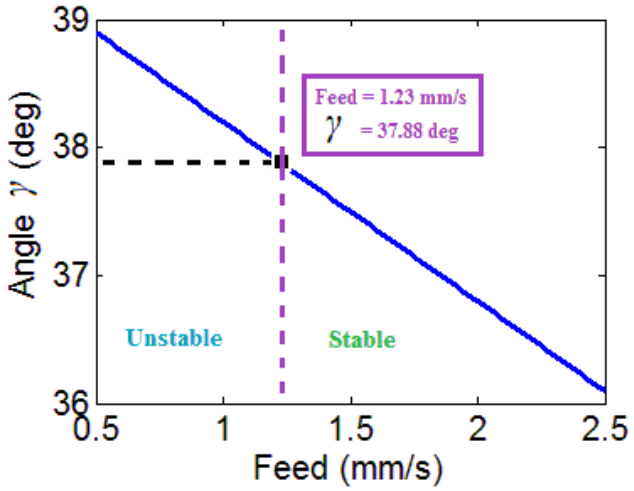

Figure 37. Simulation of γ as a function of feed rate (Case 2).

It is seen from Figure 35 that, for the specific robot arm configuration and cutting conditions considered, the angle γ decreases as the feed rate increases from 0.5 to 2 mm/s. It can also be seen that the feed rate of 1.02 mm/s (or angle $\gamma = 28.04^o$) represents the transition point between stability and instability (or chatter). As noted earlier, the conventional mode coupling chatter avoidance method in robotic milling alters the tool feed direction or the workpiece orientation to minimize γ whereas the CCT-based method modifies the direction of K_{max} to minimize γ. Similarly, the simulation result for Case 2 is shown in Figure 37. For this case, the transition point between stability and instability is predicted to occur at a feed rate of ~ 1.23 mm/s.

As shown in Table 5 and Table 6, a total of 14 dry peripheral milling tests were conducted using the robotic milling setup and the corresponding resultant cutting forces were determined from the measured force components. In order to verify the simulation results, experimental feed rates around the critical transition point (shown in Figure 35

and Figure 37) were selected. Representative results for Case 1 and Case 2 are selected for discussion below.

Figure 38a-c show the resultant forces for Case 1 at feed rates ranging from 0.7 to 1.3 mm/s, while Figure 39a-c show the resultant forces for Case 2 at feed rates ranging from 0.9 to 1.5 mm/s.

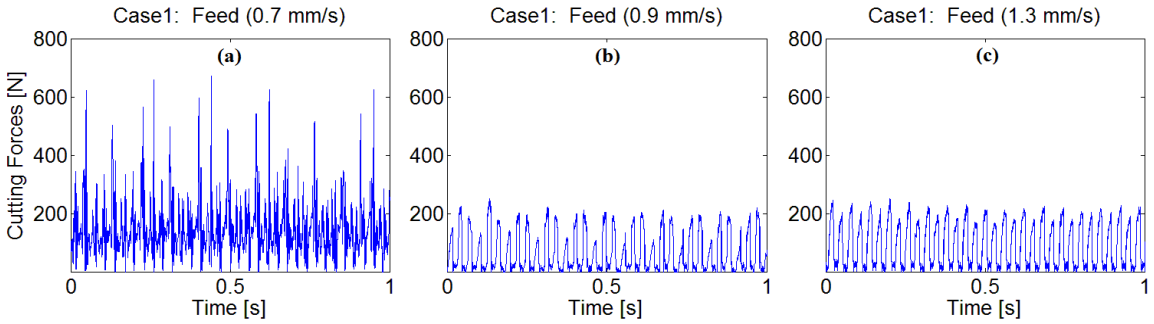

Figure 38. Case 1 (Test 1, Test 3, and Test 7).

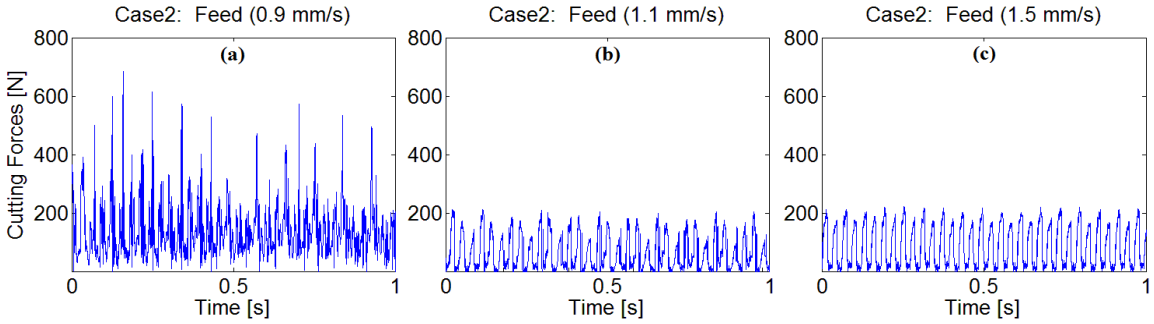

Figure 39. Case 2 (Test 8, Test 10, and Test 14).

It can be seen from Figure 38a (Test 1) and Figure 38b (Test 3) that a significant reduction in the resultant cutting force is observed at the critical feed rate. For Case 1, the

average resultant force was reduced from 147.6 N to 69.5 N, a 52.9% decrease. Similarly, a 46.9% decrease in the average resultant force was observed in Case 2, as seen in Figure 39a (Test 8) and Figure 39b (Test 10).

For the robot configurations used in Cases 1 and 2, there is transition from an unstable (chatter) cut to a more stable cut as the feed rate increases. This is consistent with the simulation results shown in Figure 35 and Figure 37, respectively. In the experiments, the transition occurs at a feed rate of ~ 0.9 mm/s for Case 1 and at a feed rate of ~ 1.1 mm/s for Case 2, both of which are slightly less than the simulated transition feed rates of 1.02 mm/s for Case 1 and 1.23 mm/s for Case 2. This discrepancy is attributed to the damping effect present in the actual process (but ignored in the simulation), which increases the stability of the system.

In order to further analyze the experimental results, Fast Fourier Transform (FFT) of the resultant forces in three representative tests for Case 1 are shown in Figure 40 (unstable), Figure 41 (transition), and Figure 42 (stable).

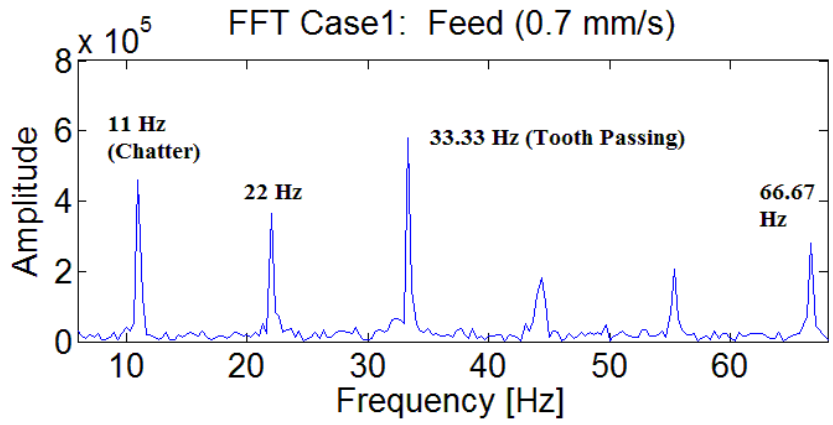

Figure 40. FFT for Case 1 at a feed rate of 0.7 mm/s (Test 1).

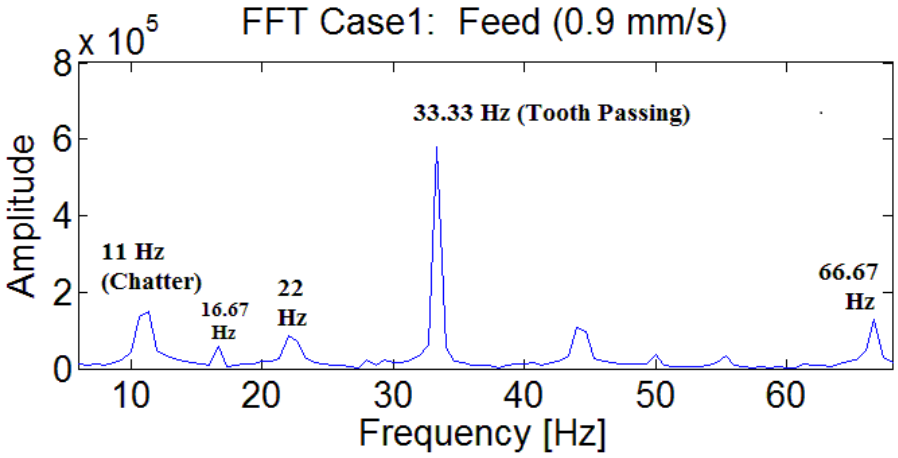

Figure 41. FFT for Case 1 at a feed rate of 0.9 mm/s (Test 3)

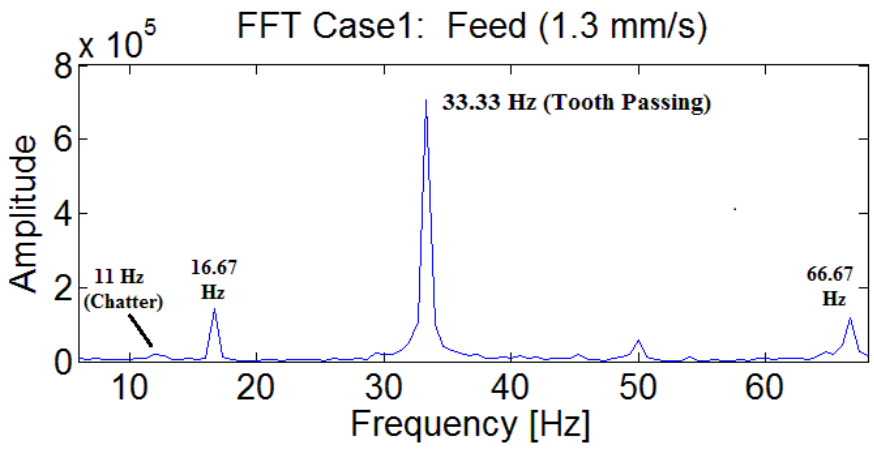

Figure 42. FFT for Case 1 at a feed rate of 1.3 mm/s (Test 7).

As seen in Figure 40 (Test 1), the mode coupling chatter vibration frequency is close to the natural frequency of the robot arm (~ 11Hz), which was identified through a modal hammer test. The vibration of the robot arm adversely impacts the undeformed chip thickness, which acts as an additional 11 Hz input that is fed back to the system. Therefore, the cutter tooth passing frequency (~33 Hz), the chatter frequency (~11 Hz), and their corresponding harmonics are visible in the Fast Fourier Transform (FFT). CNC milling experiments performed under the same cutting conditions confirm that "size effect" is not a significant factor in the robotic milling experiments.

As the feed rate increases to the transition point (Test #3, Figure 41), the dominant frequency becomes the tooth passing frequency (~33.33 Hz), and the chatter frequency is largely suppressed. When the feed rate increases to 1.3 mm/s, the system is further stabilized in Test 7. It can be seen from Figure 42 that the chatter frequency is almost negligible compared to the tooth passing frequency. However, there is still some residual vibration in Test 7, as seen in Figure 38c and Figure 42. This can be explained

by the magnitude of the robot arm stiffness (on the order of 10^5 – 10^6 N/m), which is much smaller than the stiffness of a typical CNC milling machine (on the order of 10^8 N/m).

Comparing Tests 1, 3 and 7 (see Figure 40, Figure 41, and Figure 42), it can be seen that the tooth passing frequency (~ 33.33 Hz) becomes more significant relative to the chatter frequency (~ 11 Hz). The system therefore becomes more stable as the feed rate increases from 0.7 to 1.3 mm/s, which is consistent with the trend shown in the simulation (see Figure 35).

5.3.3 Applicability to Different Arm Configurations

In order to further assess the applicability of the mode coupling chatter avoidance method for robotic milling presented in the previous section, the stability of robotic milling for different arm configurations was evaluated. It is well known from previous work [9-11, 39-41] that there are two important factors in mode coupling chatter evaluation. One is the angle γ between K_{max} and the average cutting force direction, while the other is the difference between the two principal stiffnesses of the robot arm ($\Delta K = K_{max} - K_{min}$). Mode coupling chatter is more likely to happen when ΔK is small, which, as shown elsewhere [9-11, 39-41], can be derived from the eigenvalue analysis of matrix [A] (see Eq. 39). A rule of thumb in the machine tool industry is that the stiffness in the two orthogonal directions should differ by at least 10% to avoid mode coupling chatter.

Similar to the work discussed in [56, 57], only the translations of the robot end effector in the XZ plane were analyzed for simplicity. As shown in Figure 43 to Figure 45, the joint coordinates, indicated on the robot arm, rotate about the Z axis for each joint. Because the 2nd, 3rd, and 5th revolute joins are the three most influential joints as far as the translations of the robot end effector in the XZ plane are concerned, the rest of the joints are set to 0 in the simulations to simplify the analysis and to more easily visualize the arm configurations.

Assuming the same workpiece orientation and cutting conditions (K_p, γ, α), mode coupling chatter is more likely to occur when ΔK is small. In order to assess the process stability in robotic milling for different arm configurations, the magnitude of ΔK in the XZ plane was calculated.

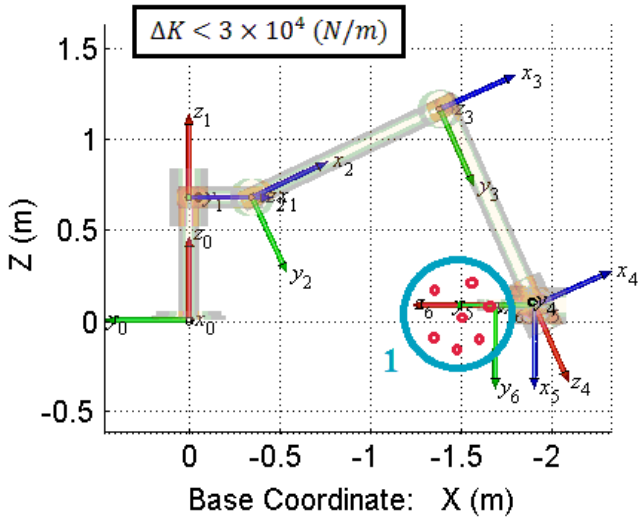

Figure 43. Simulation for ΔK in work zone 1 (Blue circle).

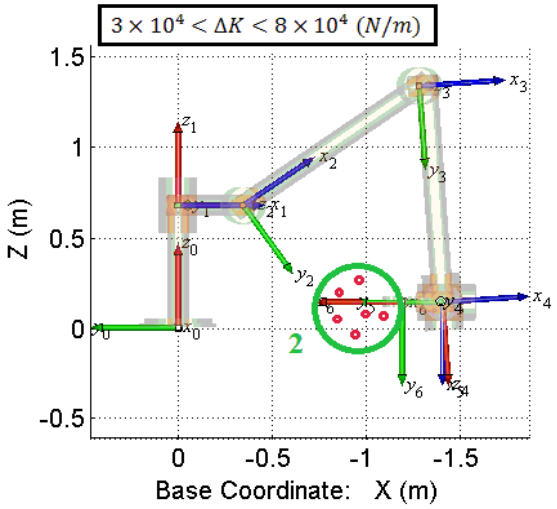

Figure 44. Simulation for ΔK in work zone 2 (Green circle).

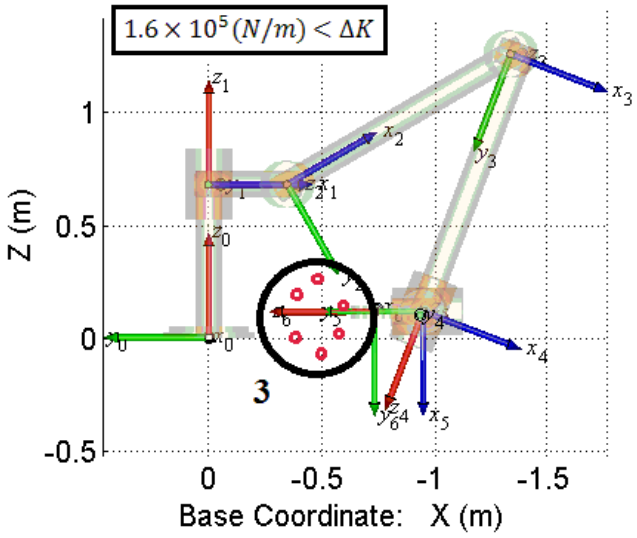

Figure 45. Simulation for ΔK in work zone 3 (Black circle).

As shown in Figure 43 to Figure 45, ΔK decreases from work zone #3 to #1 as the end effector moves farther away from the robot base. As the magnitude of ΔK decreases from work zone #3 to #1, $[K_C]$ plays an increasingly important role in CCT-based robotic

arm stiffness modeling, which is consistent with previous findings [56, 57]. Therefore, the CCT-based method is more effective in the weak stiffness work zones, where mode coupling chatter is more likely to occur.

5.4 Summary

In this chapter, the CCT-based stiffness term is integrated into the robotic milling chatter model to take into account the effect of milling force on the robot arm stiffness. In prior efforts, the angle γ between K_{max} and the milling force vector could only be altered by changing the workpiece orientation or robotic arm configuration. By using the CCT-based external force related stiffness term, another approach to chatter avoidance is possible. This involves adjusting the angle γ by changing the stiffness vector K_{max} of the robot arm. Since the stiffness of the robot arm can be adjusted by the external cutting force using the CCT-based stiffness model, the effect of cutting condition on the angle γ can be simulated to determine the stability of the robotic milling system.

Based on this approach, a new mode coupling chatter avoidance method for robotic milling using the CCT-based stiffness model was proposed in this chapter. With the help of the milling force dependent stiffness term $[K_c]$ in Eq. (42), it was shown that suitable cutting parameters could be selected to generate the appropriate $[K_c]$ to affect the eigenvector of the Cartesian stiffness $[K]$, thereby changing the direction of K_{max} to minimize γ.

Robotic milling experiments conducted to validate the approach demonstrated significant reductions ($> 45\%$) in the average resultant force when the proposed chatter avoidance strategy was implemented. Simulations demonstrated that the proposed CCT-

based method was more effective in the weak stiffness work zones, where mode coupling chatter is more likely to occur. Distinct from the previous methods reported in the literature, the new method presented in this chapter does not require changing the tool feed direction or the workpiece orientation, which preserves the versatility of robotic milling and thus making it more practical for industrial application.

CHAPTER 6. CHATTER SUPPRESSION THROUGH CLOSED LOOP CONTROL

6.1 Introduction

In this chapter, a method for real time chatter detection and suppression is proposed to account for the inherent modeling and process uncertainties in the robotic milling process for more complex tool paths. The uncertainty or inaccuracy in the force model predictions increases with more complicated robotic milling scenarios, such as due to changes in the feed/axial depth of cut or changes in the robot arm configuration along a curvilinear tool path. In this case, unlike the work presented in Chapter 5 and in prior works [8-11], the assumptions of a constant cutting condition and constant arm configuration are not applicable for the entire tool path.

To consider a tool path with significant variation in the cutting condition(s) and robot arm configuration, the tool path must be partitioned into small sections within which process stability characteristics can be assumed to be constant. A methodology to determine the appropriate section lengths within the entire tool path is proposed in this chapter. The stability characteristics for each section of the tool path can then be analyzed using the CCT-based mode coupling chatter model presented in Chapter 5. The proposed partitioning method 1) calculates the initial cutting parameters along the tool path, 2) provides a guideline to adjust the cutting parameters in case chatter occurs due to uncertainty/inaccuracy in the initial cutting parameter selection, and 3) predicts the

stability characteristics along the entire tool path, which is helpful for tool path planning at the beginning.

Using the real-time wireless PVDF sensor system discussed in Chapter 4, the cutting force-induced dynamic strains can be acquired wirelessly. Based on estimation of the chatter frequency from the robot arm model discussed in Chapter 5, the onset of mode coupling chatter in robotic milling can be detected efficiently. Once the onset of chatter is detected, the cutting conditions can be adjusted to suppress chatter using the guideline derived from the CCT-based chatter model. In the following sections of this chapter, the overall methodology and approach are described, followed by experimental validation, discussion of results, and conclusions.

6.2 Methodology

6.2.1 Section Length and Initial Cutting Condition Determination

The initial machining parameters (in this case the feed rate) must be calculated along the tool path before they are altered via closed loop control. The entire tool path is divided into small sections, whose length is defined as the section length L_S (see Figure 46). In order to determine the initial feed rate during robotic milling, the system stability is calculated at the mid-point of each individual section along the entire tool path.

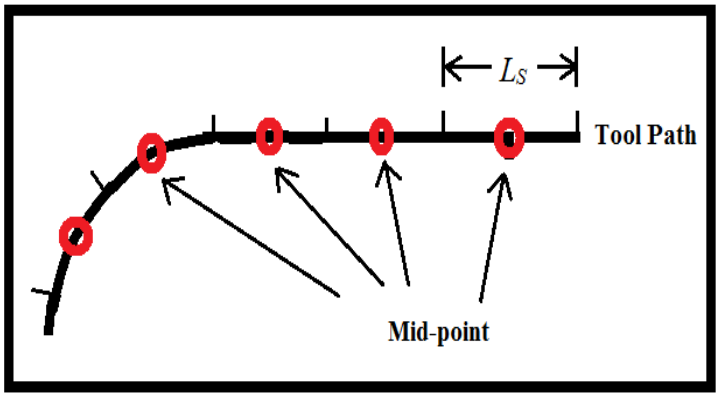

Figure 46. Partionting of the tool path into sections.

L_S must be established iteratively to ensure that the stability characteristics (see Figure 47 and Figure 48) calculated at the midpoint of each section adequately describe the stability characteristics along the entire length of that section. Note that the initial machining parameter (in this case, feed rate) is a by-product of calculating L_S. First, an initial guess for L_S is made. Then the tool path is partitioned into sections using L_S. The stability characteristics within each section are assumed to be constant so that the CCT-based chatter methodology can be applied at the midpoint to obtain the corresponding stability characteristics for the entire section. Similar to the approach in Chapter 5, the relationship between the machining parameter being adjusted (in this case the feed rate) and the angle γ can be obtained at the midpoint of each section.

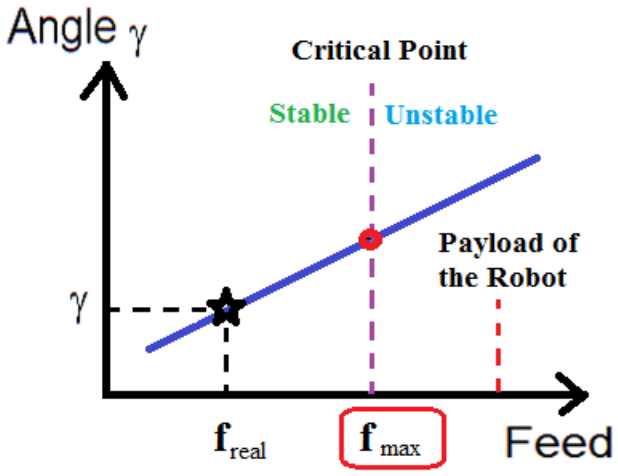

Figure 47. Case 1 with positive slope.

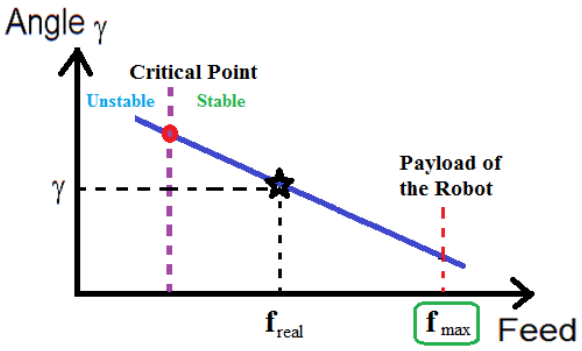

Figure 48. Case 2 with negative slope.

Note that in the stability characteristic shown in Figure 47 (Case 1), the maximum allowable feed rate is located at the critical transition point that separates stable and unstable regions. However, in the stability characteristic for Case 2 shown in Figure 48, the maximum feed rate is limited by the robot's payload. Thus, for each midpoint, the maximum allowable feed rate is defined as the maximum feed rate that will not induce force overload or chatter. Therefore, the actual feed rate for each section L_S can be calculated from the maximum feed rate and a safety factor, as follows:

$$\boldsymbol{Safety\ Factor} = \frac{f_{max}}{f_{real}} \rightarrow \boldsymbol{f_{real}} = \frac{f_{max}}{\boldsymbol{Safety\ Factor}} \tag{43}$$

where f_{max} is the theoretical maximum feed rate that does not overload the robot or does not cause chatter, while f_{real} is the feed rate chosen based on a predetermined safety factor.

From the plots shown in Figure 47 and Figure 48, the angle γ corresponding to a particular f_{real} can be calculated. The next step is to calculate the maximum allowable change in angle γ within each section, denoted as $\Delta\gamma_{max}$. $\Delta\gamma_{max}$ is the difference between the angle γ corresponding to f_{real} and the angle γ at the limit of stability or at the payload limit of the robot. For example, $\Delta\gamma_{max}$ can be calculated as the difference in γ between f_{max} and f_{real}, as shown in Figure 49, where f_{max} is the critical value of feed rate that separates the stable region from unstable cutting.

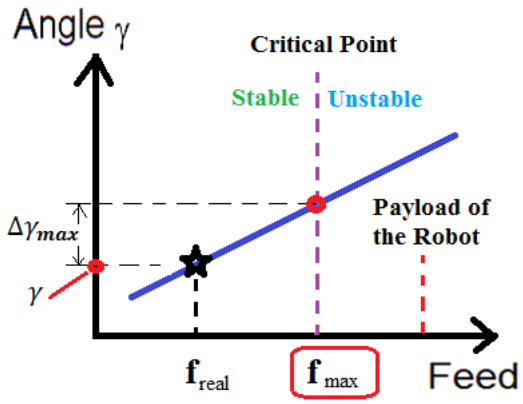

Figure 49. $\Delta\gamma_{max}$ for Case 1.

However, in the case shown in Figure 50, the angle γ corresponding to f_{real} is located between the critical stability point and the payload limit of the robot. Thus, the system becomes unstable as the feed rate is decreased past the critical point, while increasing the feed rate can cause the robot payload to be exceeded. Thus, for the

particular stability relationship illustrated in Figure 50, $\Delta\gamma_{max}$ is the minimum of $\Delta\gamma_{max1}$ and $\Delta\gamma_{max2}$.

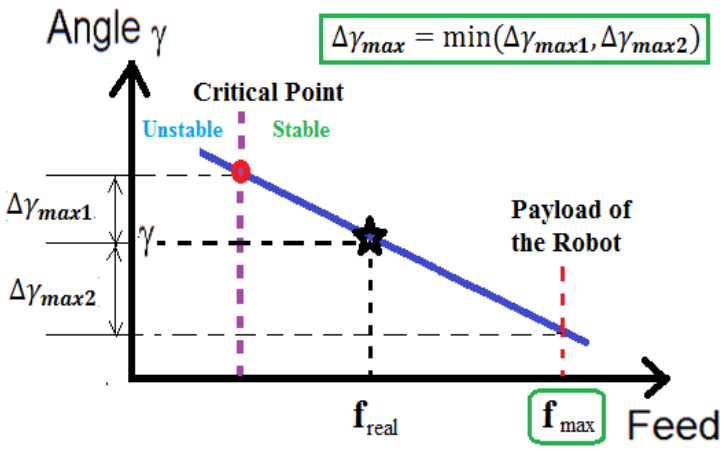

Figure 50. $\Delta\gamma_{max}$ for Case 2.

Once $\Delta\gamma_{max}$ has been determined for each section, the change in γ between the endpoints of each section, denoted as $\Delta\gamma$, is calculated by linear interpolation between the section midpoints, as shown in Figure 51. Then, $\Delta\gamma$ is compared to the maximum allowable change $\Delta\gamma_{max}$ for that particular section. If the magnitude of $\Delta\gamma$ is smaller than the magnitude of $\Delta\gamma_{max}$, the variation in γ along the entire section is within the bounds of stability/overload and the current section length is acceptable. In this case, the corresponding L_S is considered acceptable for that particular section. Otherwise, L_S is decreased, and the new reduced L_S is used in the next iteration to get a smaller $\Delta\gamma$. The algorithm proceeds until all the section lengths along the tool path satisfy the criteria ($\Delta\gamma < \Delta\gamma_{max}$).

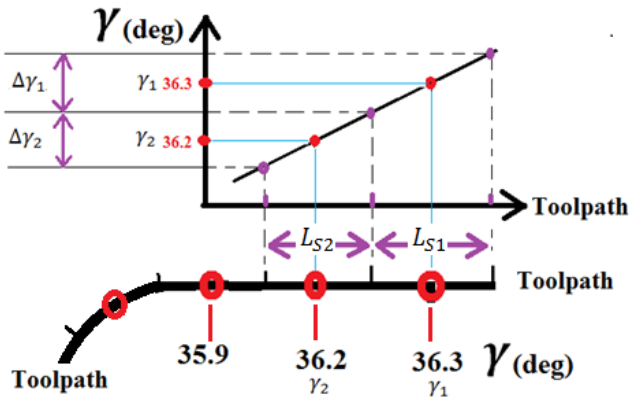

Figure 51. Calculating Δγ using linear approximation.

The complete procedure can be summarized as follows and in Figure 52:

Step 1: Pick an initial guess L_S and partition the tool path accordingly. Then perform chatter stability analysis at the midpoint of each section.

Step 2: Select the feed rate for each section according to the maximum allowable feed rate subject to a pre-determined safety factor. The corresponding angle γ is calculated from the selected feed rate.

Step 3: Calculate $\Delta\gamma_{max}$ for each section using the angle γ from Step 2 and the angle γ corresponding to the system's stability/payload limits.

Step 4: Calculate $\Delta\gamma$ along each section using linear approximation. If $\Delta\gamma$ is larger than $\Delta\gamma_{max}$, the corresponding L_S must be decreased and Steps 1-4 must be repeated with the new L_S. If $\Delta\gamma$ is less than $\Delta\gamma_{max}$, the corresponding feed rate is selected for that section.

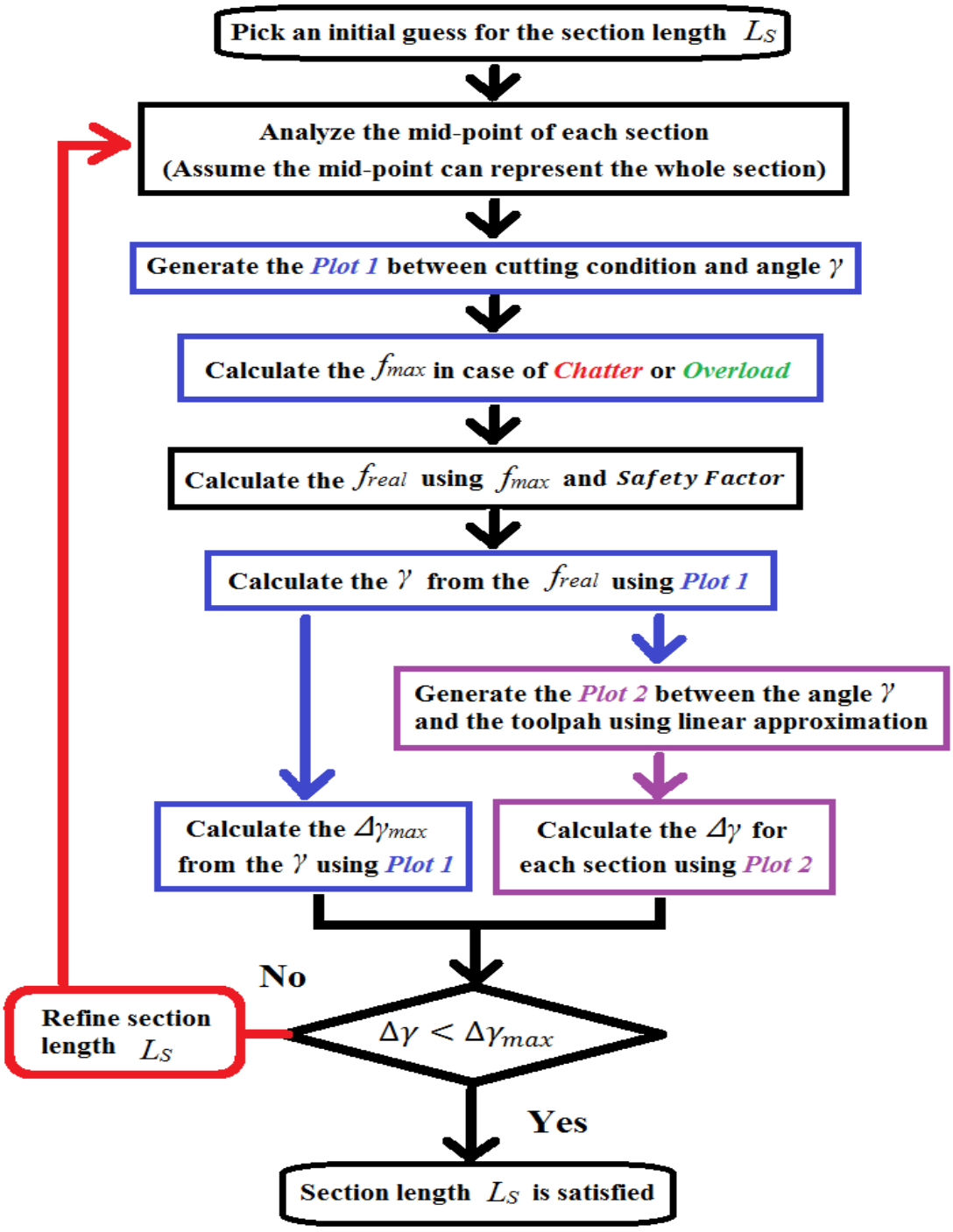

Figure 52. Algorithm for section length determination.

(Plot 1: Fig 49&50; Plot 2: Fig 51).

6.2.2 On Line Chatter Detection and Suppression

Once the section lengths and initial feed rates have been determined along the tool path, robotic milling can start as an open-loop process. In theory, the robotic milling process should be stable in all the sections along the tool path for the feed rates determined using the algorithm just described. However, uncertainties or inaccuracies in the CCT-based chatter model calculation can increase with tool path length or due to variations in the cutting conditions and material properties. For example, the mass and stiffness matrix may change significantly as the pose of the robot or the feed direction is changed. As a consequence, chatter may occur in some sections of the tool path. The use of conservative cutting conditions (very large safety factor) is a common approach to addressing these uncertainties in open-loop robotic milling [9-11]. However, this can compromise productivity of the operation. Therefore, to compensate for such uncertainties/inaccuracies and to increase productivity, a closed-loop feedback control algorithm is proposed in this chapter to detect and suppress chatter in real time.

Using the methodology described in the previous section, the appropriate section length and the corresponding feed rate can be calculated along the entire tool path. If chatter occurs in a particular section due to process uncertainty, an algorithm is required to: 1) detect chatter in its incipient stages, and 2) adjust cutting conditions to suppress the chatter. In order to accomplish these tasks, a chatter detection algorithm and the methodology for adjusting the cutting conditions to suppress chatter were developed.

To detect chatter, Discrete Wavelet Transform (DWT) was applied to the time series cutting force-induced dynamic strain signal, which was measured using the

wireless PVDF sensor system described in Chapter 4. Unlike frequency based methods, such as the FFT, the DWT achieves simultaneous time-frequency resolution and is thus suitable for early chatter detection. However, to determine the frequency decomposition band level of interest, the chatter frequency must be known beforehand. In the case of mode coupling chatter, the chatter frequency is known to be close to the robot's natural frequency. Therefore, the frequency decomposition band of interest can be pre-determined so that the mode coupling chatter frequency lies within the wavelet band of interest.

To determine the chatter fault threshold applied to the wavelet signal, a standard univariate control chart was implemented for chatter detection. Chatter is detected when the wavelet signal exceeds the predetermined control limits. The upper control limit (UCL) and lower control limit (LCL) of the control chart can be set as:

$$UCL = L_c\sigma, \;\; LCL = -L_c\sigma \tag{44}$$

where σ is the standard deviation estimated from the simulated dynamic effect model presented in Chapter 3, which is assumed to be representative of stable cutting. L_c is a real, positive number determined from an acceptable false alarm rate α_f (i.e., the probability of issuing an alarm when chatter does not occur). Similar to [67, 68], the cutting signal is assumed to follow a Gaussian distribution, and L_c can thus be determined as

$$Z_c(z \leq L_c) = 1 - \frac{\alpha_f}{2} \tag{45}$$

where $Z_c(z)$ is for the cumulative distribution function of a standard Gaussian distribution. The threshold is set as the control limits, which depend on the requirement of

false alarm rate. For the following experiments, the control limits in the control chart are set as $L_c = 4$, which corresponds to a false alarm rate (α_f) of 6E-5 according to the univariate control chart theory.

Once chatter is detected, the feed rate is adjusted. To adjust the feed rate in the correct direction (i.e. increase or decrease), the stability characteristics (shown in Figure 47 and Figure 48) for that particular section are used. The change in feed rate is proportional to the difference between the threshold and the maximum amplitude of the wavelet signal. The feed rate is adjusted until the wavelet signal is below the threshold.

6.3 Experiments and Results

6.3.1 Robotic Milling Setup

Peripheral end milling experiments on an aluminum 6061 workpiece were performed on the robotic milling testbed discussed previously in the thesis. The closed-loop control for robotic milling experiment is same as the one in Section 4.3.1. The total delay time for the closed loop system employed in this work is around 0.3 s. A 25.4 mm diameter tungsten carbide two flute square end mill with a 30 degree helix angle and 19 mm cutter length was used.

The cutting force components in the three orthogonal axes were measured using a three component quartz-based force dynamometer (Kistler 9257B) placed under the workpiece. The milling experiments consisted of a tool path which starts in the X direction but transitions to the Y direction (see Figure 53).

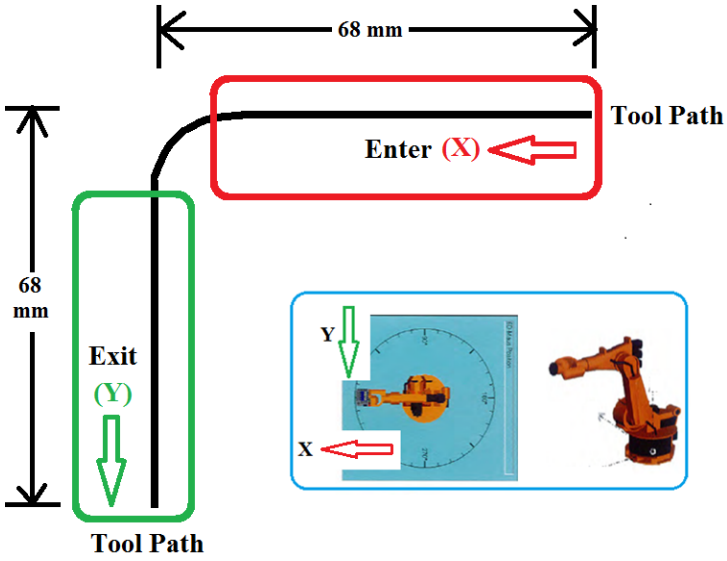

Figure 53. Tool path that first starts in the X direction and then moves in the Y direction.

Note that the stability characteristics in the X and Y directions differ significantly from each other, as shown in Figure 54. For the tool path in the X direction, the stability characteristic is defined by Case 1 (see Figure 47), where the maximum allowable feed rate f_{max} is limited by the critical transition point between stable and unstable milling. The stability characteristic for the tool path in the Y direction is similar to Case 2 (see Figure 48), where the maximum feed rate is limited by the robot's payload. Therefore, the robotic milling process along the tool path in the Y direction is expected to be more stable than along the tool path in the X direction for the same cutting conditions.

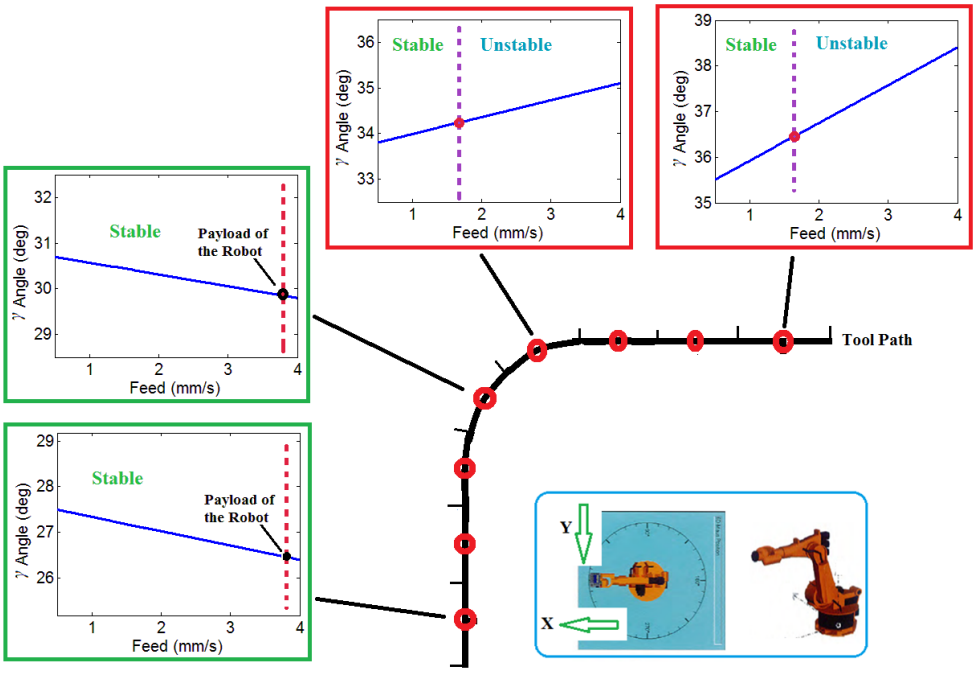

Figure 54. Stability along the tool path.

6.3.2 Results and Discussion

Note that the 210 Kg payload for the KUKA (KR210) robot arm is only for static loading, which includes the weight of the motorized spindle. In the robotic milling process, certain joints of the robotic arm can overload even when the resultant cutting force is less than the static payload. In addition, when chatter occurs, the peak amplitude of the milling force can increase dramatically. Therefore, in order to ensure the safety of the robot arm, the maximum allowable resultant cutting force was limited to 300 N.

As mentioned previously in Section 6.2.2 and as shown in Figure 55 for Tests #1(X) and #2(Y) (see Table 7), selecting a small safety factor (e.g. 1.05) yields a higher feed rate, which causes the onset of chatter very early in the cutting process. On the other

hand, selecting a large safety factor (1.4) results in the use of a smaller feed rate, which decreases the productivity of the milling operation. Therefore, a safety factor of 1.1 was used in the following experiments.

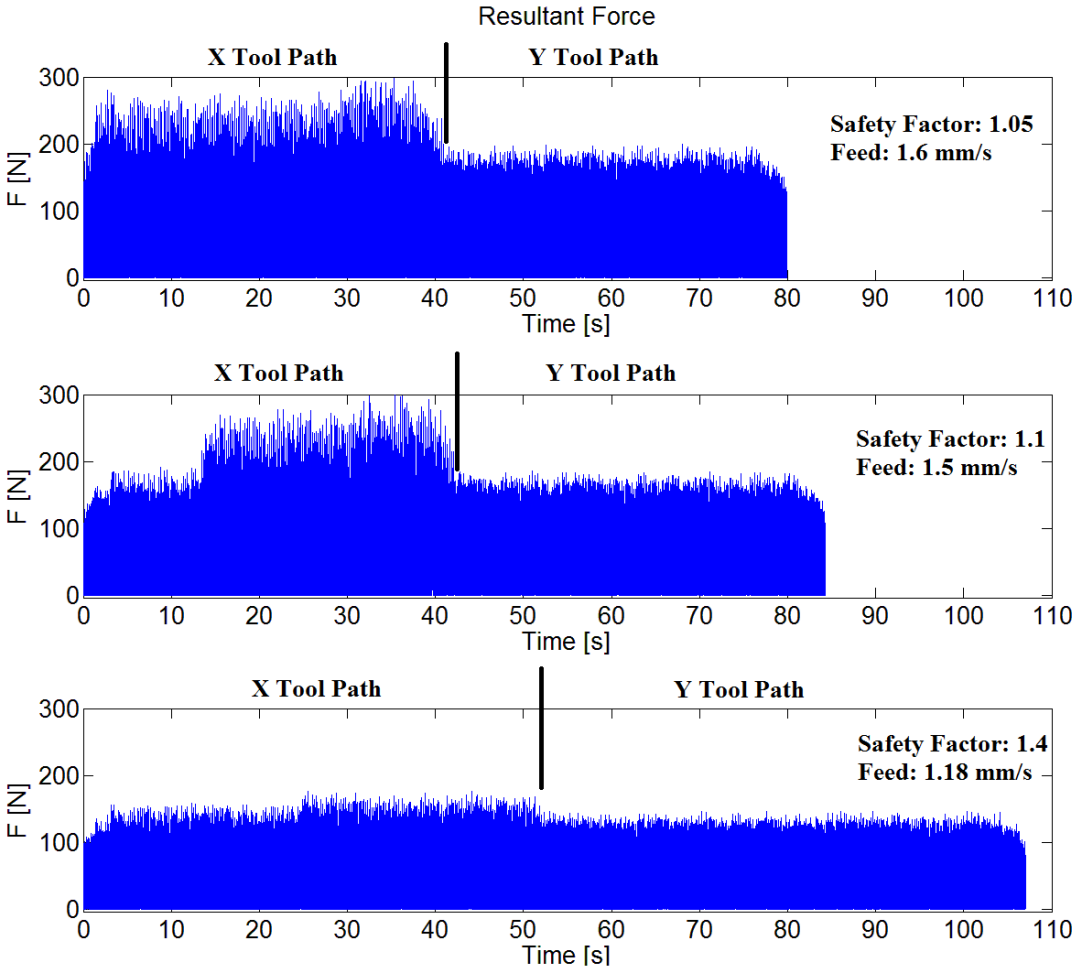

Figure 55. Effect of different safety factors on the resultant force in Tests 1 and 2.

The cutting conditions used in the open loop and feedback experiments are listed in Table 7. The radial depth of cut was 12.7 mm for all the experiments.

Table 7. Cutting conditions for the open loop and feedback experiments.

Test No.	Feed (mm/s)	Axial Depth of Cut (mm)	Direction	Control
1	1.5	3	X	Open loop
2	1.5	3	Y	
3	1.5	3	X	Feedback
4	1.5	3	Y	
5	0.8 →1.6	3	X	Open loop
6	1.6 → 3.2	3	Y	
7	0.8 →1.6	3	X	Feedback
8	1.6 → 3.2	3	Y	
9	1.6	1.5 → 3	X	Open loop
10	1.6	3 → 5.5	Y	
11	1.6	1.5 → 3	X	Feedback
12	1.6	3 → 5.5	Y	

For Tests #1 and #2 in Table 7, constant cutting conditions (feed and axial depth of cut) were applied to the X and Y tool paths to highlight the differences in their stability characteristics. Therefore, the minimum f_{real} among all the section lengths was selected as the initial feed rate in Tests #1 and #2 so that the open loop milling process would be stable in both the X and Y directions if there are no process uncertainties, i.e., the initial feed rate was calculated using accurate system parameters (robot stiffness matrix, cutting force model, etc.).

However, due to the process uncertainty in robotic milling, chatter might still occur in certain sections, as shown in Figure 56. Closed loop feedback control was then applied to the same cutting conditions to update the initial feed rate in real time to

suppress chatter in certain sections, as indicated Table 7 (see Tests #3 and #4) and Figure 57.

In Tests #5 and #6 in Table 7, the feed rate was doubled in the X and Y directions to highlight the effect of changing the feed rate. Similarly, the axial depth of cut was suddenly increased via the creation of steps in the workpieces used in Tesst #9 and #10. Note that Tests #7 and #8, and Tests #11 and #12 are the closed loop control experiments corresponding to the open loop robotic milling cutting condition used in Tests #5 and #6, and in Tests #9 and #10, respectively.

Tests in the X direction (#5 and #9) were performed to evaluate the capability of the chatter detection algorithm when chatter is actually occurring due to a sudden increase in feed rate or the axial depth of cut. Therefore, the 1.6mm/s feed rate utilized in Tests #5 and #9 were set to be larger than the feed rate used in Test #1 (1.5 mm/s) for the same axial depth of cut (3 mm).

The tests in the Y direction (#6 and #10) were performed to investigate if the proposed algorithm triggers a false alarm due to the sudden increase in cutting force owing to the variations in feed rate or the axial depth of cut. Therefore, the initial feed rate in Tests #6 and #10 were such that the abrupt increase in feed rate or axial depth of cut will not cause chatter. The initial feed rates were calculated based on the maximum resultant cutting force requirement to ensure safety of the robot (300 N).

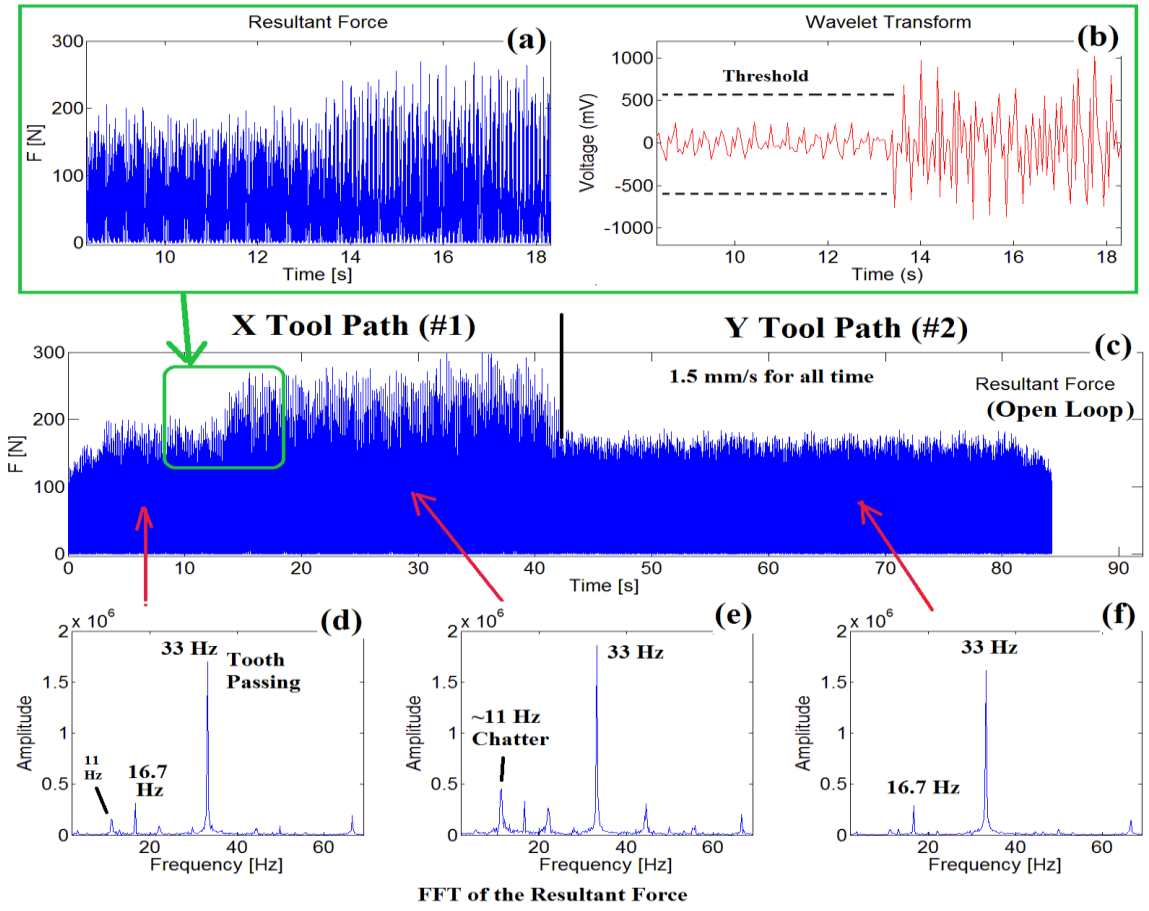

Figure 56. Open loop robotic milling in the X and Y directions (Tests #1 and #2).

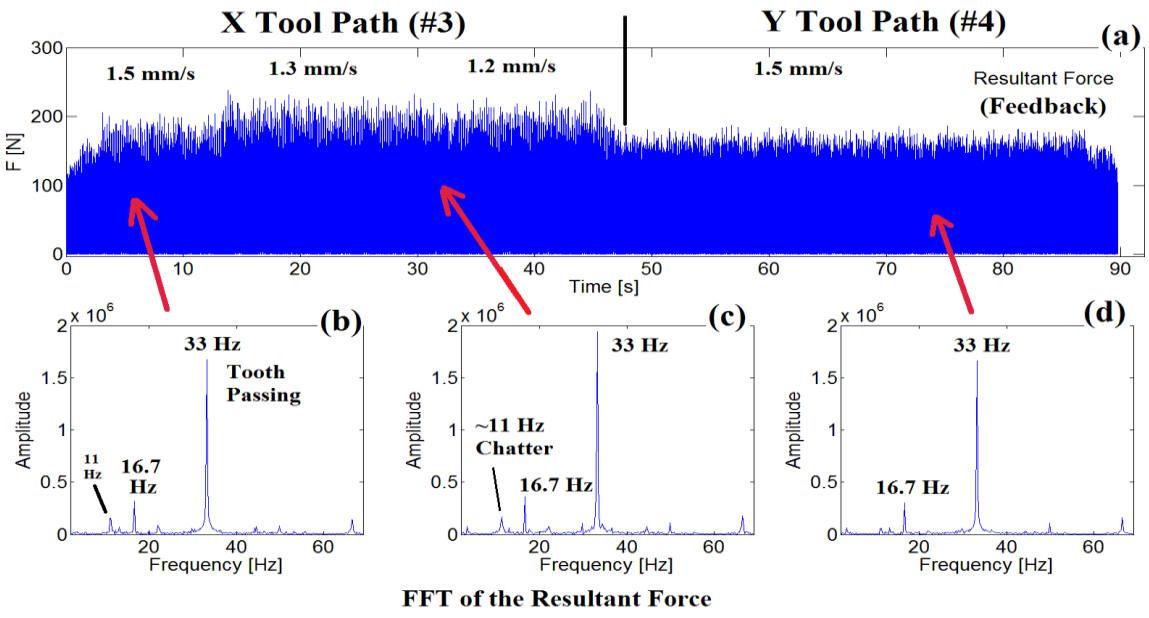

Figure 57. Closed loop robotic milling in the X and Y directions (Tests #3 and #4).

The first two tests (#1 and #2) used the same cutting conditions (feed, axial/radial depth of cut) but in the X and Y directions. As shown in Figure 56c, the experimental resultant force highlights the difference in stability when the robot arm moves in the two directions. The milling process is found to be more stable in the Y direction compared to the cutting in the X direction. As shown in Figure 56d, there is a small 11 Hz frequency peak in the FFT of the resultant force generated during cutting in the X direction, which is negligible in the FFT of the resultant force corresponding to motion in the Y direction (see Figure 56f). As explained in Chapter 3, the ~11 Hz peak is close to the natural frequency of the robot arm identified through a modal impact hammer test (11.3 Hz). The process uncertainty in the X tool path finally causes chatter to occur around 13 seconds into the cut, as shown in Figure 56(a-c). As shown in Figure 56e, when chatter occurs, the 11 Hz component in the FFT increases dramatically, which is explained by the mode coupling chatter model in Chapter 5.

As shown in Figure 56a and Figure 56b, the wavelet transform of the cutting force-induced dynamic strain signal obtained from the wireless PVDF sensor system can detect the onset of chatter efficiently since the chatter frequency lies within the 9^{th} DWT decomposition level, which can be pre-determined using the robotic model presented in Section 3.2. Chatter detection takes around 5 ms in these experiments.

Once chatter is detected, the feed rate is adjusted using the stability characteristic (shown in Figure 47 and Figure 48) appropriate for that particular section of the tool path. The feed rate is adjusted until the wavelet signal is below the threshold, as discussed in Section 6.2.2. As shown in Figure 57a (test #3), the initial feed rate was reduced to 1.2~1.5 mm/s after the detection of chatter at around 13 seconds. The chatter was then

suppressed as seen in Figure 57c. The result shown in Figure 57c is very similar to that shown in Figure 57b, which is before chatter occurs.

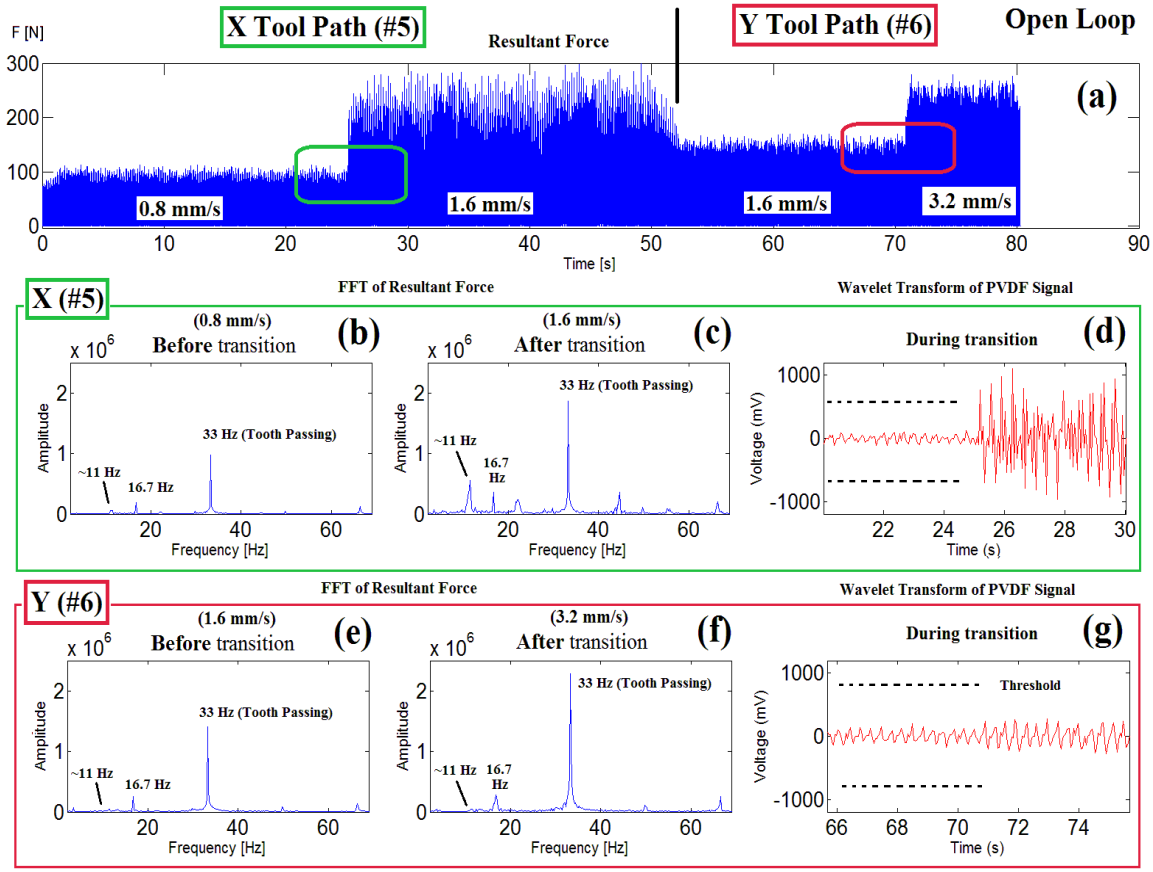

Figure 58. Open loop robotic milling in the X and Y directions (Tests #5 and #6).

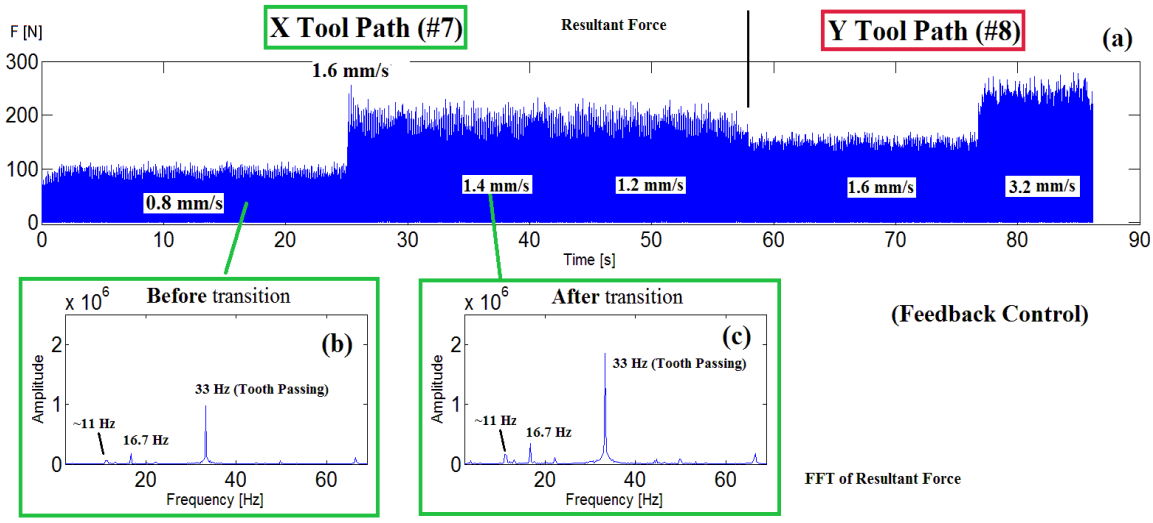

Figure 59. Closed loop robotic milling in the X and Y directions (Tests #7 and #8).

Test#5 and #6 investigate if the proposed algorithm can distinguish between chatter and feed rate-induced transients in the cutting forces. As shown in Table 7, the 1.6 mm/s feed rate used in Test #5 was set to induce chatter for tool motion in the X direction. This feed rate-induced chatter can be observed in the FFT of the resultant force, shown in Figure 58b and Figure 58c. There is a significant increase in the 11 Hz chatter frequency component after the feed rate was doubled in Test #5. This chatter phenomenon is captured by the wavelet signal in Figure 58d, which is suppressed via the closed loop feedback implemented in Test #7, as seen in Figure 59a.

The feed rate-induced transient in the resultant cutting force of Test #6 was designed as a false alarm to examine the robustness of the chatter detection algorithm. As observed in the FFT for Test #6, the sudden increase in feed rate caused a significant increase in the tooth passing frequency component, while the chatter frequency component did not increase dramatically (see Figure 58f). Thus, the wavelet signal did not trigger a false alarm because the tooth passing frequency was outside the 9th DWT decomposition level, as shown in Figure 58g.

Similarly, Tests #9-12 confirm that the algorithm was able to detect and suppress chatter caused by the sudden increase in the axial depth of cut, and was robust to the workpiece geometry-induced transients in the cutting forces.

6.4 Summary

In this chapter, a method for real time chatter detection and suppression was proposed to account for uncertainties in the robotic milling process under more complex cutting conditions. To compute the stability characteristics along a tool path characterized by significant variations in the cutting conditions and arm configuration, the tool path was partitioned into small sections where the stability characteristics could be assumed constant within each section. A methodology to determine the proper section lengths within the tool path was proposed.

Using the CCT-based mode coupling chatter analysis described in Chapter 5, an analysis of the stability characteristics within each section of the tool path was performed. This analysis 1) allows determination of the initial cutting condition, 2) provides a guideline for adjustment of the cutting condition in case chatter accidently occurs due to uncertainty/inaccuracy in the initial cutting parameter calculation, and 3) enables a prediction/understanding of the stability characteristics along the entire tool path, which is helpful for tool path planning.

A real-time wireless PVDF sensor system was implemented into the robotic milling system to measure the cutting force-induced dynamic strain signal. A wavelet transform based online chatter detection algorithm and chatter suppression strategy were presented and experimentally validated. The proposed chatter detection algorithm was shown to efficiently recognize the onset of chatter while the chatter suppression strategy was also verified to be effective in minimizing chatter during robotic milling.

CHAPTER 7. CONCLUSIONS AND RECOMMENDATIONS

This chapter summarizes the main conclusions and the original contributions of this thesis. In addition, it recommends possible areas for future work.

7.1 Conclusions

The main conclusions of this thesis are summarized below.

Effect of Robot Dynamics on Milling Forces in Robotic Milling

A dynamic milling force model incorporating the effect of robot dynamics and the effect of external forces on the robot stiffness was developed and implemented. The force model considers the influence of system compliance on the equilibrium or "steady state" uncut chip thickness using an iterative computation process. The iterative approach showed reductions of up to 50% and 75% in the simulation errors for F_{peak} and F_{PV}, respectively. Thus, the significance of the effect of robot dynamics on the resultant milling force as a function of the robot configuration and cutting conditions was analyzed. This relationship was shown to be capable of identifying the robot arm configurations that are relatively insensitive to the effect of robot dynamics, and consequently the arm configurations for which the static cutting force model can be utilized.

Milling Force Model Based Approach for Enhancement of Machining Accuracy

A method that uses wireless force sensing in combination with a mechanistic static milling force model to improve the dimensional accuracy of the cut feature

produced in robotic milling was proposed. An in-situ thin PVDF film wireless force sensor was used as the high-fidelity sensor to measure the milling forces in real-time. A mechanistic static milling force model using the thin film sensor signal was utilized to estimate the instantaneous cutter engagements for static deflection error feedback compensation. Improvements of over 70% in the cut surface dimensional error were demonstrated in the robotic milling experiments performed on an aluminum workpiece.

CCT-Based Mode Coupling Chatter Avoidance

The CCT-based stiffness term was integrated into the robotic milling chatter model. Since the stiffness of the robot arm is affected by the external cutting force as accounted for in the CCT-based stiffness model, the effect of cutting conditions, and therefore the milling forces, can be simulated to determine the stability of the robotic milling system. In addition, a chatter avoidance method using the CCT-based external force related stiffness term was proposed. Suitable cutting conditions were chosen to adjust the angle between the resultant cutting force and the maximum stiffness vectors and thereby avoid mode coupling chatter in robotic milling. Robotic milling experiments demonstrated significant reductions (>45%) in the average resultant force when the proposed chatter avoidance strategy was implemented.

Chatter Suppression using Closed Loop Control

Using the CCT-based mode coupling chatter model, a method to determine the stability characteristics for longer and more complex tool paths was proposed. The stability characteristics of small sections along the tool path were analyzed to determine the global stability along the tool path. In addition, the method was used to select initial

cutting parameters for closed loop control. To account for modeling uncertainties, a method for real time chatter detection and suppression was proposed. A real time wireless PVDF sensor system was used to measure the cutting force-induced dynamic strain signal. The time domain strain signal corresponding to the mode coupling chatter frequency was isolated within a wavelet decomposition band, which was used for monitoring the onset of chatter. The proposed online chatter detection and suppression approaches were experimentally validated. Once chatter was detected, the cutting conditions were adjusted to suppress chatter using the adjustment guidelines derived from the CCT-based chatter model. In addition, the proposed chatter detection algorithm was shown to be robust to cutting parameter-induced transients in the cutting forces.

7.2 Original Contributions

The contributions of this thesis are as follows:

1. A new hybrid method was proposed that combines wireless force sensing with a mechanistic model of the milling forces to improve the dimensional accuracy obtained in robotic milling.
2. A more comprehensive model for robotic milling chatter was developed by integrating the Conservative Congruence Transformation (CCT) that accounts for the effect of cutting forces on the robot stiffness.
3. Using the improved robotic milling chatter model, a method for chatter avoidance and real time chatter detection was developed and experimentally verified.

7.3 Recommendations for Future Work

All the methods and algorithms developed in this thesis can potentially be applied to improving the performance of robotic milling in shop floor applications. A potential future work of this thesis could be a more comprehensive dynamic milling force model for robotic milling that also accounts for the effect of the vibration in the axial direction. With a better understanding of the dynamic effect of the robotic arm on the machining force under different cutting conditions, an algorithm for compensating dynamic effects may also be a potential topic for future work. In addition, future work can also include the development of a 6 dof model for deflection error compensation in more complex machining scenarios.

To commercialize the methods introduced in this thesis, physical shielding of the sensor electronics is required to protect the sensors and electronics from coolant and chips. Though the theory presented in this thesis can be applied to other serial link robots, current state-of-the-art robots are recommended for industrial milling applications. Robot controllers with faster communication speed are necessary to compensate for the static and dynamic deflection error produced during complex tool paths. In addition, a robot with larger stiffness than the one used in this thesis can be used to widen the range of chatter free cutting conditions.

APPENDIX A

Milling Force Model Details in CHAPTER 5

(1) Mechanistic Average Milling Force Model

The mechanistically derived average milling force components in the X_o (the radial depth of cut), Y_o (axial depth of cut), and Z_o (feed) directions are given by [55]: (Coordinate Δ_o is shown in Figure 27 in Section 5.2)

$$\bar{F}_{x_o} = \left\{\frac{Na}{8\pi}[cK_{tc}(2\emptyset - sin2\emptyset) + cK_{rc}cos2\emptyset - 4K_{te}cos\emptyset - 4K_{re}sin\emptyset]\right\}_{\emptyset_{st}}^{\emptyset_{ex}} \quad \text{(A1)}$$

$$\bar{F}_{y_o} = \left\{\frac{Na}{2\pi}[-cK_{ac}cos\emptyset + K_{ae}\emptyset]\right\}_{\emptyset_{st}}^{\emptyset_{ex}} \quad \text{(A2)}$$

$$\bar{F}_{z_o} = \left\{\frac{Na}{8\pi}[cK_{tc}cos2\emptyset - cK_{rc}(2\emptyset - sin2\emptyset) - 4K_{te}sin\emptyset + 4K_{re}cos\emptyset]\right\}_{\emptyset_{st}}^{\emptyset_{ex}} \quad \text{(A3)}$$

$$|\bar{F}| = \sqrt{\left(\bar{F}_{x_o}\right)^2 + \left(\bar{F}_{y_o}\right)^2 + \left(\bar{F}_{z_o}\right)^2} \quad \text{(A4)}$$

where $\left(\bar{F}_{x_o}, \bar{F}_{y_o}, \bar{F}_{z_o}\right)$ are the average milling force components in the $X_oY_oZ_o$ directions of coordinate Δ_o, a is the axial depth of cut, N is the number of cutter teeth, c is the feed, and $\emptyset_{st}$ and $\emptyset_{ex}$ are the cutter entry and exit angles. (K_{tc},K_{rc}, K_{ac}) are the cutting force coefficients contributed by the shearing action in the tangential, radial, and axial directions, respectively, and (K_{te},K_{re}, K_{ae}) are the edge force coefficients, which can be obtained experimentally as discussed in [55]. In the present work, (K_{rc}, K_{tc}, K_{ac}) are 2.94×10^8, 9.04×10^8, and 2.78×10^8 N/m^2, respectively, while (K_{re}, K_{te}, K_{ae}) are 6.6×10^3, 6.09×10^3, and 1.12×10^3 N/m, respectively.

(2) Calculation of $\boldsymbol{K_{px_o}}$

$K_{px_o} = \frac{\partial|\bar{F}|}{\partial x_o}$ is the sensitivity of $d|\bar{F}|$ due to small deflection dx_o from the nominal position x_m during milling in coordinate Δ_o.

(X_o direction) Radial depth of cut is a variable around x_m: $x_m = R(1 - cos\emptyset_{ex})$

(Y_o direction) Axial depth of cut is assumed constant: $a = const$

The small variation in radial depth of cut dx_o can be represented in $d\emptyset$, as shown in Figure 60 and below:

$$dx_o = (sin\emptyset_{ex}) * ds = (sin\emptyset_{ex})R * d\emptyset \quad \text{(A5)}$$

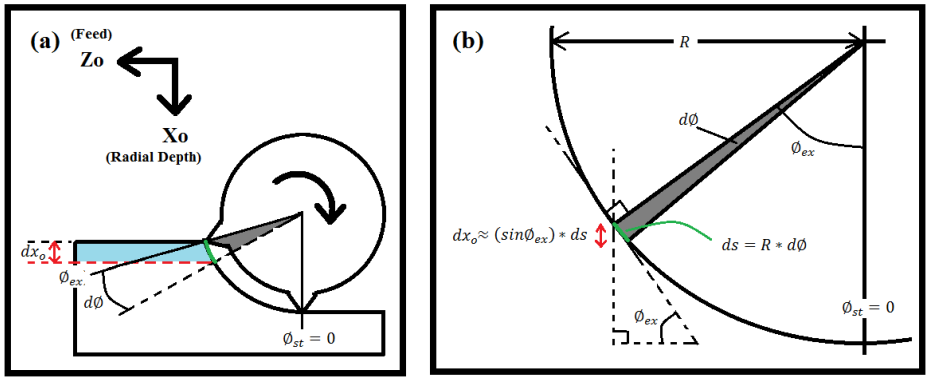

Figure 60. Schematic of the relationship between dx and $d\emptyset$. (R is the radius of the cutter)

The calculation of K_{px_o} is shown as below: (1) substitute $\emptyset_{ex} = \emptyset$ as the variale, (2) replace ∂x_o with $\partial\emptyset$ in the denominator using linear approximation (Equation A5), (3) perform the partial derivative with respect to $\emptyset$, and (4) evaluate $\emptyset = \emptyset_{ex}$.

$$KX_{px_o} = \frac{\partial \bar{F}_{x_o}}{\partial x_o} = \left(\frac{\partial \left\{ \frac{Na}{8\pi} [cK_{tc}(2\emptyset - sin2\emptyset) + cK_{rc}cos2\emptyset - 4K_{te}cos\emptyset - 4K_{re}sin\emptyset]_{\emptyset_{st}}^{\emptyset} \right\}}{(sin\emptyset_{ex})R * \partial\emptyset} \right)_{\emptyset=\emptyset_{ex}}$$

$$= \left(\frac{\partial \left\{ \frac{Na}{8\pi} [cK_{tc}(2\emptyset - sin2\emptyset) + cK_{rc}cos2\emptyset - 4K_{te}cos\emptyset - 4K_{re}sin\emptyset] \right\}}{(sin\emptyset_{ex})R * \partial\emptyset} \right)_{\emptyset=\emptyset_{ex}}$$

$$= \left(\frac{Na}{8R\pi * sin\emptyset_{ex}} \right) \left(\frac{\partial [cK_{tc}(2\emptyset - sin2\emptyset) + cK_{rc}cos2\emptyset - 4K_{te}cos\emptyset - 4K_{re}sin\emptyset]}{\partial\emptyset} \right)_{\emptyset=\emptyset_{ex}}$$

$$= \left(\frac{Na}{8R\pi * sin\emptyset_{ex}} \right) [cK_{tc}(2 - 2cos2\emptyset) - 2cK_{rc}sin2\emptyset + 4K_{te}sin\emptyset - 4K_{re}cos\emptyset]_{\emptyset=\emptyset_{ex}}$$

$$= \left(\frac{Na}{8R\pi * sin\emptyset_{ex}} \right) [cK_{tc}(2 - 2cos2\emptyset_{ex}) - 2cK_{rc}sin2\emptyset_{ex} + 4K_{te}sin\emptyset_{ex} - 4K_{re}cos\emptyset_{ex}] \quad \text{(A6)}$$

Similarly,

$$KY_{px_o} = \frac{\partial \bar{F}_{y_o}}{\partial x_o} = \left(\frac{Na}{2R\pi * sin\emptyset_{ex}} \right) (cK_{ac}sin\emptyset_{ex} + K_{ae}) \quad \text{(A7)}$$

$$KZ_{px_o} = \frac{\partial \bar{F}_{z_o}}{\partial x_o} = \left(\frac{Na}{8R\pi * sin\emptyset_{ex}} \right) [-2cK_{tc}sin2\emptyset_{ex} - cK_{rc}(2 - 2cos2\emptyset_{ex}) - 4K_{te}cos\emptyset_{ex} - 4K_{re}sin\emptyset_{ex}] \quad \text{(A8)}$$

Therefore, $K_{px_o} = \frac{\partial |\bar{F}|}{\partial x_o} = \sqrt{\left(KX_{px_o}\right)^2 + \left(KY_{px_o}\right)^2 + \left(KZ_{px_o}\right)^2}$ (A9)

(3) Calculation of $\boldsymbol{K_{py_o}}$

$K_{py_o} = \frac{\partial |\bar{F}|}{\partial y_o}$ is the sensitivity of $d|\bar{F}|$ due to small deflections dy_o from the nominal position y_m during milling in coordinate Δ_o.

(X_o direction) The radial depth of cut (or $\emptyset_{ex}$) is assumed constant:

$$x_m = R(1 - cos\emptyset_{ex}) \rightarrow \emptyset_{ex} = const$$

(Y_o direction) The axial depth of cut is a variable around y_m: $a = y_o = y_m + dy_o$

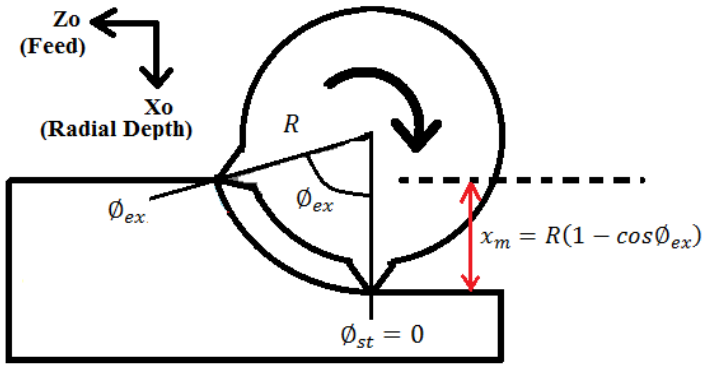

Figure 61. Schematic of the up-milling coordinate system.

The calculation of K_{py_o} is as follows: (1) substitute $a = y_o$ as the variable in the average force equation, (2) differentiate with respect to y_o, and (3) evaluate $y_o = y_m$.

$$\bar{F}_{x_o} = \left\{\frac{Na}{8\pi}[cK_{tc}(2\emptyset - sin2\emptyset) + cK_{rc}cos2\emptyset - 4K_{te}cos\emptyset - 4K_{re}sin\emptyset]\right\}_{\emptyset_{st}}^{\emptyset_{ex}}$$
$$= \left\{\frac{Ny_o}{8\pi}[cK_{tc}(2\emptyset - sin2\emptyset) + cK_{rc}cos2\emptyset - 4K_{te}cos\emptyset - 4K_{re}sin\emptyset]\right\}_{\emptyset_{st}}^{\emptyset_{ex}} \quad \text{(A10)}$$

$$KX_{py_o} = \frac{\partial \bar{F}_{x_o}}{\partial y_o} = \left\{\frac{N}{8\pi}[cK_{tc}(2\emptyset - sin2\emptyset) + cK_{rc}cos2\emptyset - 4K_{te}cos\emptyset - 4K_{re}sin\emptyset]\right\}_{\emptyset_{st}}^{\emptyset_{ex}} \quad \text{(A11)}$$

Similarly,

$$KY_{py_o} = \frac{\partial \bar{F}_{y_o}}{\partial y_o} = \left\{\frac{N}{2\pi}[-cK_{ac}cos\emptyset + K_{ae}\emptyset]\right\}_{\emptyset_{st}}^{\emptyset_{ex}} \quad \text{(A12)}$$

$$KZ_{py_o} = \frac{\partial \bar{F}_{z_o}}{\partial y_o} = \left\{\frac{N}{8\pi}[cK_{tc}cos2\emptyset - cK_{rc}(2\emptyset - sin2\emptyset) - 4K_{te}sin\emptyset + 4K_{re}cos\emptyset]\right\}_{\emptyset_{st}}^{\emptyset_{ex}} \quad \text{(A13)}$$

Please note that $|\bar{F}|$ is decreased with positive deflection y_o , or reduced axial depth of cut. Therefore,

$$K_{py_o} = \frac{\partial |\bar{F}|}{\partial y_o} = -\sqrt{\left(KX_{py_o}\right)^2 + \left(KY_{py_o}\right)^2 + \left(KZ_{py_o}\right)^2} \quad \text{(A14)}$$

(4) Calculation of $\boldsymbol{K_{px}}$ and $\boldsymbol{K_{py}}$

According to Section 5.2, a new coordinate system ($\Delta: XYZ$) is defined by rotating the original coordinate system ($\Delta_o: X_oY_oZ_o$) by angle α about the negative Y_o axis, as shown in Figure 27. Therefore, the projection of the deflection dx and dy from Δ to Δ_o is:

$$dx_o = dx * cos\alpha \tag{A15}$$

$$dy_o = dy \tag{A16}$$

Therefore, the corresponding K_{px} and K_{py} in the new coordinate system ($\Delta: XYZ$) are:

$$K_{px} = \left(\frac{\partial|\bar{F}|}{\partial x}\right) = \left(\frac{\partial|\bar{F}|}{\partial x_o}\right)\left(\frac{dx_o}{dx}\right) = K_{px_o} * cos\alpha \tag{A17}$$

$$K_{py} = \left(\frac{\partial|\bar{F}|}{\partial y}\right) = \left(\frac{\partial|\bar{F}|}{\partial y_o}\right)\left(\frac{dy_o}{dy}\right) = K_{py_o} \tag{A18}$$

REFERENCES

1. Hu, Y.N. and Y.H. Chen, *Implementation of a robot system for sculptured surface cutting. Part 1. Rough machining.* The International Journal of Advanced Manufacturing Technology, 1999. **15**(9): p. 624-629.

2. Matsuoka, S.-i., et al., *High-speed end milling of an articulated robot and its characteristics.* Journal of Materials Processing Technology, 1999. **95**(1–3): p. 83-89.

3. Abele, E., M. Weigold, and S. Rothenbücher, *Modeling and Identification of an Industrial Robot for Machining Applications.* CIRP Annals - Manufacturing Technology, 2007. **56**(1): p. 387-390.

4. Klimchik, A., et al., *Compliance Error Compensation in Robotic-Based Milling.* Informatics in Control, Automation and Robotics, 2014. **283**: p. 197-216.

5. Sutherland, J. and R.E. Devor, *An improved method for cutting force and surface error prediction in flexible end milling systems.* Journal of engineering for industry, 1986. **108**(4): p. 269-279.

6. Sutherland, J.W. and R. DeVor, *A dynamic model of the cutting force system in the end milling process.* Diss. Abstr. Int., 1988. **49**(1): p. 293.

7. Montgomery, D. and Y. Altintas, *Mechanism of cutting force and surface generation in dynamic milling.* Journal of Engineering for Industry, 1991. **113**(2): p. 160-168.

8. Zhang, H., et al., *Machining with flexible manipulator: toward improving robotic machining performance*, in *IEEE/ASME International Conference on Advanced Intelligent Mechatronics*. 2005. p. 1127-1132.

9. Wang, J., H. Zhang, and Z. Pan, *Machining with flexible manipulators: Critical issues and solutions.* 2006: p. 515-536.

10. Pan, Z., et al., *Chatter analysis of robotic machining process.* Journal of materials processing technology, 2006. **173**(3): p. 301-309.

11. Pan, Z. and H. Zhang, *Analysis and suppression of chatter in robotic machining process*, in *International Conference on Control, Automation and Systems*. 2007. p. 595-600.

12. Abele, E., M. Weigold, and M. Kulok, *Increasing the accuracy of a milling industrial robot.* Production Engineering, 2006. **13**(2): p. 221-224.

13. Abele, E., M. Weigold, and S. Rothenbücher, *Modeling and identification of an industrial robot for machining applications.* CIRP Annals-Manufacturing Technology, 2007. **56**(1): p. 387-390.

14. Cortsen, J. and H.G. Petersen, *Advanced off-line simulation framework with deformation compensation for high speed machining with robot manipulators*, in *IEEE/ASME International Conference on Advanced Intelligent Mechatronics (AIM)*. 2012. p. 934-939.

15. Mejri, S., et al., *Dynamic characterization of machining robot and stability analysis.* The International Journal of Advanced Manufacturing Technology, 2015. **82**(1-4): p. 351-359.

16. Tunc, L. and J. Shaw, *Investigation of the effects of Stewart platform-type industrial robot on stability of robotic milling.* The International Journal of Advanced Manufacturing Technology, 2016. p. 1-11.

17. Bondarenko, D., et al., *Elasto-dynamic model of robotic milling process considering interaction between tool and workpiece*, in *ASME Biennial Conference on Engineering Systems Design and Analysis*. 2012. p. 217-226.

18. Alici, G. and B. Shirinzadeh, *Enhanced stiffness modeling, identification and characterization for robot manipulators.* IEEE Transactions on Robotics, 2005. **21**(4): p. 554-564.

19. Chen, S.F. and I. Kao, *Conservative congruence transformation for joint and cartesian stiffness matrices of robotic hands and fingers.* The International Journal of Robotics Research, 2000. **19**(9): p. 835-847.

20. Kao, I. and C. Ngo, *Properties of the grasp stiffness matrix and conservative control strategies.* The International Journal of Robotics Research, 1999. **18**(2): p. 159-167.

21. Li, Y., S.-F. Chen, and I. Kao, *Stiffness control and transformation for robotic systems with coordinate and non-coordinate bases*, in *IEEE International Conference on Robotics and Automation International Conference*. 2002. p. 550-555.

22. Freeman, R.A., *Synthesis of actively adjustable springs by antagonistic redundant actuation.* Journal of Dynamic Systems, Measurement, and Control, 1992. **114**: p. 455.

23. Choi, H., W.K. Chung, and Y. Youm, *Stiffness analysis and control of redundant manipulators*, in *IEEE Robotics and Automation International Conference*. 1994. p. 689-695.

24. Li, Y. and I. Kao, *A review of modeling of soft-contact fingers and stiffness control for dextrous manipulation in robotics*, in *IEEE Robotics and Automation International Conference*. 2001. p. 3055-3060.

25. Dumas, C., et al., *Workpiece placement optimization of six-revolute industrial serial robots for machining operations*, in *ASME Biennial Conference on Engineering Systems Design and Analysis*. 2012. p. 419-428.

26. Caro, S., et al. *Workpiece placement optimization for machining operations with a KUKA KR270-2 robot*. in *IEEE International Conference on Robotics and Automation (ICRA)*. 2013. p. 2921-2926.

27. Chen, Y. and F. Dong, *Robot machining: recent development and future research issues.* The International Journal of Advanced Manufacturing Technology, 2013. **66**(9-12): p. 1489-1497.

28. Slavkovic, N.R., D.S. Milutinovic, and M.M. Glavonjic, *A method for off-line compensation of cutting force-induced errors in robotic machining by tool path modification.* The International Journal of Advanced Manufacturing Technology, 2014. **70**(9-12): p. 2083-2096.

29. Kaldestad, K.B., I. Tyapin, and G. Hovland. *Robotic face milling path correction and vibration reduction*. in *IEEE International Conference on Advanced Intelligent Mechatronics (AIM)*. 2015. p. 543-548.

30. Seltzer, M., et al., *High speed cutting with industrial robots: towards model based compensation of deviations*, in *Robotik Conference*. 2008: Munich, Germany. p. 143-146.

31. Schneider, U., et al., *Improving robotic machining accuracy through experimental error investigation and modular compensation.* The International Journal of Advanced Manufacturing Technology, 2014. p. 1-13.

32. Klimchik, A., et al., *Experimental study of robotic-based machining.* IFAC-PapersOnLine, 2016. **49**(12): p. 174-179.

33. Kunieda, M., T. Nakagawa, and T. Higuchi, *Robot-polishing of curved surface with magnetically pressed polishing tool.* Journal of the Japan Society for Precision Engineering, 1988. **54**(1): p. 125-131.

34. Yamane, Y., et al., *Application of multi-joint type industrial robot to scraping of surface plate.* Journal of the Japan Society for Precision Engineering, 1989. **55**(10): p. 1787-1792.

35. Takeuchi, Y., N. Asakawa, and D. Ge, *Automation of polishing work by an industrial robot: system of polishing robot.* JSME International Journal. Ser. C, Dynamics, Control, Robotics, Design and Manufacturing, 1993. **36**(4): p. 556-561.

36. Jinno, M., et al., *Development of a force controlled robot for grinding, chamfering and polishing*, in *IEEE Robotics and Automation International Conference*. 1995. p. 1455-1460.

37. Tao, Z., M. Nakamura, and N. Kyura, *High-precision contour control of industrial robot arm by neural network compensation with learning uncertainties*, in *IEEE Industrial Electronics International Symposium*. 2001. p. 1650-1655.

38. Abele, E., S. Rothenbücher, and M. Weigold, *Cartesian compliance model for industrial robots using virtual joints.* Production Engineering, 2008. **2**(3): p. 339-343.

39. Gasparetto, A., *A system theory approach to mode coupling chatter in machining.* Journal of Dynamic systems, Measurement, and Control, 1998. **120**(4): p. 545-547.

40. Gasparetto, A., *Eigenvalue analysis of mode-coupling chatter for machine-tool stabilization.* Journal of Vibration and Control, 2001. **7**(2): p. 181-197.

41. Tobias, S.A., *Machine-tool vibration*. 1965.

42. Tse, W. and Y. Chen. *A robotic system for rapid prototyping*. in *IEEE International Conference on Robotics and Automation.* 1997. p. 1815-1820.

43. Lee, M.K. *Design of a high stiffness machining robot arm using double parallel mechanisms*. in *IEEE International Conference on Robotics and Automation*. 1995. p. 234-240.

44. Stewart, D., *A platform with six degrees of freedom.* Proceedings of the institution of mechanical engineers, 1965. **180**(1): p. 371-386.

45. Surdilović, D. and M. Vukobratović, *Deflection compensation for large flexible manipulators.* Mechanism and Machine Theory, 1996. **31**(3): p. 317-329.

46. Hwang, J.C., et al., *Error compensation of a large scale LCD Glass transfer robot*, in *International Federation of Automatic Control*. 2008. p. 6-11.

47. Abderrahim, M., et al., *Accuracy and calibration issues of industrial manipulators.* Industrial Robotics: Programming, Simulation and Application, 2007. p. 131-146.

48. Wang, J., H. Zhang, and T. Fuhlbrigge, *Improving machining accuracy with robot deformation compensation*, in *IEEE Intelligent Robots and Systems International Conference*. 2009. p. 3826-3831.

49. Oiwa, T., *Error compensation system for joints, links and machine frame of parallel kinematics machines.* The International Journal of Robotics Research, 2005. **24**(12): p. 1087-1102.

50. Sörnmo, O., et al., *Increasing time-efficiency and accuracy of robotic machining processes using model-based adaptive force control.* IFAC Proceedings Volumes, 2012. **45**(22): p. 543-548.

51. Schneider, U., et al., *Integrated approach to robotic machining with macro/micro-actuation.* Robotics and Computer-Integrated Manufacturing, 2014. **30**(6): p. 636-647.

52. Salisbury, J.K., *Active stiffness control of a manipulator in cartesian coordinates*, in *IEEE Decision and Control including the Symposium on Adaptive Processes Conference*. 1980. p. 95-100.

53. Tobias, S. and W. Fishwick, *The chatter of lathe tools under orthogonal cutting conditions.* Trans. ASME, 1958. **80**(2): p. 1079-1088.

54. Tlusty, J. and M. Polacek, *The stability of machine tools against aelf-excited vibrations in machining.* International Research in Production Engineering, 1963. **1**(1): p. 465-474.

55. Altintas, Y., *Manufacturing automation: metal cutting mechanics, machine tool vibrations, and CNC design*. 2012.

56. Dumas, C., et al. *A methodology for joint stiffness identification of serial robots*. in *IEEE/RSJ International Conference on Intelligent Robots and Systems (IROS)* 2010. p. 464-469.

57. Dumas, C., et al., *Joint stiffness identification of six-revolute industrial serial robots.* Robotics and Computer-Integrated Manufacturing, 2011. **27**(4): p. 881-888.

58. Mason, M.T. and J.K. Salisbury Jr, *Robot hands and the mechanics of manipulation*. 1985.

59. Cen, L., et al., *A Wireless Force Sensing and Model Based Approach for Enhancement of Machining Accuracy in Robotic Milling.* IEEE/ASME Transactions on Mechatronics, 2016. **21**(5): p. 2227 - 2235.

60. Ma, L., et al., *Thin-film PVDF sensor-based monitoring of cutting forces in peripheral end milling.* Journal of Dynamic Systems, Measurement, and Control, 2012. **134**(5): p. 051014.

61. Gradišek, J., M. Kalveram, and K. Weinert, *Mechanistic identification of specific force coefficients for a general end mill.* International Journal of Machine Tools and Manufacture, 2004. **44**(4): p. 401-414.

62. Engin, S. and Y. Altintas, *Mechanics and dynamics of general milling cutters.: Part I: Helical end mills.* International Journal of Machine Tools and Manufacture, 2001. **41**(15): p. 2195-2212.

63. Engin, S. and Y. Altintas, *Mechanics and dynamics of general milling cutters.: Part ii: Inserted cutters.* International Journal of Machine Tools and Manufacture, 2001. **41**(15): p. 2213-2231.

64. Yang, M. and H. Park, *The prediction of cutting force in ball-end milling.* International Journal of Machine Tools and Manufacture, 1991. **31**(1): p. 45-54.

65. Lazoglu, I., *Sculpture surface machining: a generalized model of ball-end milling force system.* International Journal of Machine Tools and Manufacture, 2003. **43**(5): p. 453-462.

66. Nyman, P. and M. Edberg, *Implementing multi-touch screen for real-time control of a robotic cell, at Universidad Politécnica de Valencia*, in *Department of Product and Production Development*. 2010. Master Thesis.

67. Ma, L., S.N. Melkote, and J.B. Castle, *A Model-Based Computationally Efficient Method for On-Line Detection of Chatter in Milling.* Journal of Manufacturing Science and Engineering, 2013. **135**(3): p. 031007.

68. Ma, L., *PVDF sensor based wireless monitoring of milling process, at Georgia Institute of Technology*, in *Department of Mechanical Engineering*. 2013. PhD Thesis.